MAGNETOSTRUCTURAL CORRELATIONS IN POLYNUCLEAR COMPLEXES OF PHTHALAZINE BASED TETRA- AND HEXADENTATE LIGANDS

CHRISTOPHER LORENZO SHEPPARD

INFORMATION TO USERS

This manuscript has been reproduced from the microfilm master. UMI films the text directly from the original or copy submitted. Thus, some thesis and dissertation copies are in typewriter face, while others may be from any type of computer printer.

The quality of this reproduction is dependent upon the quality of the copy submitted. Broken or indistinct print, colored or poor quality illustrations and photographs, print bleedthrough, substandard margins, and improper alignment can adversely affect reproduction.

In the unlikely event that the author did not send UMI a complete manuscript and there are missing pages, these will be noted. Also, if unauthorized copyright material had to be removed, a note will indicate the deletion.

Oversize materials (e.g., maps, drawings, charts) are reproduced by sectioning the original, beginning at the upper left-hand corner and continuing from left to right in equal sections with small overlaps. Each original is also photographed in one exposure and is included in reduced form at the back of the book.

Photographs included in the original manuscript have been reproduced xerographically in this copy. Higher quality 6" x 9" black and white photographic prints are available for any photographs or illustrations appearing in this copy for an additional charge. Contact UMI directly to order.

UMI

A Bell & Howell Information Company
300 North Zeeb Road, Ann Arbor MI 48106-1346 USA
313/761-4700 800/521-0600

Magnetostructural Correlations in Polynuclear Complexes of Phthalazine Based Tetra- and Hexadentate Ligands

by

Christopher Lorenzo Sheppard, B.Sc.(Honours)

A thesis submitted to the

School of Graduate Studies

in partial fulfilment of the

requirements for the degree

Master of Science

Department of Chemistry

Memorial University of Newfoundland

St. John's Newfoundland Canada

Abstract

This thesis describes the synthesis, spectroscopic and crystallographic characterisation, and magnetism of a series of polynuclear Cu(II) complexes of the ligand 1,4-bis(3'-methyl-2'-pyridyl)aminophthalazine (PAP3Me), and a series of Ni(II) and Mn(II) complexes of the ligand 1,4-bis((6-methylpyridine-2-carboxaldiimino)amino)phthalazine (PHP6Me), with particular interest in μ_2-1,1 azide bridged systems. In addition, a series of Extended Hückel molecular orbital calculations investigating the variation of magnetic behaviour with changes in the geometry of the binuclear centre in the phthalazine / μ_2-1,1 azide bridged Cu(II) binuclear system was also undertaken.

Part A is an introduction, consisting of three chapters. Chapter 1 provides an introduction to the study of polynuclear metal complexes. The role of these complexes as a bridge between the physics of molecular magnetism and the biochemistry of metalloenzymes is emphasised, and the theory of magnetism introduced. Chapter 2 develops the theory of molecular magnetism of binuclear metal complexes, including quantitative expressions for magnetic exchange, factors influencing the magnitude and sign of exchange interactions, and computational models (Extended Hückel) of these interactions. Chapter 3 is an overview of the magnetic properties of binuclear and polynuclear complexes linked via azide or thiocyanate bridges.

Part B consists of experimental results, and contains two chapters. Chapter 4 describes the synthesis of complexes based on a Cu_2PAP3Me core, in

which the binuclear Cu(II) centres are bridged by phthalazine and azide or phthalazine and some other exogenous bridge. The X-ray diffraction structures of four Cu(II) complexes, along with infrared, UV / Vis and variable temperature magnetism studies of these four, and five other complexes, are presented. In particular, it is found that the variable temperature magnetic data of the μ_2-1,1 azide bridged complexes **cannot** be fitted to the Bleaney-Bowers equation, whereas the data for the non-azide complexes can. Several other attempts to understand the anomalous magnetism of the azide systems suggests that using a variable temperature -2J best models the observed behaviour. A variable temperature X-ray diffraction study was undertaken in an attempt to rationalise this behaviour in terms of changing bridge geometry, but the results indicate that this is not the case. Extended Hückel molecular orbital calculations were also carried out and showed that magnetic coupling in phthalazine / μ_2-1,1 azide bridged Cu(II) systems is a function of not only the μ_2-1,1 azide bridge angle, but of other geometric distortions of the azide bridge. Chapter 5 presents the synthesis, preliminary X-ray diffraction studies, spectroscopic studies, and magnetism of Ni(II) and Mn(II) complexes of the ligand PHP6Me, plus either azide or thiocyanate. Due to a lack of firm structural data, the results are inconclusive, and attempts to establish unequivocally an antiferromagnetic realm for μ_2-1,1 azide bridged Ni(II) and Mn(II) complexes proved unsuccessful.

Acknowledgements

First of all, I would like to express my thanks to my supervisor Dr. Laurence K. Thompson for his advice and encouragement, patience and support during the course of the research presented herein. As well, I would like to acknowledge the advice and support of the other members of my supervisory committee, Dr. C. Robert Lucas and Dr. Peter G. Pickup.

Special acknowledgement is extended to Mr. David O. Miller and Dr. John N. Bridson of the Department of Chemistry, Memorial University of Newfoundland, and Dr. Andres E. Goeta and Prof. Judith A. K. Howard of the Department of Chemistry, University of Durham, for the X-ray structure determinations. Additional thanks are extended to Dr. Goeta and Prof. Howard for making my time spent at the University of Durham both enjoyable and informative.

I would like to thank Dr. Thompson, the Department of Chemistry, and School of Graduate Studies of Memorial University of Newfoundland for financial support during the course of this study. The North Atlantic Treaty Organization is also acknowledged for financial assistance, in the form of a joint research grant between Dr. Thompson and Prof. Howard, allowing crystallographic studies at the University of Durham.

I would like to acknowledge all of my colleagues in the Thompon research group. Especial thanks are extended to Dr. Santokh S. Tandon for his help in obtaining X-ray quality crystals for several of the complexes reported herein.

Without his assistance, this study would be much less complete. In addition, special thanks go to Mr. Mike E. Manuel for guiding me through the lab during my first few months, Dr. Makoto Handa for laying the groundwork for understanding some of the magnetism presented herein, and Mr. Murray K. Park for helping keep my head above water and my feet on the ground.

Thanks are also extended to all the students, staff and faculty of the Department of Chemistry, to numerous to mention by name, who have made my years at Memorial an experience to remember.

Finally, I would like to thank my parents, Lloyd and Una, and my sister, Lorraine. Even if they weren't always sure exactly what their son or brother was doing with his life, they were always unfailing in their support. This thesis is dedicated to them.

Table of Contents

List of Tables

Table

List of Figures

Figure

List of Abbreviations and Symbols

APHP	1,4-bis((pyrid-2-ylacetaldiimino)amino)phthalazine
D	axial zero field splitting parameter
deoxyHc	deoxyhemocyanin
EHMO	Extended Hückel molecular orbital
emu	electromagnetic unit
EXAFS	extended X-ray absorption fine structure
g	Landé splitting factor
H	magnetic field
Hc	hemocyanin
Hdd	orbital energy for a "d" orbital
Hpp	orbital energy for a "p" orbital
Hss	orbital energy for a "s" orbital
$\mathbf{H}$	Hamiltonian
J	exchange integral
J'	interdimer exchange integral
$J_{ai,ai}$, $J_{ai,bi}$	two electron Coulomb integral
k	Boltzman constant
K_{ij}	two electron exchange integral
m	the number of distinct pairs of molecular orbitals
M	molar magnetisation

MO	molecular orbital
N	Avagadro's number
Nα	temperature independent paramagnetism (TIP)
oxyHc	oxyhemocyanin
PAP3Me	1,4-bis(3'-methyl-2'-pyridyl)aminophthalazine
PAPR	1,4-bis(R-methyl-2'-pyridyl)aminophthalazine (R = 3 - 6)
PHP6Me	1,4-bis((6-methylpyridine-2-carboxaldiimino)amino)phthalazine
R	residual factor
s	local spin quantum number
S	dimer spin quantum number
T_c	Curie temperature
T_N	Néel temperature
Z'	dimer lattice coordination number
α	bridge angle
α_o	angle of accidental orthogonality
β	electronic Bohr magneton
χ	magnetic susceptibility
χ_g	gram magnetic susceptibility
χ_M	molar magnetic susceptibility
Δ	energy difference between symmetric and antisymmetric MO's
ε	molar extinction coefficient

ε_i	energy of molecular orbital i
Φ	molecular orbital
μ_{eff}	effective magnetic moment
μ_n	microscopic magnetisation
θ	Curie-Weiss or Weiss-like correction
ρ	fraction of paramagnetic impurity
Ψ	Heitler-London (two-electron) wavefunction
ζ	atomic orbital exponent

Part A. Introduction

Chapter 1. General Introduction

1.1 Preamble

The study of the interactions between metal centres in polynuclear complexes has been, and continues to be, of great interest. Perhaps the most important reason for this is that the phenomenon of interaction between metal centres occupies a place where several scientific disciplines overlap. In particular, it is a bridge between the two extremes of the physics of molecular magnetism and the role of polynuclear centres in biological processes. The following sections will illustrate this concept with regard to the transition metals of interest in this study, with a discussion of some biologically relevant binuclear metalloproteins, and a brief examination of the nature and theory of magnetic behaviour.

1.2 Binuclear Complexes as Models for Biological Systems

1.2.1 Type III Copper Enzymes: Hemocyanin and Tyrosinase

Hemocyanins are a class of copper based dioxygen carriers found in a wide range of molluscs and arthropods. The active site of hemocyanin (Hc) has long attracted the attention of chemists due to its rather unique spectral and physical properties.[1] It is a Type III copper centre; that is, it is ESR silent in the Cu(II) oxygenated form, and also shows very strong antiferromagnetic coupling

($-2J \geq 550\ cm^{-1}$). In addition, rather than the weak d-d transition bands usually found in the electronic spectra of Cu(II) compounds, oxyHc shows two strong bands at 580nm (ε = 1000 $M^{-1}cm^{-1}$) and 345nm (ε = 20000 $M^{-1}cm^{-1}$). EXAFS studies have shown a Cu-Cu separation of ~3.6 Å, and the resonance Raman spectrum shows that the dioxygen is symmetrically coordinated as the peroxide.

The exact structure of the copper active site remained a mystery for some time, but the strong antiferromagnetic coupling was indicative of superexchange via an exogenous bridge. Based on this fact and the experimental data, it was proposed that the two Cu(II) centres were bridged by a μ-1,2-peroxide in either a trans or cis configuration (Fig.1.1). However, both a trans-1,2 model complex prepared by Karlin et al.[2] and computational models of the cis-1,2 configuration studied by Solomon et al.[3] proved to be poor spectroscopic models for oxyHc.

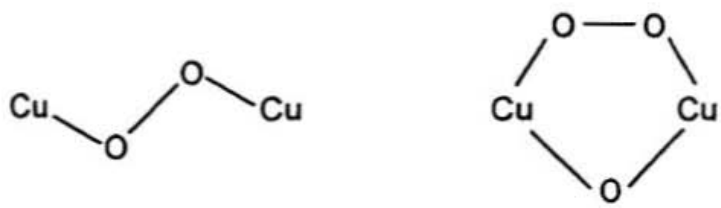

trans μ-1,2 cis μ-1,2

Fig. 1.1 Proposed Structural Models for the Hemocyanin Active Site.

More recently, however, Kitajima et al.[4] reported the structure of a μ-η^2:η^2 peroxide bridged Cu(II) complex which exhibited spectroscopic and magnetic properties nearly identical with those of oxyHc (Fig.1.2(a)).

Indisputable proof for which model best describes the binuclear centre in hemocyanin had, however, to come from a crystal structure of the protein itself. Two reports of the structure of deoxyHc from *P. interruptus*[5] and *L. polyphemus*[6] show essentially the same binuclear centre: each Cu(I) centre is coordinated to three histidine residues in approximately trigonal geometry, and no bridging ligand is observed. It was a structure of the oxygenated *L. polyphemus*[7,8] hemocyanin which finally showed that dioxygen is indeed bound as the μ-η^2:η^2 peroxide (Fig.1.2(b)). The coordination sphere around each Cu(II) is completed by two strongly bound histidines (2.0-2.1Å) and one weakly bound axial histidine (2.4-2.5 Å) to give approximately square pyramidal geometry.

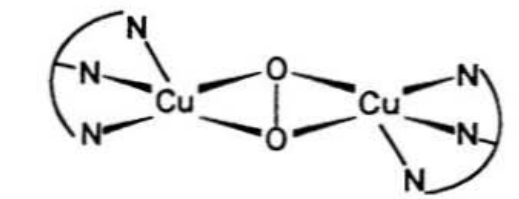

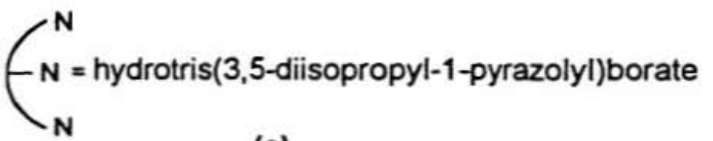

(a)

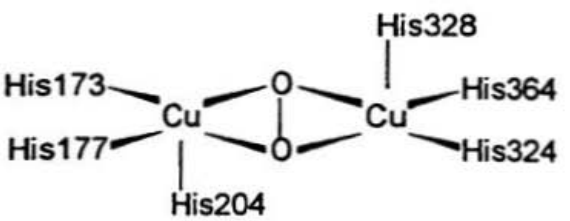

(b)

Fig. 1.2 (a) Kitajima's μ–η^2:η^2 Model Complex (b) Structure of the Hemocyanin Active Site in *L. Polyphemus*.

Tyrosinase is another Type III copper enzyme which catalyses the ortho-hydroxylation of phenols to catechols in a variety of plants, bacteria and animals. The structure of the active site in tyrosinase is not known, but it is spectroscopically very similar to that of hemocyanin.[9] It is therefore generally believed that the structure of tyrosinase in the oxygenated form is similar to that of oxyHc.

1.2.2 Binuclear Enzymes of Other Transition Metals: Urease and Arginase

While hemocyanin has perhaps been the most extensively studied, many other first row transition metals also form binuclear metalloenzymes. These are found in many roles, from oxygen transport enzymes to hydrolases to catalases. An extensive review is beyond the scope of this discussion, but a brief examination of two illustrative systems is presented.

Urease is an enzyme found in certain plants, fungi and bacteria which catalyses the hydrolysis of urea to ammonium carbamate. It is found to contain two Ni(II) centres per protein subunit which prove to be ESR undetectable, suggesting an antiferromagnetically coupled system. Variable temperature magnetism studies do indeed show the binuclear centre to be weakly antiferromagnetically coupled ($-2J = 13\ cm^{-1}$), and it is also found that up to 20% of the Ni(II) centres show no exchange interaction, a phenomenon which is pH dependent.[10] The visible spectrum of jackbean urease shows ligand field bands

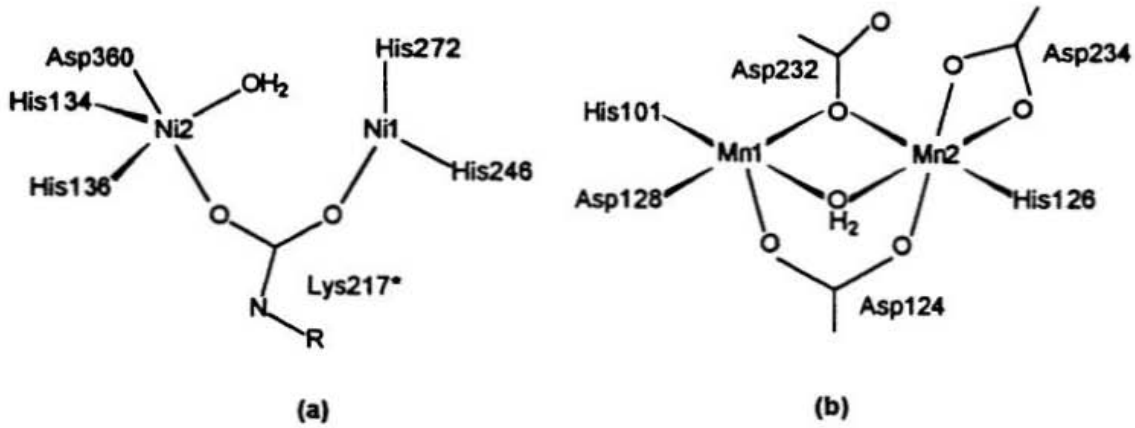

Fig. 1.3 Binuclear Metalloenzymes of First Row Transition Metals. (a) *L. aerogenes* Urease (b) Rat Liver Arginase.

similar to those of 5 or 6 coordinate Ni(II),[10] while the EXAFS spectrum suggests that these are N or O donors, with no S ligands.[11]

The crystal structure at 2.2Å resolution of *K. aerogenes* urease[12] (Fig.1.3(a)) shows two distinct Ni(II) centres, separated by about 3.5Å. Ni1 is coordinated to three ligands and a fourth site is partially occupied by H_2O, so the geometry is best described as pseudotetrahedral. Ni2 is coordinated by five ligands in a distorted trigonal bipyrimidal or square pyramidal geometry. The observed coupling appears to occur through the carbamate bridge of the modified lysine residue

In contrast to nickel, for which urease is the only known binuclear metalloenzyme, binuclear and higher nuclearity manganese clusters are prevalent in biological systems, mainly as redox enzymes[13] and hydrolases.[14] One notable characteristic of manganese in non-redox biological systems, however, is the low metal ion specificity. That is to say, Mn(II) can be easily

interchanged with other divalent metals (especially Mg(II) and Zn(II)) in many systems. As a result, even in cases in which a crystal structure is known, it is often difficult to tell which metal is found in the native metalloenzyme. One of the few shown conclusively to contain manganese in the native enzyme is arginase. It is involved in the terminal step of the urea cycle, in which it catalyses the hydrolyses of the guanidine moiety of L-arginine to give urea and L-ornithine. Rat liver arginase is found as a trimer, with a total of six Mn(II) ions. The low temperature ESR spectrum is quite complex, but shows a ^{55}Mn hyperfine splitting of ~45G,[15] which is about half that expected for isolated Mn(II) and is characteristic for coupled Mn(II) systems. In addition, the temperature dependant ESR spectrum of the borate inhibited enzyme shows an antiferromagnetically coupled system with $-2J = 4\ cm^{-1}$.[16] Little else was known about the manganese active site, however, until the recent publication of a crystal structure of rat liver arginase at 2.1Å resolution[17] (Fig.1.3(B)). It shows two different Mn(II) centres. Mn1 is of square pyramidal geometry, while Mn2 is surrounded by a distorted octahedral array of ligands, and the Mn-Mn separation is 3.3 Å. There are three bridges (2 aspartic acid residues and a H_2O) which are symmetrically arranged between the two metal centres. With three bridges, there are ample exchange pathways for the observed magnetic coupling.

1.3 Principles of Magnetochemistry[18,19]

It is a generally known fact that all substances are influenced by the presence of an external magnetic field. The behaviour of a given substance in a magnetic field is usually expressed in terms of its gram or molar susceptibility, χ_g or χ_M respectively, and can take one of two general forms. When χ is negative, the substance is said to be diamagnetic and is repelled by the magnetic field. This is a property of spin paired electrons, such that all substances have a diamagnetic component. When χ is positive, the substance is attracted into the field, and it is said to be paramagnetic. This is a property of unpaired electrons, and is usually associated with metal ions and organic free radicals.

Even though diamagnetism is ubiquitous, it is a relatively weak and uninteresting force in comparison to paramagnetism. While in both cases χ is independent of field strength, only paramagnets show a dependence on temperature. This relationship was first quantified around the turn of the century by Curie who found that a number of paramagnetic substances showed an inverse relationship between χ and T

$$\chi = C / T \qquad (1.1)$$

where C is the Curie constant. This relationship was later modified by Onnes and Perrier, who found that many paramagnetic substances better fitted the relationship

$$\chi = C / (T + \theta) \qquad (1.2)$$

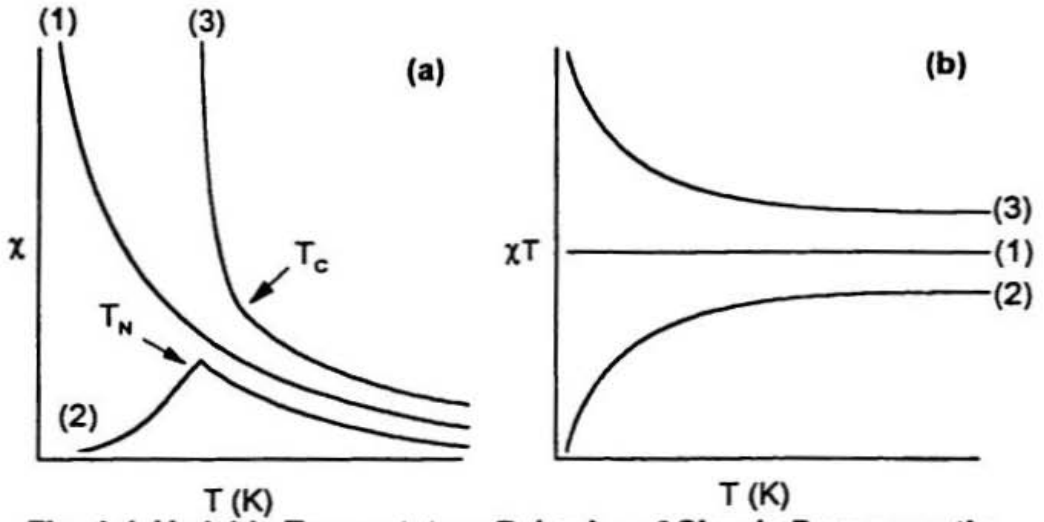

Fig. 1.4 Variable Tempertature Behavior of Simple Paramagnetic (1), Antiferromagnetic (2), and Ferromagnetic (3) Materials (a) χ vs T (b) χT vs T.

where θ is the Curie-Weiss constant, generally taken to account for minor interactions between individual paramagnetic centres.

In addition to simple paramagnetic behaviour, many systems exhibit magnetic coupling between paramagnetic centres. These magnetically concentrated systems can either exhibit ferromagnetism or antiferromagnetism. The variable temperature behaviour of the various types of paramagnetism is shown schematically in Fig.1.4. Ferromagnetic substances demonstrate normal paramagnetic behaviour down to the Curie temperature (T_C). Below T_C, parallel coupling of spins occurs, so that χ is greater than for a simple paramagnet. Conversely, antiferromagnetic substances behave as normal paramagnets down to the Néel temperature (T_N), below which antiparallel coupling of spins occurs and χ is less than expected for a simple paramagnet. Although the transition from simple paramagnetic behaviour to magnetically concentrated behaviour is

sharp in Fig.1.4(a), in practice this is not always the case and the transition may occur over a temperature range. For this reason, magnetic data are often plotted as χ*T vs T as shown in Fig.1.4(b), which enables a definitive distinction between the various types of magnetic behaviour.

Chapter 2. Magnetism of Binuclear Metal Complexes

2.1 The Van Vleck Equation[18,20]

Although the magnetic behaviour of chemical compounds can assume a number of different forms, it is possible to understand and unify magnetic behaviour on the basis of a single relationship. This was first described by Van Vleck[21] in 1932, who derived an equation which when solved for the appropriate Hamiltonian and eigenvector basis set, allows accurate prediction of the susceptibility of a given chemical compound.

The interaction of a substance with a magnetic field is generally described by its magnetisation. In classical terms, this can be represented as

$$M = -\frac{\partial E}{\partial H} \qquad (2.1)$$

where E is the energy and H is the magnetic field. In quantum mechanical terms, the relationship becomes

$$\mu_n = -\frac{\partial E_n}{\partial H} \qquad (2.2)$$

By summing μ_n according the Boltzman distribution law, we then get the macroscopic or bulk molar magnetisation as

$$M = \frac{N\Sigma_n(-\partial E_n/\partial H)\exp(-E_n/kT)}{\Sigma_n \exp(-E_n/kT)} \qquad (2.3)$$

Eq. (2.3) is perhaps the fundamental expression in molecular magnetism, since it is both general and does not involve any approximations. However, it is difficult to apply because in order to calculate the derivatives, the E_n values as a function of the field strength must be known. The equation derived by Van Vleck is based on two approximations:

1) The energies can be expressed as a series of the form

$$E_n = E_n^{(0)} + E_n^{(1)}H + E_n^{(2)}H^2 + \bullet\bullet\bullet \quad (2.4)$$

such that (2.2) now becomes

$$\mu_n = -E_n^{(1)} - 2E_n^{(2)}H + \bullet\bullet\bullet \quad (2.5)$$

2) That $kT >> E_n^{(1)}H + E_n^{(2)}H^2 \bullet\bullet\bullet$, such that

$$\exp(-E_n/kT) = \exp(-E_n^{(0)}/kT)(1 - E_n^{(1)}H/kT) \quad (2.6)$$

If we also assume that in zero field the magnetisation disappears (ie: no spontaneous magnetisation occurs), (2.3) then becomes

$$M = \frac{NH\Sigma_n(E_n^{(1)2}/kT - 2E_n^{(2)})\exp(-E_n^{(0)}/kT)}{\Sigma_n \exp(-E_n^{(0)}/kT)} \quad (2.7)$$

or expressed in terms of the molar magnetic susceptibility

$$\chi_M = \frac{N\Sigma_n(E_n^{(1)2}/kT - 2E_n^{(2)})\exp(-E_n^{(0)}/kT)}{\Sigma_n \exp(-E_n^{(0)}/kT)} \quad (2.8)$$

Equation (2.8) is the Van Vleck formula. To now solve for χ_M, we need only know the $E_n^{(0)}$, $E_n^{(1)}$, and $E_n^{(2)}$ quantities. $E_n^{(0)}$ are the zero field eigenvalues of the spin Hamiltonian used to solve the equation, while $E_n^{(1)}$ and $E_n^{(2)}$ the first- and second-order Zeeman energies, respectively. The first-order Zeeman effect arises from symmetrical splitting of an energy level due to orientation of ions with and against the applied field, and is proportional to the field H. The second order-effect is proportional to H^2 and is the result of mixing between the ground state and some excited state. When the energy separation of these states is >>kT (as it generally is in first row transition metals) population of the upper state

does not occur and the contribution to the magnetisation is temperature independent, and is thus known as temperature independent paramagnetism (TIP).

2.2 Quantitative Expressions for Molecular Magnetism

2.2.1 Introduction

The magnetic exchange between two metal centres in a binuclear complex can be represented by the isotropic Heisenberg-Dirac-Van Vleck Hamiltonian which is generally expressed as

$$H = -2Js_1s_2 \qquad (2.9)$$

where s_1 and s_2 are the local spin quantum numbers and J is the exchange integral between the two centres. This Hamiltonian is valid provided that two criteria are met. First, that the local states have no first order angular momentum, and second that the dominant interaction is the intradimer exchange.

When considering interactions between metal ions, the good spin numbers are those of the dimer rather than of the isolated metal ion. For a homobinuclear system, these new spin quantum numbers are

$$S = 2s, 2s-1, \bullet\bullet\bullet \qquad (2.10)$$

Since

$$S = s_1 + s_2 \qquad (2.11)$$

the Hamiltonian (2.9) can also be written as

$$H = -J(S^2 - s_1^2 - s_2^2) \qquad (2.12)$$

the eigenvalues of which are

$$E(S) = -J(S(S+1)) \qquad (2.13)$$

These are the zero field energies, $E_n^{(0)}$, of interest in the Van Vleck equation.

The procedure for clusters containing more than two metal centres is essentially the same as that for a dimer. However, as the number of centres increases, so does the complexity of the derivation. For example, for a tetranuclear system,[22] the appropriate Hamiltonian is

$$H = -2J_{12}s_1s_2 - 2J_{13}s_1s_3 - 2J_{14}s_1s_4 - 2J_{23}s_2s_3 - 2J_{24}s_2s_4 - 2J_{34}s_3s_4 \qquad (2.14)$$

assuming that all exchange pathways are significant and unique. It should be obvious that the derivation of the energy levels and solution of the Van Vleck equation likewise becomes very complicated very quickly as the number of centres increases.

2.2.2 Magnetic Exchange in Cu(II) and Mn(II) Systems[18]

Magnetic exchange in Cu(II) systems has been extensively investigated, partly because of the relevance to bioinorganic systems, but largely due to the conceptual simplicity of the s = ½ system. For two interacting s = ½ ions, the appropriate spin quantum numbers, according to (2.10), are S=1 and S=0. Furthermore, the energy eigenvalues (2.13) are -2J and 0, respectively, for the two new spin states. The energy diagram, including first-order Zeeman splitting,

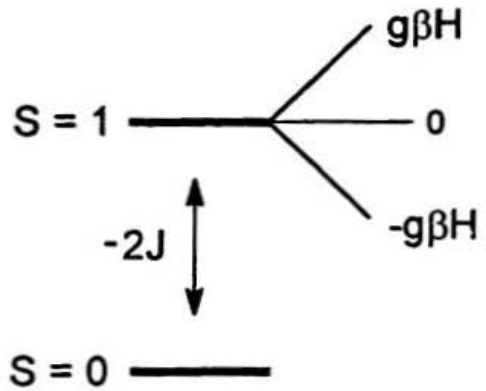

Fig. 2.1 Relative Energies of Spin States in a s = ½ Binuclear System.

for this situation is shown schematically in Fig.2.1. This particular case illustrates an antiferromagnetic system, with the singlet state lower in energy than the triplet. In a ferromagnetic system, the diagram is simply inverted such that the triplet is now lower in energy and the energy difference becomes 2J.

The solution of (2.8) for the s = ½ system yields the Bleaney-Bowers[23] equation for the magnetic susceptibility per metal centre

$$\chi_M = \frac{Ng^2\beta^2}{kT}\left(\frac{1}{3+e^{2x}}\right) + N\alpha \qquad (2.15)$$

where x = (J/kT), and the other symbols have their usual meaning. In practice, the equation generally used is a modified version of (2.15), of the form

$$\chi_M = \left[\frac{Ng^2\beta^2}{k(T-\theta)}\left(\frac{1}{3+e^{2x}}\right)\right](1-\rho) + \left(\frac{Ng^2\beta^2}{4kT}\right)\rho + N\alpha \qquad (2.16)$$

Equation (2.16) takes into account two factors usually observed in experimental magnetic data. Firstly, it includes a term, ρ, which is the fraction of uncoupled or paramagnetic impurity. This is assumed to obey the Curie law and, for the sake of simplicity, have the same molecular weight per metal as the dimer. Secondly,

it includes a Weiss-like correction, θ, which accounts for weak intermolecular interactions.

Another system which is well behaved magnetically is high spin Mn(II). It is a d^5 ion with a single electron in each d orbital. Since it contains no paired electrons, it does not have an orbital contribution to magnetism. As a result, it can be treated similarly to Cu(II). Since each Mn(II) centre has a spin of s = 5/2, the energy level diagram is more complicated, but the new spin quantum numbers and the energy eigenvalues are calculated by the same procedure from (2.10) and (2.13) respectively, as shown in Table 2.1.

Table 2.1 Energy Eigenvalues and First-Order Zeeman Multiplicities for the Spin States of a Mn(II) Binuclear System.

Spin, S	Energy	Zeeman Multiplicity
5	30J	11
4	20J	9
3	12J	7
2	6J	5
1	2J	3
0	0	1

Likewise, an expression for χ_M per metal centre can be derived from the Van Vleck equation and the isotropic spin Hamiltonian (2.9)

$$\chi_M = \left[\frac{Ng^2\beta^2}{k(T-\theta)}\left(\frac{55+30e^{10x}+14e^{18x}+5e^{24x}+e^{28x}}{11+9e^{10x}+7e^{18x}+5e^{24x}+3e^{28x}+e^{30x}}\right)\right](1-\rho) + \left(\frac{35Ng^2\beta^2}{12kT}\right)\rho + N\alpha \qquad (2.17)$$

where the equation has again been modified to include a paramagnetic impurity fraction and a Weiss-like θ correction.

2.2.3 Magnetic Exchange in Ni(II) Systems[24,25]

In contrast to Cu(II) and Mn(II), deriving a relationship to adequately describe the magnetic exchange in a Ni(II) dimer requires consideration of factors beyond the intradimer exchange. In particular, the most dominant feature of Ni(II) magnetochemistry is the zero field splitting (ZFS) of the $^3A_2$ ground state. This arises from the coupling of the ground state with some excited state(s) which results in a splitting of its Zeeman components (Fig. 2.2). It is a consequence of the electrostatic field of the ligands rather than the application of an external field, hence the name zero field splitting.

Since ZFS is often of the same order of magnitude as the intradimer exchange, it must be taken into account when examining Ni(II) dimers. The appropriate Hamiltonian then becomes

$$H_o = -2Js_1s_2 - D(s_{1z}^2 + s_{2z}^2) \qquad (2.18)$$

where D is the zero field splitting and s_{1z} and s_{2z} the z component of the ion spins. If an external field, H, is applied along the x, y, or z axis, then the Hamiltonian becomes

$$H = H_o - g_i\beta HS_i \qquad (2.19)$$

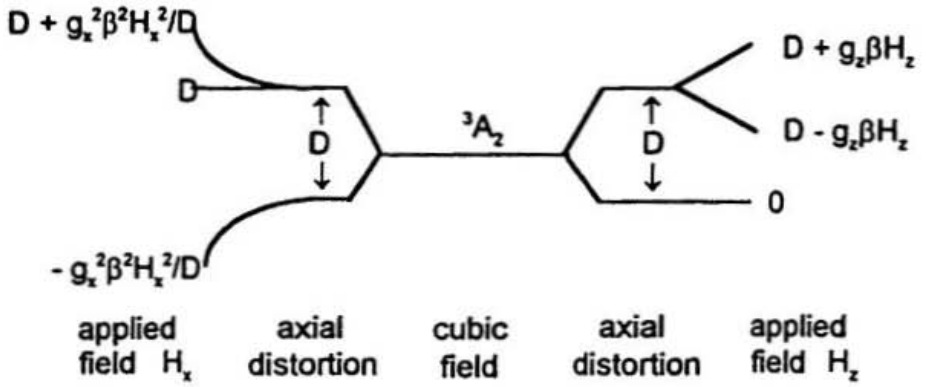

Fig. 2.2 Ni(II) With Axial Distortion and External Applied Field.

where i = x or y or z. When the external field is aligned with the z axis, then the energies can be calculated exactly from first order perturbation theory as

$$E_n = E_{0,n} - g_z\beta H\langle\Psi_{0,n} / S_z / \Psi_{0,n}\rangle \qquad (2.20)$$

When the external field is aligned along either the x or y axis, the first order perturbation energies are zero, and the appropriate energies must be calculated from second order perturbation theory. The resulting energy eigenvalues (see Appendix A) and the Hamiltonian (2.19) yield, on solving the Van Vleck equation, expressions for the x, y, and z components of the magnetic susceptibility

$$\chi_z = \frac{2Ng_z^2\beta^2}{kT}F_1(J,D,T) \qquad (2.21)$$

and

$$\chi_x = \chi_y = 2Ng_x^2\beta^2[\frac{1}{D}F_2(J,D,T) + \frac{3C_2^2}{3J-\delta}F_3(J,D,T) + \frac{3C_1^2}{3J-\delta}F_4(J,D,T)] \qquad (2.22)$$

where C_1, C_2, and δ are coefficients in J and D, and $F_n(J,D,T)$ are temperature dependent functions in J and D, all of which are given in Appendix A. Since, in practice, most magnetic susceptibility measurements are done on powdered samples, it is the averaged susceptibility, χ_{avg}, which is of interest.

$$\chi_{avg} = \frac{1}{3}(\chi_x + \chi_y + \chi_z) \qquad (2.23a)$$

$$\chi_{avg} = \frac{Ng^2\beta^2}{3k}[\frac{1}{T}F_1(J,D,T) + \frac{2}{T}F_2(J,D,T) + \frac{6C_2^2}{3J-\delta}F_3(J,D,T) + \frac{6C_1^2}{3J-\delta}F_4(J,D,T)] + N\alpha \qquad (2.23b)$$

Note that equation (2.23b) also includes a TIP term. As was seen in the Cu(II) and Mn(II) equations, an intermolecular coupling term is often also included in the expression for Ni(II). This can be done by simply including a Weiss-like correction term, but for Ni(II) it can be calculated relatively easily by adding another term to the Hamiltonian (2.19) to account for this.

$$H = H_o - g_i\beta HS_i - 2Z'J'S_i\langle S_i\rangle \qquad (2.24)$$

Proceeding as above, the solution to the Van Vleck equation becomes

$$\chi_{avg} = \frac{Ng^2\beta^2}{3k}[\frac{F_1(J,D,T)}{T-4Z'J'F'(J,D,T)} + \frac{2F'(J,D,T)}{1-4Z'J'F'(J,D,T)}] + N\alpha \qquad (2.25)$$

where F'(J,D,T) is defined in Appendix A.

2.3 Structure and Magnetism: Factors Influencing the Magnitude and Sign of the Isotropic Exchange

One of the goals in the study of molecular magnetism is to understand what geometric and structural factors are responsible for the observed magnetic behaviour of an exchange coupled system. It then becomes possible to design systems with specific and desired magnetic properties. As such, it is imperative to understand that magnetic exchange in a given system occurs between the

unpaired electrons of the paramagnetic centres. Therefore, any attribute which affects the ability of the electrons to communicate or interact with one another will in turn affect the magnitude and sign of the magnetic exchange.

Electronegativity is a measure of the ability of an element to attract or polarise electrons towards itself. By manipulating the electronegativity of the ligands in a complex, it is thus possible to also manipulate the magnetic coupling. An illustrative example of the effect of non-bridging ligands is found in the pair of isostructural complexes $[Cu_2(PTP)Cl_4](CH_3CH_2OH)$[27] and $[Cu_2(PTP)Br_4]$[28] (PTP = 3,6-bis(2'-pyridylthio)pyridazine). The halides in each complex are ligands, two terminal and two forming non-magnetic axial / equatorial bridges. Both are antiferromagnetically coupled through the pyridazine bridge. The bromo compound, however, is more strongly coupled (-2J = 243 cm^{-1}) than the chloro compound (-2J = 131 cm^{-1}), a consequence of chlorine's higher electronegativity, which pulls more electron density away from the magnetic bridge than does bromine. A similar, yet opposite effect occurs for isostructural complexes in which the electronegativity of the bridge itself is varied. For example, Kahn et al.[29] reported a series of binuclear Cu(II) complexes with oxalate, oxamide, and dithiooxamide bridges (Fig.2.3) in which the coupling decreased as the electronegativity of the bridging ligand increased (ie: O<N<S). This is due to the increasing ability of the bridge to "hold up" or resist electron spin exchange.

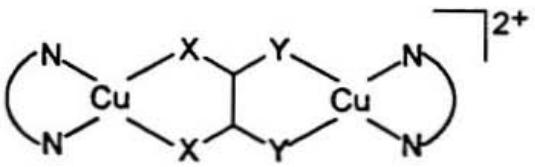

X=Y=O $-2J = 384.5\ cm^{-1}$
X=O, Y=N $-2J = 581 cm^{-1}$
X=S, Y=N $-2J = 594\ cm^{-1}$

Fig. 2.3 Electronegativity of Bridging Ligand vs. -2J for a Series of $Cu_2(C_2X_2Y_2)L_2$ Complexes.

A more fundamental factor than electronegativity is the coordination geometry about the metal ions and the geometry of the bridge(s) responsible for the exchange. Essentially, these are both specific cases of the influence of orbital overlap on magnetic exchange. Consider, for example, the magnetic orbitals of an isolated Cu(II) ion. The d^9 Cu(II) ion has only one unpaired electron, and hence only one magnetic orbital. For square planar, square pyramidal and octahedral geometries, the magnetic orbital is $d_{x^2-y^2}$, while for trigonal bipyramidal it is d_{z^2}. The interaction of the magnetic orbitals of two Cu(II) ions via a bridge will often result in antiferromagnetic coupling. However, if the overlap occurs via a magnetic orbital on one ion and a non-magnetic orbital on another, it is said to be an orthogonal interaction and it can lead at most to ferromagnetic coupling.

Another, and more critical factor, when considering the geometry and subsequent orbital overlap of the metal ions with the bridge(s) propagating the magnetic exchange is accidental orthogonality. In general, orthogonality is best

described as a discontinuity in the exchange pathway which prevents direct interaction of the unpaired spins via orbital overlap. Orthogonality as described concerning the metal ion magnetic orbitals only is known as strict orthogonality. It arises when the two magnetic orbitals transform as different irreducible representations of the same molecular symmetry group. Accidental orthogonality results when the effective overlap between magnetic orbitals is zero, which can occur only for very specific values of the structural parameters.

The classic magnetostructural correlation which illustrates the concept of accidental orthogonality and the influence of bridge geometry on magnetic coupling was reported by Hatfield and Hodgson[30] in the mid 1970's. This involved a series of planar hydroxo-bridged Cu(II) dimers of the type shown in Fig.2.4. Comparing the bridge angle, α, of twelve structurally characterised complexes, they found that as the angle varied from 95.6° to 104.1°, the coupling constant 2J varied from +172 cm^{-1} to -509 cm^{-1} in a linear fashion, according to equation (2.26).

$$2J = 74.53\,\alpha\ (cm^{-1}deg^{-1}) - 7270\ cm^{-1} \qquad (2.26)$$

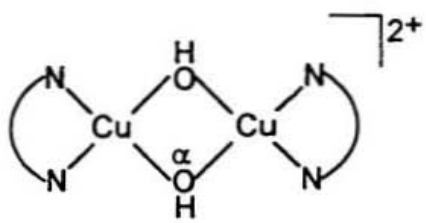

Fig. 2.4 General Structure of the Hydroxy-Bridged Dimers Studied by Hatfield and Hodgson.

This parallels the variation of the orbital overlap with bridge angle. At ~180°, overlap and antiferromagnetic coupling are theoretically at a maximum, while at ~90° there exists accidental orthogonality and exchange is ferromagnetic. Equation (2.26) also predicts that for a bridge angle of α=97.5°, the observed coupling should be zero. Experimentally, it is also noted that above this angle, antiferromagnetic coupling is observed, while below 97.5°, ferromagnetic coupling is observed.

2.4 A Theoretical Model for Magnetic Exchange

When discussing the magnetic behaviour of a given complex, it is common practice to refer to it as being 'antiferromagnetic' or 'ferromagnetic', as the case may be. In practice, however, no complex is simply one or the other, and the observed coupling is a sum total of all the ferromagnetic and antiferromagnetic terms.

$$J = J_F + J_{AF} \tag{2.27}$$

On the basis of Extended Hückel calculations, Hay, Thibeault and Hoffman[31] derived a semiquantitative model to describe the origin of the J_F and J_{AF} terms in a binuclear system. For the general d^n case, the two contributions are

$$J_F = \frac{1}{m^2} \sum_{i \in A} \sum_{j \in B} K_{ij} \tag{2.28}$$

$$J_{AF} = -\frac{1}{m^2} \sum_{i=1}^{m} \frac{\frac{1}{2}(\varepsilon_{2i} - \varepsilon_{2i-1})^2}{J_{ai,ai} - J_{ai,bi}} \tag{2.29}$$

where m is the number of distinct pairs of orbitals from which localised orbitals can be formed, $J_{ai,ai}$, $J_{ai,bi}$ and K_{ij} are two electron integrals, and ε_{2i} and ε_{2i-1} are the energies of the relevant molecular orbitals. While at first glance this model may appear daunting, it becomes much easier to use by making the approximation that the two electron integrals are relatively insensitive to structural or substituent changes in a family of complexes. This leads to a number of useful inferences. First, since the ferromagnetic contribution arises solely from the two electron exchange integrals K_{ij}, it will be constant for a given family of complexes. Similarly, the Coulomb integrals $J_{ai,ai}$ and $J_{ai,bi}$ will also be constant, such that it is the orbital energy term $(\varepsilon_{2i} - \varepsilon_{2i-1})^2$ which is responsible for the variation of magnetic coupling in a given family of structurally related complexes. While this approximation is useful, it also illustrates the limitations of the model. Firstly, ferromagnetism can only be examined indirectly as a function of the antiferromagnetic term. Secondly, since the two electron integrals are treated as unknown constants , different families of complexes cannot be compared.

Even considering these limitations, the model has been used to deduce magnetostructural correlations in a number of dominantly antiferromagnetic systems. As with so many aspects of magnetism, Cu(II) systems have been studied most extensively. For a Cu(II) dimer, the expression for the observed coupling as derived from (2.27), (2.28), and (2.29) is

$$2J = 2K_{ab} - \frac{(\varepsilon_1 - \varepsilon_2)^2}{J_{aa} - J_{ab}} \qquad (2.30)$$

So, as the energy difference $\varepsilon_1 - \varepsilon_2$ (or Δ) increases, the coupling will become more strongly antiferromagnetic, and conversely more weakly antiferromagnetic as Δ decreases. When the two orbitals are degenerate, (2.30) becomes

$$2J = 2K_{ab} \qquad (2.31)$$

so that the observed coupling is the total inherent ferromagnetism of the system. This is the case of accidental orthogonality described earlier. Note that a dominantly ferromagnetic interaction also occurs when the antiferromagnetic term is less than $2K_{ab}$.

To illustrate the utility and validity of this model, let us return now to the dihydroxy-bridged Cu(II) dimer system. This was originally examined theoretically by Hoffman et al.[31] and later by Kahn.[32] Consider first the two singly occupied molecular orbitals (SOMO's) of the dimer. Assuming D_{2h} symmetry, the two orbitals transform as b_{1g} and b_{2u}, as shown in Fig.2.5. The energy variation $(\varepsilon_{b1g} - \varepsilon_{b2u})^2$ is therefore a function of the overlap between the metal d orbital and

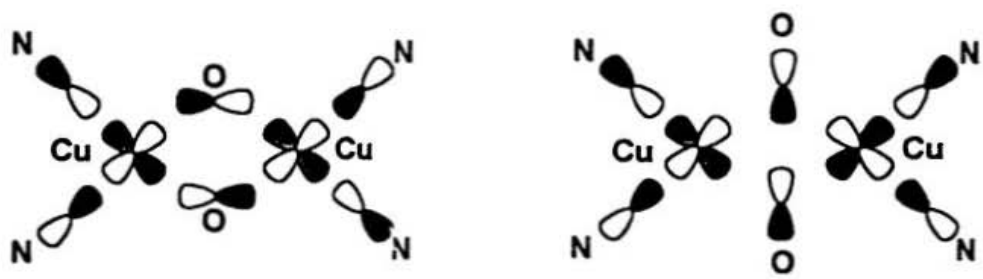

b_{1g} b_{2u}

Fig. 2.5 Singly Occupied MO's for the Dihydroxy-Bridged System.

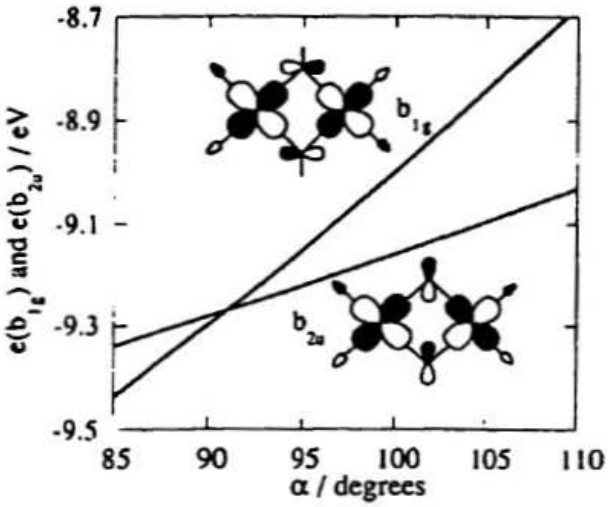

Fig. 2.6 Variation in the Energy of b_{1g} and b_{2u} MO's With Changing Bridge Angle, α.[20]

the oxygen p orbital. The overlap between the metal and ligand orbitals should be equal for b_{1g} and b_{2u} at $\alpha = 90°$, and the two molecular orbitals degenerate and orthogonal. In practice, the angle of accidental orthogonality, α_o, is slightly greater than 90° due to some oxygen 2s orbital contribution to b_{2u} (Fig.2.6). As the bridge angle becomes either larger or smaller than α_o, the energy term Δ^2, and subsequently the antiferromagnetic term, increases. As noted previously, Hatfield and Hodgson found that at $\alpha = 97.5°$, the effective coupling should be zero, due to equal antiferromagnetic and ferromagnetic terms in (2.30). Above this angle, antiferromagnetic coupling dominated. In theory, a similar situation occurs for some angle $\alpha<\alpha_o$, such that below a certain angle the coupling should switch from ferromagnetic to antiferromagnetic. Experimentally, below $\alpha = 97.5°$ all complexes are found to be ferromagnetically coupled. At lower bridge angles,

where antiferromagnetic coupling is expected, the metal-metal separation gets very small and direct metal-metal interactions begin to appear.

The analysis is similar for the general d^n case. The antiferromagnetic term is then, as shown in (2.29), the sum of the contributions of the of the pairs of closely related molecular orbitals (ie: those derived largely from the same metal d orbitals). For example, for the Ni(II) high spin case,[31] equations (2.28) and (2.29) yield

$$2J = \frac{1}{2}(K_{ac} + K_{ad} + K_{bc} + K_{bd}) - \frac{\frac{1}{4}(\varepsilon_1-\varepsilon_2)^2}{J_{aa}-J_{ac}} - \frac{\frac{1}{4}(\varepsilon_3-\varepsilon_4)^2}{J_{bb}-J_{bd}} \qquad (2.32)$$

Here, ε_1 and ε_2 are the energies of the molecular orbitals derived from the x^2-y^2 metal orbitals, and ε_3 and ε_4 are the energies of the z^2 derived molecular orbitals. So, the antiferromagnetic term is due to the separate contributions of difference between the pairs of orbitals Φ_1/Φ_2 and Φ_3/Φ_4. The same procedure can be used for other binuclear metal systems, with comparable results. It is important to note, however, that the contributions of the orbital pairs need not be equal. Consider for example the case in which a Ni(II) dimer has a bridge in the xy plane. The greatest contribution to the antiferromagnetic coupling then comes from the x^2-y^2 term as opposed to the z^2 term, since the z^2 orbitals will only marginally overlap with the orbitals of the bridging ligands.

2.5 Orbital Complemetarity and Countercomplementarity

The semiquantitative model described in the previous section can also be used to help understand the magnetic coupling in a system with two or more dissimilar magnetic bridges. If a binuclear metal centre is bridged by two or more different magnetic bridges, orbital complementarity and countercomplementarity help govern the magnitude of the coupling constant. This is illustrated in Fig.2.7, using model binuclear square planar Cu(II) systems bridged by μ_2-1,1 azide / pyridazine and μ_2-1,1 azide / carboxylate.[33] As already noted, the magnitude and sign of the coupling constant is a function of the energy difference between the symmetric and antisymmetric molecular orbitals. In the binuclear Cu(II) model bridged by a single μ_2-1,1 azide, the azide antisymmetric molecular orbital Φ_{AS} is higher in energy than the symmetric Φ_S. This is true also for the pyridazine bridge. However, in the case of carboxylate, Φ_S is higher in energy than Φ_{AS}. So, in the μ_2-1,1 azide / carboxylate bridged system, the two bridges work to counteract each other, and the resultant observed coupling is much less than it would be for either bridge alone. This is known as orbital countercomplementarity. For the μ_2-1,1 azide / pyridazine bridged system, the opposite is true. The observed coupling is much greater than that for a dimer singly bridged by either one of the ligands, and the two bridges are said to be complementary.

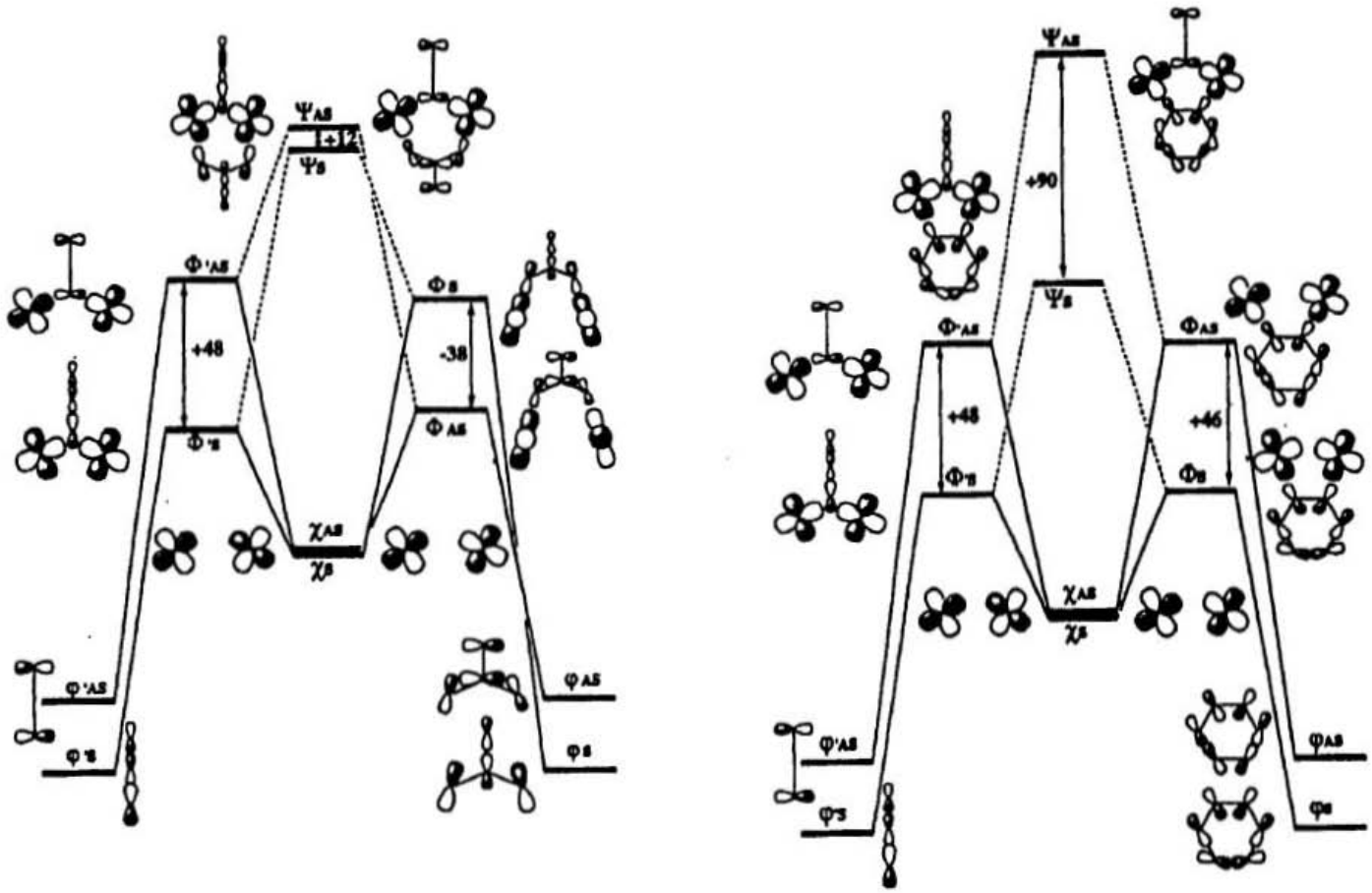

Fig. 2.7 Orbital Complementarity and Countercomplementarity (a) MO Diagram for μ_2-1,1 Azide / Carboxylate Bridged Dimer (b) MO Diagram for μ_2-1,1 Azide / Pyrdiazine Bridged Dimer.[33]

Chapter 3. Azide and Thiocyanate Bridged Metal Complexes

3.1 Magnetic Exchange Via Azide and Thiocyanate Bridges

The azide group is known to bond to metal centres in a number of ways: as a terminal ligand via a single nitrogen, as a μ_2-1,1 or μ_3-1,1 bridge via a single nitrogen, and as a μ_2-1,3 bridge via the two peripheral nitrogen atoms. The μ_3-1,1 bridging mode is quite rare, occurring most notably in a series of tetranuclear cubane-like complexes of Ni(II)[34] and Pt(II).[35] Terminal azide, and μ_2-1,1 and μ_2-1,3 bridging ligands are much more prevalent, and can often occur simultaneously in the same complex. In binuclear complexes, the combination of terminal ligand and a single bridging mode is quite common, while the combination of μ_2-1,1 and μ_2-1,3 bridges (sometimes with terminal ligands as well) is found much less frequently,[36-38] although a number of chain systems containing alternating μ_2-1,1 and μ_2-1,3 bridges are known.[39-45] Even more infrequent is the situation in which a single azide ligand acts as both a μ_2-1,1 and μ_2-1,3 bridge simultaneously.[45]

Paralleling the variety of bonding modes is the variety of magnetic behaviour observed for azide bridged complexes. Complexes containing μ_2-1,3 bridges are noted for propagating antiferromagnetic exchange, quite strong in many cases. In fact, symmetrically dibridged planar Cu(II) / μ_2-1,3 azide dimers (Fig. 3.1(a), δ = 0) are so strongly coupled that they are effectively diamagnetic.[46-49] Similar behaviour is also observed in dimers of other metals.

For example, strong antiferromagnetic coupling is observed for both Ni(II)[50] and Mn(II)[39] planar μ_2-1,3 bridged dimers, with the coupling becoming weaker as the dihedral angle, δ, increases. This correlation is reflected in Extended Hückel molecular orbital calculations[39,51] which predict maximum coupling at $\delta = 0$, then a gradual decrease to a minimum at $\delta = \sim 60°$. In fact, in the Ni(II) case,[51] $\delta = 60°$ is the angle of accidental orthogonality, such that ferromagnetic exchange should be observed, although no structures have yet been reported with an angle in this area.

Antiferromagnetic exchange is also observed for metal dimers bridged by a single μ_2-1,3 azide (Fig.3.1(b)). In the Cu(II) case, the coupling is again strong, but generally not as intense as that observed in the dibridged case.[49] A similar situation is observed again for Ni(II) and Mn(II). Extended Hückel molecular orbital calculations indicate maximum antiferromagnetic coupling at $\beta = 110°$ (Mn)[52] and $\beta = 108°$ (Ni),[53] decreasing to a minimum coupling at $\beta = 160°$ for Mn(II) and accidental orthogonality at $\beta = 164°$ for Ni(II). Again, however, no

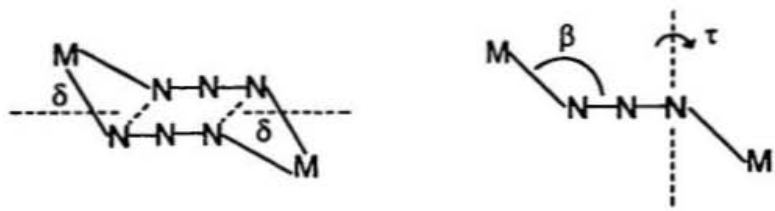

(a) (b)

Fig. 3.1 μ_2-1,3 Azide Bridges. (a) Symmetrical Dibridged (b) Single Bridge.

experimental confirmation of ferromagnetic coupling in the Ni(II) case is known. The coupling in both cases is also dependent on the M-N-N / N-N-M torsion angle, τ, with a maximum at $\tau = 0°$ (ie: planar), and a gradual decrease as τ increases. This is in good agreement with the dibridged case, since varying the dihedral angle δ is essentially a combination of varying the angles β and τ.

The previous discussion assumes, of course, that the azide is bridging between two magnetically active orbitals. While this is not relevant for Ni(II) and Mn(II), a number of Cu(II) / μ_2-1,3 bridged dimers are known[38,49] which contain a square pyramidal or octahedral array of ligands with axial / equatorial bridges. The coupling in these cases is effectively zero, although some weak interaction is occasionally observed. A similar condition is observed when bridging occurs via two axial contacts.[54,55]

Metal dimers containing μ_2-1,1 azide bridges show an even more remarkable dependence of magnetic behaviour on bridge geometry. Early studies of Cu(II) dimers bridged by two μ_2-1,1 azides revealed ferromagnetic coupling.[47,56,57] This ferromagnetism was justified by invoking an accidental orthogonality argument, similar to that used to explain the observed magnetic behaviour in the structurally related dihydroxy dimers.[30-32] The angle of accidental orthogonality was calculated by Extended Hückel methods to be ~103° (Fig.3.2), somewhat larger than in the dihydroxy bridged series, a consequence of the less electronegative nitrogen bridge.[32,47] The model was also

consistent with the experimental data, since the observed bridge angles fell around 103° (100.5° - 105.46°), where ferromagnetic behaviour is expected. However, a separate study[56] proposed that **all** μ_2-1,1 bridged Cu(II) dimers should exhibit ferromagnetism, regardless of the bridge angle. It was argued that since the splitting (Δ) between the two SOMO's was quite small compared to the dihydroxy bridged case, the antiferromagnetic contribution would always be insignificant, and the observed exchange would be ferromagnetic due to spin polarisation (Fig.3.3). This states that in the free azide ion, the two electrons in the π_g HOMO are localised at the extreme ends of the ion, one with α spin and one with β spin. When the azide is bridging between two metal ions, these electrons would be partially delocalized towards the two metal $d_{x^2-y^2}$ orbitals.

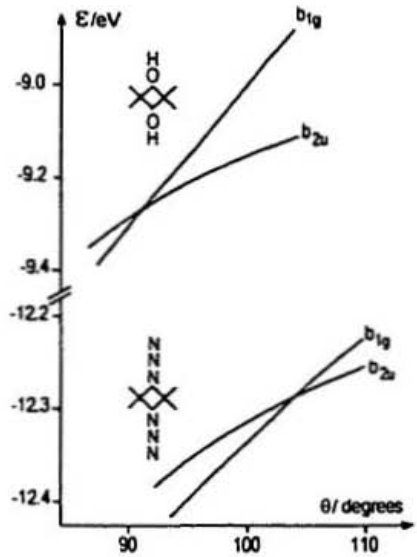

Fig. 3.2 Variation in Energy of b_{1g} and b_{2u} MO's and Accidental Orthogonality for μ_2-1,1 Azide and Dihydroxy Bridged Complexes.[32]

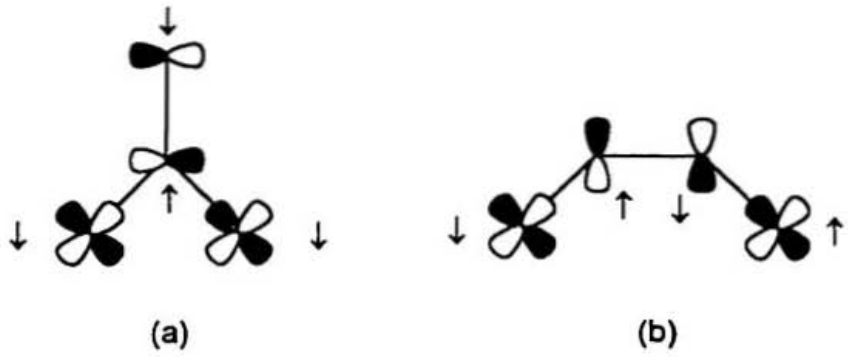

Fig. 3.3 Spin Polarization in Azide Bridged Complexes. (a) μ_2-1,1 Bridge (b) μ_2-1,3 Bridge.

Therefore, the spin of the unpaired electron(s) on the metals align themselves, at greater than 50% probability, with spin opposite to that of the azide electron(s). This would result in all μ_2-1,1 azide complexes being ferromagnetic, and all μ_2-1,3 azide complexes being antiferromagnetic.

The contention over the mechanism controlling spin exchange stemmed from both the paucity of structures available and on the lack of control over the μ_2-1,1 bridge angles in the reported complexes. The terminal, N-donor chelate ligands imposed no geometric constraint on the azide bridge angle, and inevitably the angles fell around the angle of accidental orthogonality. Recent studies,[58,59] however, of μ_2-1,1 bridged systems incorporating N_4 diazine primary ligands which allowed systematic control of the azide bridge angle from 98.3° - 124.1°, has established a thus far elusive antiferromagnetic realm for the μ_2-1,1 azide system, with coupling of $-2J > 900$ cm^{-1} for an angle of 124.1°, and a linear

correlation of azide bridge angle with the magnitude of the coupling constant (Fig. 3.4). The observed crossover is ~108°, somewhat larger than the 103° predicted, this being due to orbital complementarity of the diazine and azide bridges. In addition, a recent report of a polarised neutron diffraction study on $[Cu_2(t\text{-bupy})_4(\mu_2\text{-}1,1\text{-}N_3)_2](ClO_4)_2$[60] revealed spin density calculations that are not consistent with the electron density as predicted by spin polarisation theory.

A similar problem has plagued the study of μ_2-1,1 azide bridged complexes of other first row transition metals. The early trend observed for Cu(II), that μ_2-1,3 bridges propagate antiferromagnetic exchange while μ_2-1,1 bridges propagate ferromagnetic exchange, is general for other metals. The most extensively studied systems after Cu(II) have been Ni(II) and Mn(II), but

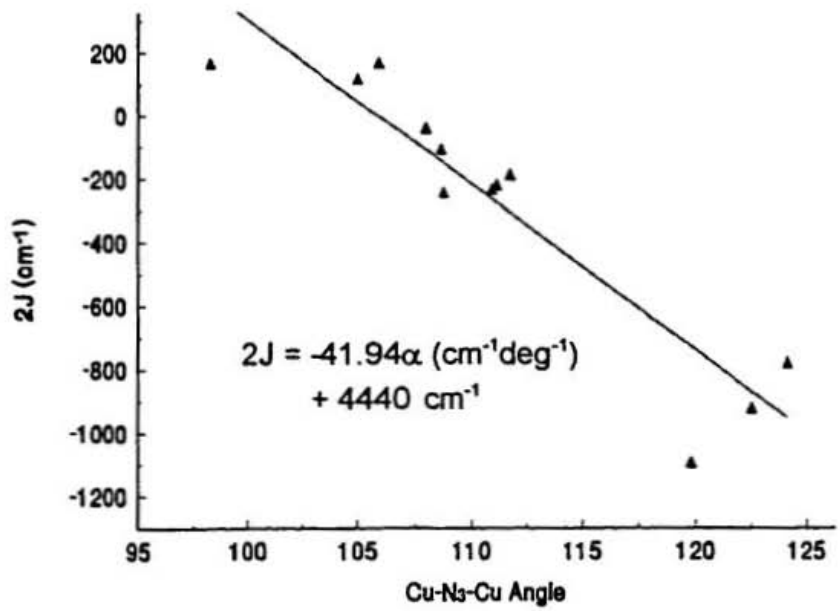

Fig. 3.4 Plot of 2J (cm^{-1}) vs Cu-N_3-Cu Bridge Angle (°) For Binuclear Cu(II) Complexes Containing One μ_2-1,1 Azide Bridge and a Second Diazine Bridge, Along with the Equation of the Best Fit Line.[58,59]

Table 3.1 Representative Binuclear and 1D Chain Ni(II) and Mn(II) Complexes Containing μ_2-1,1 Azide Bridges.

†Complex	M-N_3-M Angle (°)	J (cm^{-1})	Ref.
$[Ni(terpy)(N_3)_2]_2(H_2O)_2$	101.3(3)	20.1	61
$[Ni(pepci)(N_3)_2]_2$	102.2(2) 101.0(2)	36.3	62
$[Ni(Medpt)(N_3)]_2$	104.0(1)	46.7	63
$[(Ni_2(L1)_2(N_3)_3](ClO_4)$	85.8(1) 87.0(1) 85.0(1)	30.7	64
$[Ni(232\text{-}tet)(N_3)]_2(PF_6)_2$	104.6(3)	34.3	65
$[Ni(en)_2(N_3)]_2(ClO_4)_2$	104.3(2)	20.9	66
$[Ni(en)(N_3)_2]_n$	103(1) 95.2(9) 103(2) 101(1)	14.8	66
$[Ni(tn)(N_3)_2]_n$	105.0(8) 101.4(1)	17.6	66
$[Ni(Me_3[12]N_3)(N_3)]_2(ClO_4)_2(H_2O)_2$	103.8(3)	43.9	67
$[Ni(232\text{-}tet)(N_3)]_2(ClO_4)_2$	104.9(2)	33.8	67
$[Ni_2(L2)(N_3)_3]$	86.2	17.2	68
$[Ni_2(terpy)_2(N_3)_3(H_2O)](ClO_4)(H_2O)$	103	13.6	69
$[Mn(terpy)(N_3)_2]_2(H_2O)_2$	104.6(1)	2.43	70

† terpy = 2,2':6'2''-terpyridine
pepci = N'-(2-pyridin-2-ylethyl)pyridine-2-carbaldimine
Medpt = methyl(bis(3-aminopropyl))amine
L1 = 1,4,7-trimethyl-1,4,7-triazacyclononane
232-tet = N,N'-bis(2-aminoethyl)-1,3-propanediamine
en = ethylenediamine
tn = 1,3-diaminopropane
$Me_3[12]N_3$ = 2,4,4-trimethyl-1,5,9-triazacyclododec-1-ene
L2 = bis(N,N'-dimethyl-1,4,7-triazacyclononane)calix[4]arene

only a relatively narrow range of μ_2-1,1 bridge angles have been reported (Table 3.1) for much the same reason as the early Cu(II) complexes: there is no means in these complexes of controlling the bridge angle, the value being left to chance. As a result, all known Ni(II) and Mn(II) complexes bridged solely by μ_2-1,1 azide are ferromagnetically coupled, and this observed magnetism has been variously ascribed to either accidental orthogonality or spin polarisation. A report of an alternating μ_2-1,1 / μ_2-1,3 Ni(II) chain with a very small μ_2-1,1 azide angle (84.2°),[41] however, showed that the magnetic data could be fitted sensibly only if the coupling through the μ_2-1,1 bridge is assumed to be antiferromagnetic, an observation which would appear to lend support to the accidental orthogonality model.

A much wider range of μ_2-1,1 bridge angles has been examined theoretically by Extended Hückel molecular orbital calculations. A recent study[39] of a Mn(II) / μ_2-1,1 azide model complex examined the effect of bridge bond symmetry and bridge angle on the antiferromagnetic component of the exchange. It was found that the $\Sigma\Delta^2$, and hence the antiferromagnetic component of the coupling, decreased essentially linearly with increasing bond asymmetry, and that it also decreased as the bridge angle decreased over the range 110° - 80°. However, examining the magnetic orbital most directly interacting with the azide bridge (d_{xy}) a situation of accidental orthogonality is observed at 105°, which implies the presence of an antiferromagnetic realm at bridge angles

sufficiently above or below 105°. The observed ferromagnetism for the only isolated Mn(II) / μ_2-1,1 azide dimer reported is reasonable by this argument, since it shows a bond angle of 104.6(1)°, right at the angle of accidental orthogonality. A previous study[69] by the same authors on a Ni(II) / μ_2-1,1 azide model system suggested a maximum antiferromagnetic coupling at 85°, decreasing to a minimum at 115°. No details of the model were reported, however, so it is uncertain if both magnetic orbitals were examined or just the most directly relevant orbital, as in the Mn(II) study.

Both Ni(II) and Mn(II) also form a number of thiocyanate bridged complexes. In contrast to azide complexes of these metals, μ_2(N)-1,1 thiocyanate bridged systems are quite rare, and the magnetic exchange through these bridges is not well understood. In general, however, magnetic exchange through the μ_2(N)-1,1 thiocyanate bridge is quite weak. Just one complex of Ni(II) containing only μ_2(N)-1,1 thiocyanate bridges is known,[71] but no magnetic data are reported. There are several Ni(II) complexes, however, which contain μ_2(N)-1,1 thiocyanates with other bridges. The trinuclear complex[72] $[Ni_3(NCS)_6(detrH)_6](H_2O)_2$ (detrH = 3,5-diethyl-1,2,4-triazole) contains both μ_2(N)-1,1 thiocyanate and triazole diazine bridges, and exhibits weak ferromagnetism. Since the diazine moiety is known to propagate antiferromagnetic exchange, the ferromagnetism would appear to be a function of the μ_2(N)-1,1 thiocyanate bridge. The tetranuclear complex[73]

Table 3.2 Representative Binuclear and 1D Chain Ni(II) and Mn(II) Complexes Containing μ_2(N,S)-1,3 Thiocyanate Bridges.

Complex†	β_1 (°)	β_2 (°)	J (cm^{-1})	Ref.
$[Ni(en)_2(NCS)]_2I_2$	167	100	4.5	25
$[Ni(tren)(NCS)]_2(BPh_4)_2$	167	100	2.4	77
$[Ni(terpy)(NCS)_2]_2$	159(2)	100.0(8)	4.9	78
[*catena*-$(NCS)(Ni(en)_2]_n(PF_6)_n$	171.5(3)	100.8(2)	0.2	79
$[Ni(Medpt)(NCS)_2]_n$	161.5(6)	100.5(1)	1.12	80
$[Ni_2(Me_2en)_3(NCS)_4]$	142.4(3) 165.2(3)	105.8(1) 100.7(1)	6.3	81
$[Ni_1(Me_2en)_2(NCS)]_2(PF_6)_2$	167.9(4) 165.6(4)	99.4(2) 93.1(2)	4.3	81
$[Mn(tren)(NCS)]_2(BPh_4)_2$	161.2(4)	‡	-0.2	82
$[Mn(SCN)_2(CH_3CH_2OH)_2]_n$	169.0(1)	103.6(1)	-1.3	83

† Me_2en = 1,2-diamino-2-methylpropane
Other abbreviations given in Table 3.1

‡ Data not reported

$[Ni_4L3(NCS)_2(H_2O)_2](ClO_4)_2(CH_3CN)_2$ (L3 = 36-membered octaaminotetraphenol macrocycle) consists of two binuclear asymmetric units in which the Ni(II) centres are bridged by phenoxide, water, and μ_2(N)-1,1 thiocyanate, and exhibits moderate antiferromagnetic exchange. Since both phenoxide and water bridges are known to propagate moderate to strong antiferromagnetic exchange in Ni(II) systems, the sign of any weak contribution from the μ_2(N)-1,1 thiocyanate is

Fig. 3.5 **μ_2(N,S)-1,3 Thiocyanate Bridge Geometries. (a) Retangular (b) Trapazoidal.**

difficult to determine. A similar paucity of both structural and magnetic data exists for Mn(II) μ_2(N)-1,1 thiocyanates,[74-76] although it is interesting to note that in several systems with both μ_2(N)-1,1 thiocyanate and alkoxy bridges, the coupling is effectively zero.[75,76]

Although in many ways structurally analogous to μ_2-1,3 azide bridged Ni(II) and Mn(II) complexes, the magnetic behaviour of the μ_2(N,S)-1,3 bridged Ni(II) complexes is quite different (Table 3.2). To date, all reported μ_2(N,S)-1,3 bridged Ni(II) complexes are weakly ferromagnetically coupled, in contrast to the strong antiferromagnetic coupling observed in μ_2-1,3 azide bridged Ni(II) systems. For Ni(II), the structures of all of the known μ_2(N,S)-1,3 thiocyanate complexes are close to the idealised rectangular structure shown schematically in Fig.3.5(a). As noted by Ginsberg[25] in his classical work interpreting ferromagnetic coupling in $[Ni(en)_2(NCS)]_2I_2$, this arrangement should give ferromagnetic coupling on the basis of either the Goodenough-Kanamori[84] rules or Anderson's expanded orbital theory.[85] More recent Extended Hückel molecular orbital calculations[81] support this interpretation, showing accidental orthogonality at geometries approximating Fig.3.5(a). The magnetic orbitals remain essentially

degenerate even as the model structure moves from planar to a chair form similar to that shown for μ_2-1,3 azide in Fig.3.1(a). It is only as the geometry moves towards trapezoidal (Fig.3.4(b)) that any significant increase in the $\Sigma\Delta^2$ values is observed, suggesting the possibility of an antiferromagnetic realm. This has, however, not been confirmed experimentally.

On the other hand, Mn(II) / μ_2(N,S)-1,3 bridged complexes are weakly antiferromagnetically coupled (Table 3.2). This is a function of the Mn(II) d_{yz} and d_{xz} magnetic orbitals, not present in Ni(II), which overlap with the thiocyanate orbitals and prevent strict orthogonality as observed for Ni(II). Extended Hückel molecular orbital calculations[52] show that for geometries which result in orthogonality and hence ferromagnetic coupling in Ni(II) systems, the Mn(II) / μ_2(N,S)-1,3 system exhibits relatively significant $\Sigma\Delta^2$ values, suggesting antiferromagnetic exchange, as is observed.

3.2 The Objectives of This Study

The objectives of the study reported in this thesis are twofold. Firstly, it was desired to examine more closely the magnetic behaviour of the μ_2-1,1 azide / diazine bridged Cu(II) system. The ferromagnetic realm at angles <~108° and the antiferromagnetic realm at >~108° are now well established,[58,59] but the magnetic behaviour at angles near the angle of magnetic crossover is not clearly understood. It has been found that for weakly antiferromagnetically coupled

systems with angles ~108°, it is difficult to fit the magnetic data to the Bleaney-Bowers equation (2.16).[38,59] In order to further investigate this anomaly, a series of binuclear Cu(II) complexes of the ligand 1,4-bis(3'-methyl-2'-pyridyl)aminophthalazine (PAP3Me), shown in Fig.3.6(a), were synthesised. Since it is found that azide complexes of the analogous 6-methyl ligand PAP6Me have relatively large Cu-Cu separations and μ_2-1,1 azide angles due to steric influence of the 6-methyl moiety,[58,59] the ligand PAP3Me was chosen in the hopes that the 3-methyl moiety would act to reduce the Cu-Cu separation, and hence μ_2-1,1 azide angle, in a similar yet opposite manor. This should give complexes with angles very near the magnetic crossover angle.

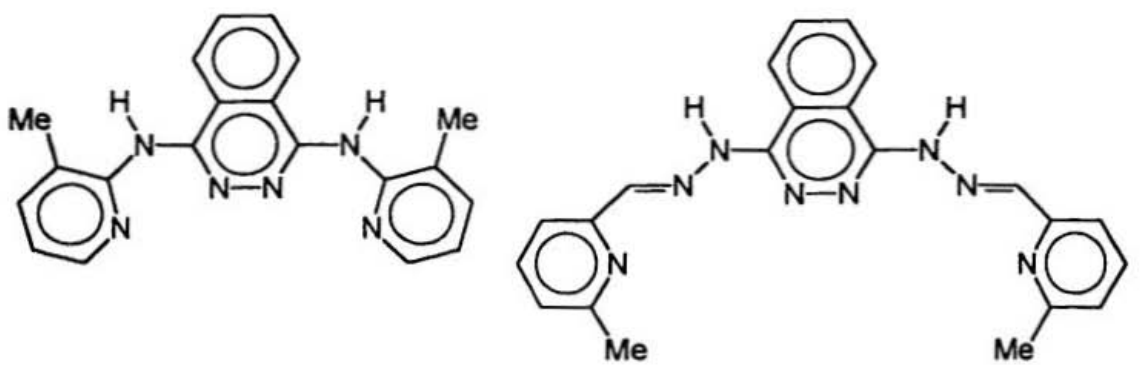

(a) **(b)**

Fig. 3.6 The Ligands Used in This Study. (a) 1,4-bis(3'-methyl -2'-pyridyl)aminophthalazine (PAP3Me) (b) 1,4-bis((6-methyl pyridine -2-carboxaldiimino)amino)phthalazine (PHP6Me).

Secondly, the magnetochemistry of some binuclear Ni(II) and Mn(II) azide and thiocyanate complexes of the ligand 1,4-bis((6-methylpyridine-2-carboxaldiimino)amino)phthalazine (PHP6Me), shown in Fig.3.6(b), was investigated. It was hoped to establish an antiferromagnetic realm for μ_2-1,1 azide complexes of other transition metals besides Cu(II), as well as further investigate the magnetic properties of the μ_2(N)-1,1 thiocyanate bridge. The ligand PHP6Me was chosen for several reasons. As a hexadentate ligand, it is better able to give the octahedral geometry preferred by Ni(II) and Mn(II) than a similar tetradentate system, such that control of the geometry of the binuclear centre is more straightforward. The 6-methyl ligand, in particular, was again chosen for steric reasons. The ligand PHP6Me has been observed[86] to form 2:1 ligand / metal complexes containing exogenous bridges with Ni(II), while the analogous ligand APHP (APHP = 1,4-bis((pyrid-2-ylacetaldiimino)amino) phthalazine) often gives 1:1 ligand metal complexes with no exogenous bridges. It is thought that this is due to the steric effect of the 6-methyl moiety which makes the formation of the 1:1 system energetically unfavourable. Since this study is concerned with the magnetic behaviour of the exogenous azide and thiocyanate bridges, the formation of 2:1 complexes is desired.

Part B. Experimental Results and Discussion

Physical Measurements and General Comments

Infrared spectra over the range 4000 cm^{-1} to 400 cm^{-1} were recorded as Nujol mulls on KBr plates using a Mattson Polaris FT-IR instrument. Far Infrared spectra over the range 500 cm^{-1} to 200 cm^{-1} were recorded as Nujol mulls on CsI plates using a Perkin-Elmer Model 283 instrument. Solution UV / Vis spectra were recorded using matched quartz cells (0.1 cm or 1.0 cm) and solid state spectra as Nujol mulls on a Cary 5E spectrometer. Powder and solution (DMF) ESR spectra were recorded with a Brüker ESP300 X-band spectrometer at room temperature. X-ray crystal diffraction data were obtained on either a Rigaku AFC6S diffractometer or a Siemens SMART three-circle diffractometer with a CCD area detector, using graphite monochromated Mo Kα radiation.

Magnetic susceptibility data were collected on vacuum dried samples of the complexes. Room temperature magnetic susceptibilities were recorded by the Faraday method using a Cahn 7600 Faraday Magnetic Balance. Variable temperature magnetic data in the range 4-300K were collected using an Oxford Instruments Superconducting Faraday Susceptometer equipped with a Sartorius 4432 microbalance, employing a main solenoid field of 1.5T and a gradient field of 10 $T \cdot m^{-1}$. The experimental χ_M vs. T data are reported in Appendix D. $Hg[Co(NCS)_4]$ was used as a calibration standard for both instruments, and

temperature errors for the variable temperature data were determined with $[TMENH_2][CuCl_4]$.

Elemental analyses (C,H,N) on vacuum dried samples were performed by Canadian Microanalytical Service, Delta, BC, Canada.

Commercially available reagents were used as received without further purification.

Extended Hückel molecular orbital calculations were carried out using the Extended Hückel program (EHC) and computer-aided composition of atomic orbitals (CACAO) program of Mealli and Proserpio.[87] The parameters for the optimised Slater type orbitals were provided by Dr. Francesc Lloret,[88] and are reported with the internal coordinate input files in Appendix E.

Caution !

Both perchlorate and azide compounds are potentially explosive and should be treated with care and used only in small quantities. In particular, $Cu(N_3)_2$ and many other simple ionic metal azides are explosive, so care must be taken to avoid using an excess of metal salt and azide during the synthesis of metal complexes. All azide and perchlorate complexes reported herein were tested by controlled mechanical impact to ensure their stability.

Chapter 4. Cu(II) Complexes of the Ligand PAP3Me

4.1 Synthesis of the Ligand and Complexes

The ligand 1,4-bis(3'-methyl-2'-pyridyl)aminophthalazine (PAP3Me) was prepared using the literature procedure,[26] by fusion of phthalonitrile and 2-amino-3-picoline, followed by ring expansion of the resulting isoindoline to the phthalazine with hydrazine hydrate in methanol.

$[Cu_4(PAP3Me\text{-}H)_2(N_3)_6]$ **(1)**

A solution of $Cu(CH_3COO)_2 \cdot H_2O$ (0.100g, 0.580mmol) in hot CH_3OH (25mL) was added to a solution of PAP3Me (0.050g, 0.150mmol) in hot CH_2Cl_2 (25mL) to give a blue-green solution. Subsequent addition of a solution of NaN_3 (0.035g, 0.540mmol) in hot CH_3OH (10mL) gave a dark green solution. A green microcrystalline product formed overnight. This was filtered off, washed with CH_2Cl_2 and CH_3OH, and recrystallised by slow diffusion of CH_3OH into a DMF solution to give dark green, well formed crystals. Yield: 0.060g (67%). Anal. Calc'd for $[Cu_4(C_{20}H_{17}N_6)_2(N_3)_6]$, C: 40.40 H: 2.89 N: 35.34; Found, C: 40.89 H: 3.09 N: 35.11.

$[Cu_4(PAP3Me)_2(N_3)_4(NO_3)_2(H_2O)_2](NO_3)_2$ **(2)**

A solution of $Cu(NO_3)_2 \cdot 3H_2O$ (0.168g, 0.700mmol) in hot CH_3OH (40mL) was added to a solution of PAP3Me (0.121g, 0.350mmol) in hot CH_2Cl_2 (40mL) to

give a dark aqua-green solution. Subsequent addition of a solution of NaN_3 (0.043g, 0.660mmol) in hot CH_3OH (10mL) gave a dark green solution. This was heated for several minutes, and then filtered. A green crystalline product formed overnight, which was filtered off and washed with a little cold CH_3OH and CH_2Cl_2. Yield: 0.127g (52%). Anal. Calc'd for $[Cu_4(C_{20}H_{18}N_6)_2(N_3)_4(NO_3)_2(H_2O)_2](NO_3)_2$, C: 34.53 H: 2.90 N: 28.19; Found, C: 34.52 H: 2.87 N: 27.49. The crystal structure shows additional lattice H_2O which was lost on vacuum drying prior to elemental analysis.

$[Cu_2(PAP3Me)(N_3)_3(CH_3OH)](ClO_4)(H_2O)$ **(3)**

A solution of $Cu(ClO_4)_2 \cdot 6H_2O$ (0.200g, 0.540mmol) in hot CH_3OH (25mL) was added to a solution of PAP3Me (0.050g, 0.150mmol) in hot CH_2Cl_2 (25mL) to give a green solution. Subsequent addition of a solution of NaN_3 (0.035g, 0.540mmol) in hot CH_3OH (5mL) gave a dark green solution, with a small amount of dark brown precipitate. This precipitate was filtered off, and the solution left overnight to give dark green crystals. These were filtered off and washed with a little CH_2Cl_2 and CH_3OH. Yield: 0.100g (90%). Anal. Calc'd for $[Cu_2(C_{20}H_{18}N_6)(N_3)_3(CH_3OH)](ClO_4)(H_2O)$, C: 33.85 H: 3.25 N: 28.20; Found, C: 33.77 H: 2.79 N: 28.89. The crystal structure shows a poorly resolved lattice fragment which is likely due to lattice solvent, as observed in the elemental analysis.

$[Cu_2(PAP3Me)(N_3)_2Cl_2](CH_3OH)_{1.5}$ (4)

A solution of $CuCl_2 \cdot 2H_2O$ (0.122g, 0.720mmol) in hot CH_3OH (20mL) was added to a solution of PAP3Me (0.120g, 0.350mmol) in hot CH_2Cl_2 (20mL) to give a green solution. Subsequent addition of a solution of NaN_3 (0.045g, 0.700mmol) in hot CH_3OH (10mL) gave a darker green solution. This was heated for several minutes, and then filtered. A green microcrystalline product formed overnight, which was filtered and washed with cold CH_3OH / H_2O. Yield: 0.080g (34%). Anal. Calc'd for $[Cu_2(C_{20}H_{18}N_6)(N_3)_2Cl_2](CH_3OH)_{1.5}$, C: 38.39 H: 3.60 N: 24.99; Found, C: 38.56 H: 2.95 N: 24.26.

$[Cu_4(PAP3Me)_2(N_3)_5Br_3]$ (5)

$CuBr_2$ (0.154g, 0.700mmol) and PAP3Me (0.122g, 0.350mmol) were both dissolved in hot CH_3OH (50 mL) to give a dark green solution. Subsequent addition of a solution of NaN_3 (0.046g, 0.700mmol) in H_2O (5mL) resulted in no visible change in the solution. This solution was heated for several minutes and then filtered. After several days, a dark green microcrystalline product had formed, which was filtered off and washed with a little cold CH_3OH. Yield: 0.100g (41%). Anal. Calc'd for $[Cu_4(C_{20}H_{18}N_6)_2(N_3)_5Br_3]$, C: 34.59 H: 2.62 N: 27.23; Found, C: 34.37 H: 2.86 N: 27.31.

$[Cu_2(PAP3Me)(SO_4)_2(H_2O)_4](H_2O)$ **(6)**

PAP3Me (0.170g, 0.500mmol) was added to a solution of $CuSO_4 \cdot 5H_2O$ (0.250g, 1.00mmol) in H_2O / CH_3OH (40mL / 5mL). The resulting suspension was heated for ~20 minutes until nearly all of the ligand had dissolved, and was then filtered to remove excess ligand. The resulting green solution was reduced in volume to ~10mL and left to cool, giving an emerald green microcrystalline product after several days. This was filtered off and washed with a little cold CH_3OH. X-ray quality crystals were prepared by diethyl ether diffusion into a CH_3OH / H_2O solution of the product. Yield: 0.090g (24%). Anal. Calc'd for $[Cu_2(C_{20}H_{18}N_6)(SO_4)_2(H_2O)_4](H_2O)$, C: 31.95 H: 3.76 N: 11.18; Found, C: 31.88 H: 3.64 N: 11.02. The crystal structure shows additional lattice water $(H_2O)_{0.5}$ which was lost on vacuum drying prior to elemental analysis.

$[Cu_2(PAP3Me)Cl_4]$ **(7)**

A solution of $CuCl_2 \cdot 2H_2O$ (0.169g, 1.00mmol) in CH_3OH (20mL) was added to a solution of PAP3Me (0.170g, 0.500mmol) in hot CH_2Cl_2 (30mL) to give a forest green coloured solution. This was heated for several minutes and then filtered. A green precipitate formed upon cooling, which was filtered off and washed with a little cold CH_3OH. Yield: 0.200g (65%). Anal. Calc'd for $[Cu_2(C_{20}H_{18}N_6)Cl_4]$, C: 39.29 H: 2.97 N: 13.75; Found, C: 39.15 H: 3.06 N: 13.45.

$[Cu_2(PAP3Me)(OH)(NO_3)_3](H_2O)$ (8) and $[Cu_2(PAP3Me)(OH)Br_3]$ (9)

A solution of $Cu(NO_3)_2 \cdot 3H_2O$ (0.240g, 1.00mmol) in CH_3OH (20mL) was added to a suspension of PAP3Me (0.170g, 0.500mmol) in H_2O (10mL). This mixture was heated for ~15 minutes until nearly all of the ligand had dissolved, and was then filtered to remove the excess ligand. After about a week, a blue-green crystalline product had formed, which was filtered off and washed with a little cold CH_3OH. Yield: 0.060g (17%). Anal. Calc'd for $[Cu_2(C_{20}H_{18}N_6)(OH)(NO_3)_3](H_2O)$, C:34.78 H: 3.07 N: 18.26; Found, C: 34.99 H: 3.10 N: 18.38.

$[Cu_2(PAP3Me)(OH)Br_3]$ (9) was prepared by the same procedure, using $CuBr_2$ (0.233g, 1.00mmol) to give a dark green crystalline product. Yield: 0.015g (4%). Anal. Calc'd for $[Cu_2(C_{20}H_{18}N_6)(OH)Br_3]$, C: 33.07 H: 2.64 N: 11.57; Found, C: 33.08 H: 3.06 N: 11.58.

4.2 X-Ray Crystallography

4.2.1 X-Ray Crystal Structures of the Cu(II) / PAP3Me Complexes

$[Cu_4(PAP3Me\text{-}H)_2(N_3)_6]$ (1)

The structure of **1** determined at 150K is shown in Fig.4.1, and a detailed view of the tetranuclear core in Fig.4.2. The structure is remarkable in that it contains three different types of azide; terminal, μ_2-1,1 bridging, μ_2-1,3 bridging. In addition, one bridging azide acts as both a μ_2-1,1 and μ_2-1,3 bridge simultaneously, in the formation of a one dimensional chain. Each tetranuclear

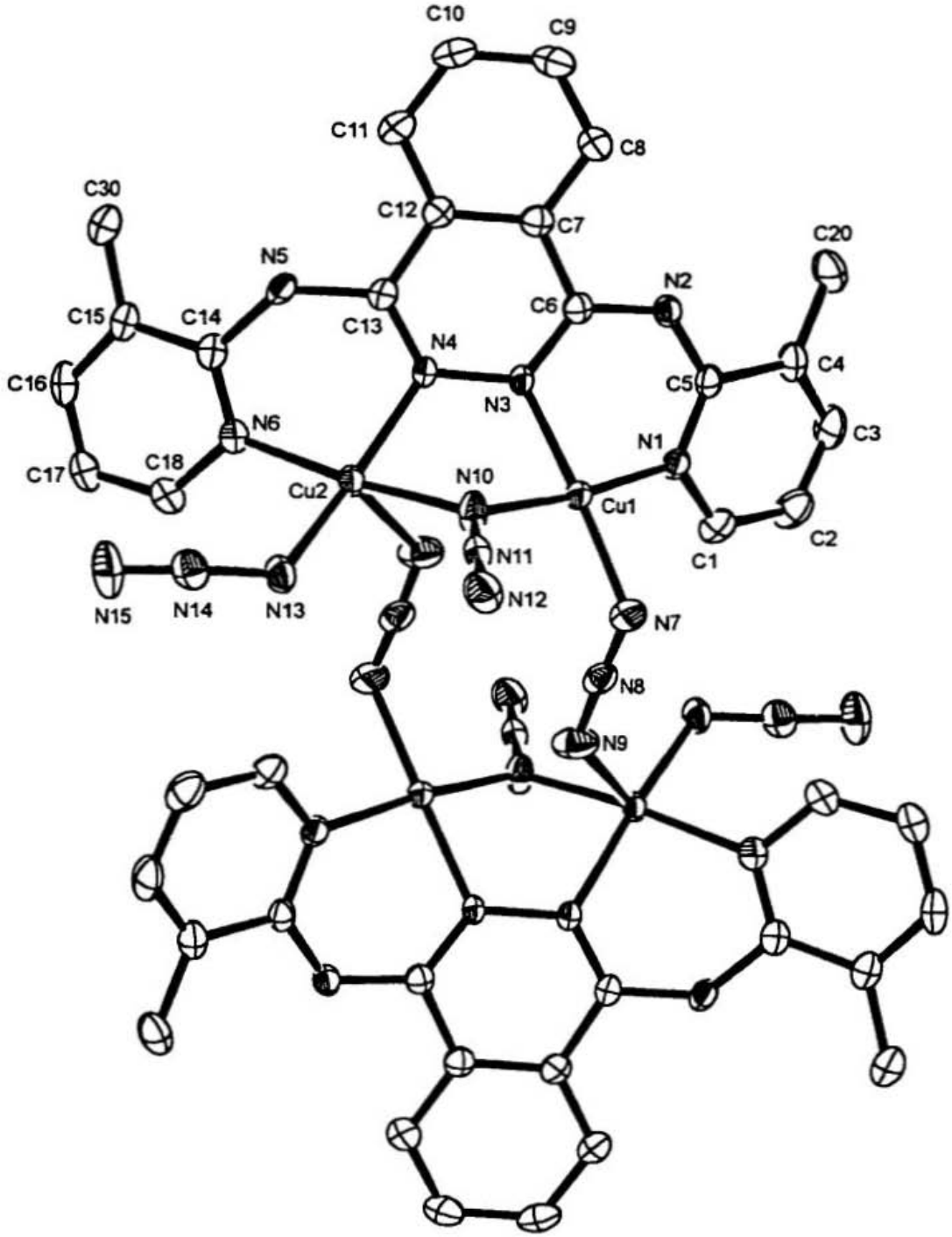

Fig. 4.1 Structural Representation of $[Cu_4(PAP3Me\text{-}H)_2(N_3)_6]$ (1) with Hydrogen Atoms Omitted (50% Probability Ellipsoids).

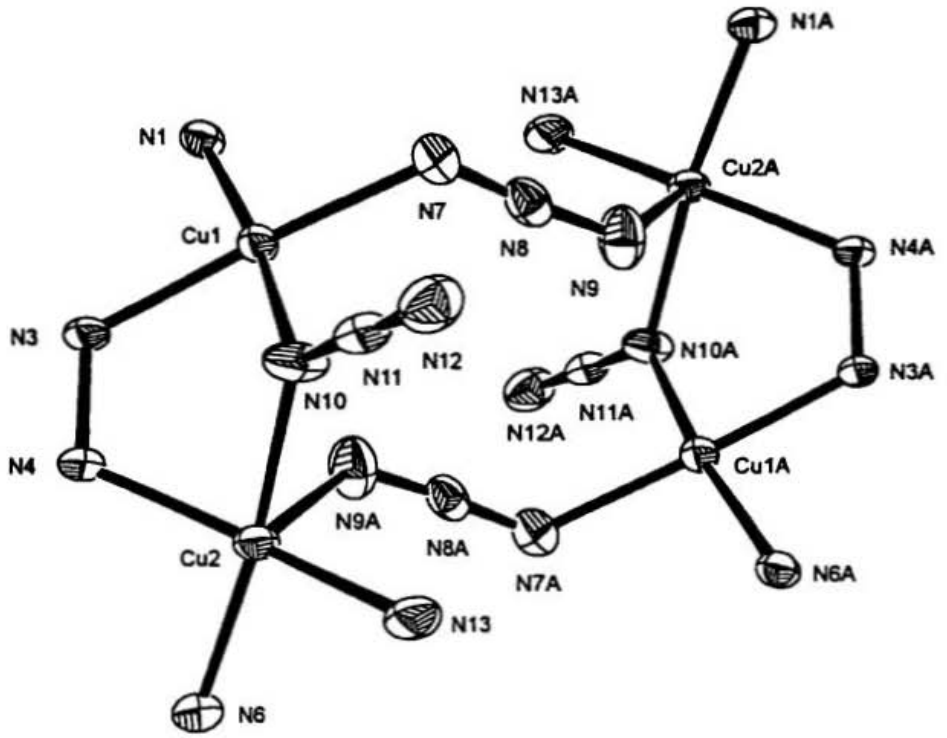

Fig. 4.2 Structural Representation of $[Cu_4(PAP3Me\text{-}H)_2(N_3)_6]$ (1): Detailed View of the Tetranuclear Core.

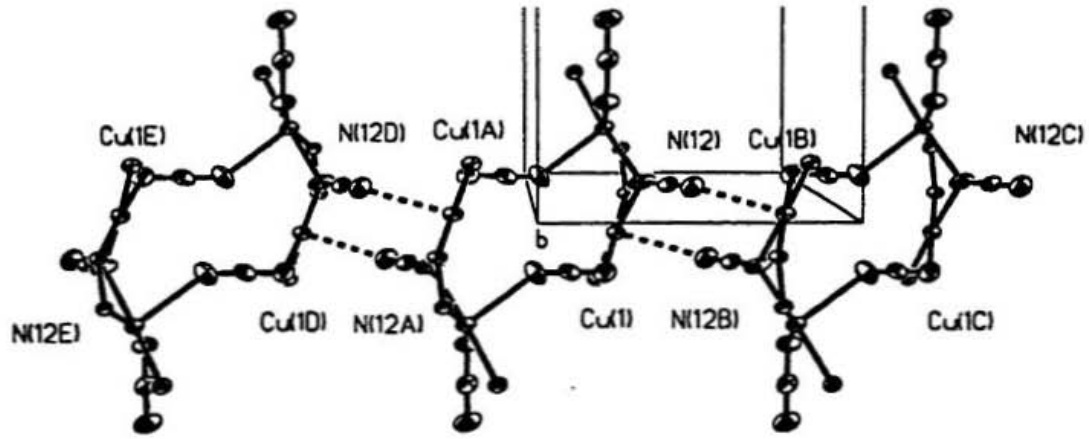

Fig. 4.3 Structural Representation of $[Cu_4(PAP3Me\text{-}H)_2(N_3)_6]$ (1): Infinite 1-Dimensional Chain Formed Along *a* by the Tetranuclear Cores.

Table 4.1(a) Selected Bond Distances (Å) and Angles (°) for $[Cu_4(PAP3Me\text{-}H)_2(N_3)_6]$ (1) at Four Temperatures (50K, 90K, 150K, 290K).

	50K	90K	150K	290K
Cu(1)-N(3)	1.969(3)	1.961(2)	1.958(2)	1.959(3)
Cu(1)-N(1)	1.981(3)	1.979(2)	1.976(2)	1.980(3)
Cu(1)-N(7)	1.984(3)	1.985(2)	1.983(2)	1.980(3)
Cu(1)-N(10)	1.990(3)	1.992(2)	1.987(2)	1.984(3)
Cu(1)-N(12B)	2.584(3)	2.597(3)	2.623(2)	2.717(4)
Cu(2)-N(13)	1.963(3)	1.965(2)	1.960(2)	1.959(3)
Cu(2)-N(10)	1.967(3)	1.966(2)	1.964(2)	1.963(3)
Cu(2)-N(6)	1.977(3)	1.971(2)	1.969(2)	1.973(3)
Cu(2)-N(4)	2.024(3)	2.019(2)	2.015(2)	2.017(3)
Cu(2)-N(9A)	2.349(3)	2.352(2)	2.359(2)	2.403(3)
Cu(1)-Cu(2)	3.185(2)	3.185(2)	3.1807(4)	3.185(2)
N(3)-N(4)	1.384(4)	1.391(3)	1.391(2)	1.394(3)
N(3)-Cu(1)-N(1)	88.37(11)	88.29(8)	88.23(7)	88.11(10)
N(3)-Cu(1)-N(7)	176.80(12)	176.93(8)	177.27(8)	177.62(12)
N(1)-Cu(1)-N(7)	94.65(12)	94.59(8)	94.40(8)	94.25(12)
N(3)-Cu(1)-N(10)	85.33(11)	85.33(8)	85.64(8)	85.81(12)
N(1)-Cu(1)-N(10)	173.11(12)	172.93(9)	173.17(8)	173.06(13)
N(7)-Cu(1)-N(10)	91.71(12)	91.85(9)	91.78(9)	91.85(13)
N(3)-Cu(1)-N(12B)	96.23(10)	96.30(8)	96.35(7)	96.90(11)
N(1)-Cu(1)-N(12B)	96.84(11)	96.78(9)	97.28(7)	98.41(11)

Table 4.1(b) Selected Angles (°) for $[Cu_4(PAP3Me\text{-}H)_2(N_3)_6]$ (1) at Four Temperatures (50K, 90K, 150K, 290K).

	50K	90K	150K	290K
N(7)-Cu(1)-N(12B)	84.49(11)	84.40(7)	84.41(8)	83.06(13)
N(10)-Cu(1)-N(12B)	81.13(12)	80.93(10)	80.44(8)	79.05(12)
N(13)-Cu(2)-N(10)	89.57(12)	89.71(8)	89.73(8)	89.99(12)
N(13)-Cu(2)-N(6)	95.44(12)	95.25(8)	95.18(8)	95.04(12)
N(10)-Cu(2)-N(6)	173.28(12)	173.26(9)	173.56(8)	174.11(12)
N(13)-Cu(2)-N(4)	164.85(12)	164.68(8)	164.58(8)	164.17(13)
N(10)-Cu(2)-N(4)	84.84(11)	84.88(8)	84.93(8)	85.26(11)
N(6)-Cu(2)-N(4)	89.20(11)	89.17(8)	89.27(7)	89.08(10)
N(13)-Cu(2)-N(9A)	105.21(12)	105.44(8)	105.68(8)	106.72(13)
N(10)-Cu(2)-N(9A)	85.57(13)	85.65(9)	85.45(9)	84.88(13)
N(6)-Cu(2)-N(9A)	97.38(12)	97.38(8)	97.21(8)	96.58(12)
N(4)-Cu(2)-N(9A)	88.42(11)	88.46(7)	88.34(7)	87.92(11)
Cu(2)-N(10)-Cu(1)	107.23(13)	107.16(10)	107.22(10)	107.60(14)
N(11)-N(10)-Cu(2)	124.4(2)	124.5(2)	124.5(2)	124.1(2)
N(11)-N(10)-Cu(1)	126.5(2)	126.5(2)	126.9(2)	127.4(2)
N(3)-N(4)-Cu(2)	116.2(2)	116.15(13)	116.44(13)	116.3(2)
N(4)-N(3)-Cu(1)	117.4(2)	117.42(13)	117.08(13)	117.2(2)
N(7)-N(8)-N(9)	176.7(3)	176.2(2)	176.2(2)	176.2(4)
N(10)-N(11)-N(12)	179.5(3)	179.5(3)	179.2(2)	179.1(4)
Cu(1)-N(12B)-N(11B)	128.6(3)	128.9(3)	130.0(2)	132.7(3)
Cu(2)-N(9A)-N(8A)	129.2(2)	128.8(2)	128.2(2)	126.2(3)

Table 4.2 Geometrical Data for $[Cu_4(PAP3Me\text{-}H)_2(N_3)_6]$ (1) at Four Temperatures (50K, 90K, 150K, 290K).

	50K	90K	150K	290K
Pyridine-Phthalazine Dihedral Angles	33.20(16)° 27.12(17)°	33.18(11)° 27.12(11)°	33.28(11)° 27.27(11)°	33.09(16)° 27.19(15)°
Angle Between Cu(II) Least Square Planes	82.17(14)°	82.08(8)°	82.25(8)°	83.57(15)°
μ_2-1,1 Azide 'Envelope' Fold	58.39(19)°	58.42(13)°	58.01(13)°	57.5(2)°
Sum of Angles Around N(10) (μ_2-1,1 Bridge)	358.1°	358.2°	358.6°	359.1°
Cu(1) Displacement	0.709(2) Å	0.704(2) Å	0.701(2) Å	0.694(2) Å
Cu(2) Displacement	0.156(1) Å	0.158(1) Å	0.156(1) Å	0.152(1) Å

unit is made up of two binuclear units linked via two μ_2-1,3 azide bridges through equatorial (Cu(1)-N(7) 1.958(2)Å) and axial (Cu(2A)-N(9) 2.359(2)Å) contacts. Each binuclear unit consists of a PAP3Me ligand, deprotonated at N(2) by the action of the weakly basic CH_3COO^- ion, which coordinates two Cu(II) centres bridged equatorially by the phthalazine diazine (N_2) moiety (Cu(1)-N(3) 1.958(2)Å, Cu(2)-N(4) 2.015(2)Å) and a μ_2-1,1 azide (Cu(1)-N(10) 1.987(2)Å, Cu(2)-N(10) 1.964(2)Å). The coordination about Cu(1) is completed by an

equatorial pyridine nitrogen (Cu(1)-N(1) 1.976(2)Å) from PAP3Me, and about Cu(2) by an equatorial pyridine nitrogen (Cu(2)-N(6) 1.969(2)Å) and a terminal azide (Cu(2)-N(13) 1.960(2)Å). This gives a nominally four coordinate geometry around Cu(1) and five coordinate around Cu(2) including the long axial contact from the μ_2-1,3 azide bridge. However, the tetranuclear clusters form chains along the ***a*** axis through short intermolecular contacts between Cu(1) and N(12) (2.623(2)Å) as shown in Fig.4.3, giving five-coordination about Cu(1) as well. The two intramolecular Cu(II) centres are separated by 3.1807(4)Å, and the μ_2-1,1 azide bridge angle is 107.22(10)°. The sum of the angles around N(10) is 358.6°, indicating that there is no significant pyramidal distortion at the μ_2-1,1 bridge. However, the μ_2-1,1 azide does not lie in the same plane as the Cu(II)-diazine moiety, such that the angle between the planes defined by Cu(1)-N(3)-N(4)-Cu(2) and Cu(1)-N(10)-Cu(2) is 58.01(13)°. The ligand PAP3Me is not planar, showing a pronounced *syn* twist, with dihedral angles between the pyridine (defined by N(1) and N(6)) mean planes and phthalazine mean plane of 27.27(11)° and 33.28(11)°, respectively. The Cu(II) centres are displaced from their N_4 mean equatorial donor planes by 0.701(2)Å (Cu(1)) and 0.156(1)Å (Cu(2)) towards N(12A) and N(9), respectively, and there is a dihedral angle of 82.25(8)° between these mean equatorial planes.

The structure of (1) was also determined at three other temperatures (50K, 90K, 290K) to identify any significant structural changes in the tetranuclear

core at different temperatures, which in turn could effect the magnetic coupling between the Cu(II) centres. Bond lengths and angles relevant to the Cu(II) coordination sphere are given in Table 4.1 and other relevant geometrical data are given in Table 4.2, for all four temperatures. The data show that there is very little variation in the structural parameters between 50K and 290K. The greatest differences are found for the μ_2-1,3 azide bridge angles and Cu-N_{azide} distances, and for the 1-dimensional chain distances and angles. For example, the bond distance Cu(1)-N(12B) ranges from 2.584(3)Å at 50K to 2.717(4)Å at 290K, while the Cu(II)-azide angle Cu(1)-N(12B)-N(11B) ranges from 128.6(3)° to 132.7(3)° over the same range. This is most likely due to the decrease in the unit cell dimensions as the temperature decreases (see Appendix B), forcing closer packing of the unit cell contents, and consequently causing a variation in the intermolecular contacts. These changes, however, are inconsequential with respect to the magnetic coupling, since these bridges do not link magnetic orbitals on the Cu(II) centres.

$[Cu_4(PAP3Me)_2(N_3)_4(NO_3)_2(H_2O)_2](NO_3)_2(H_2O)_{0.77}$ (2)

The structure of the tetranuclear cation in **2** is shown in Fig.4.4, while a detailed view of the tetranuclear core is shown in Fig.4.5. Bond distances and angles relevant to the Cu(II) coordination spheres are given in Table 4.3. One lattice nitrate was found to be disordered, and after fixing the occupancies of the

nitrate images, the geometrical and thermal parameters of the group were fixed for the final round of least squares refinement. A partially occupied lattice water was also optimised and fixed in the same manner. The tetranuclear structure is very similar to that in **1**, with two binuclear units linked via μ_2-1,3 azide bridges through equatorial (Cu(2)-N(10) 1.96(1)Å) and axial (Cu(1A)-N(12) 2.42(1)Å) contacts. The binuclear structure is also similar, with two Cu(II) centres bridged equatorially by the PAP3Me diazine moiety (Cu(1)-N(3) 2.009(9)Å, Cu(2)-N(4) 1.97(1)Å) and a μ_2-1,1 azide (Cu(1)-N(7) 1.95(1)Å, Cu(2)-N(7) 1.93(1)Å). The

Table 4.3 Selected Bond Distances (Å) and Angles (°) for $[Cu_4(PAP3Me)_2(N_3)_4(NO_3)_2(H_2O)_2](NO_3)_2(H_2O)_{0.77}$ (2).

Cu(1)-O(1)	1.981(9)	Cu(2)-N(4)	1.97(1)
Cu(1)-N(1)	1.96(1)	Cu(2)-N(6)	1.99(1)
Cu(1)-N(3)	2.009(9)	Cu(2)-N(7)	1.93(1)
Cu(1)-N(7)	1.95(1)	Cu(2)-N(10)	1.96(1)
Cu(1)-N(12A)	2.42(1)	Cu(2)-O(4)	2.563(2)
Cu(1)-Cu(2)	3.163(6)	N(3)-N(4)	1.35(1)
Cu(1)-N(7)-Cu(2)	109.4(5)	N(6)-Cu(2)-N(7)	171.7(4)
O(1)-Cu(1)-N(1)	93.1(4)	N(6)-Cu(2)-N(10)	95.0(5)
O(1)-Cu(1)-N(3)	171.7(4)	N(6)-Cu(2)-O(4)	88.0(4)
O(1)-Cu(1)-N(7)	94.2(5)	N(7)-Cu(2)-N(10)	93.2(4)
O(1)-Cu(1)-N(12A)	91.8(4)	N(7)-Cu(2)-O(4)	95.4(3)
N(1)-Cu(1)-N(7)	175.0(5)	N(10)-Cu(2)-O(4)	87.6(4)
N(1)-Cu(1)-N(3)	90.8(5)	Cu(1)-N(7)-N(8)	124(1)
N(1)-Cu(1)-N(12A)	90.1(5)	Cu(2)-N(7)-N(8)	120(1)
N(3)-Cu(1)-N(7)	93.3(5)	N(7)-N(8)-N(9)	177(2)
N(3)-Cu(1)-N(12A)	88.7(4)	Cu(1)-N(12A)-N(11A)	110.2(1)
N(7)-Cu(1)-N(12A)	85.0(5)	Cu(2)-N(10)-N(11)	122(1)
N(4)-Cu(2)-N(6)	88.0(5)	N(10)-N(11)-N(12)	173(1)
N(4)-Cu(2)-N(7)	83.8(4)	Cu(1)-N(3)-N(4)	115.6(8)
N(4)-Cu(2)-N(10)	172.4(5)	Cu(2)-N(4)-N(3)	118.1(8)
N(4)-Cu(2)-O(4)	99.6(3)		

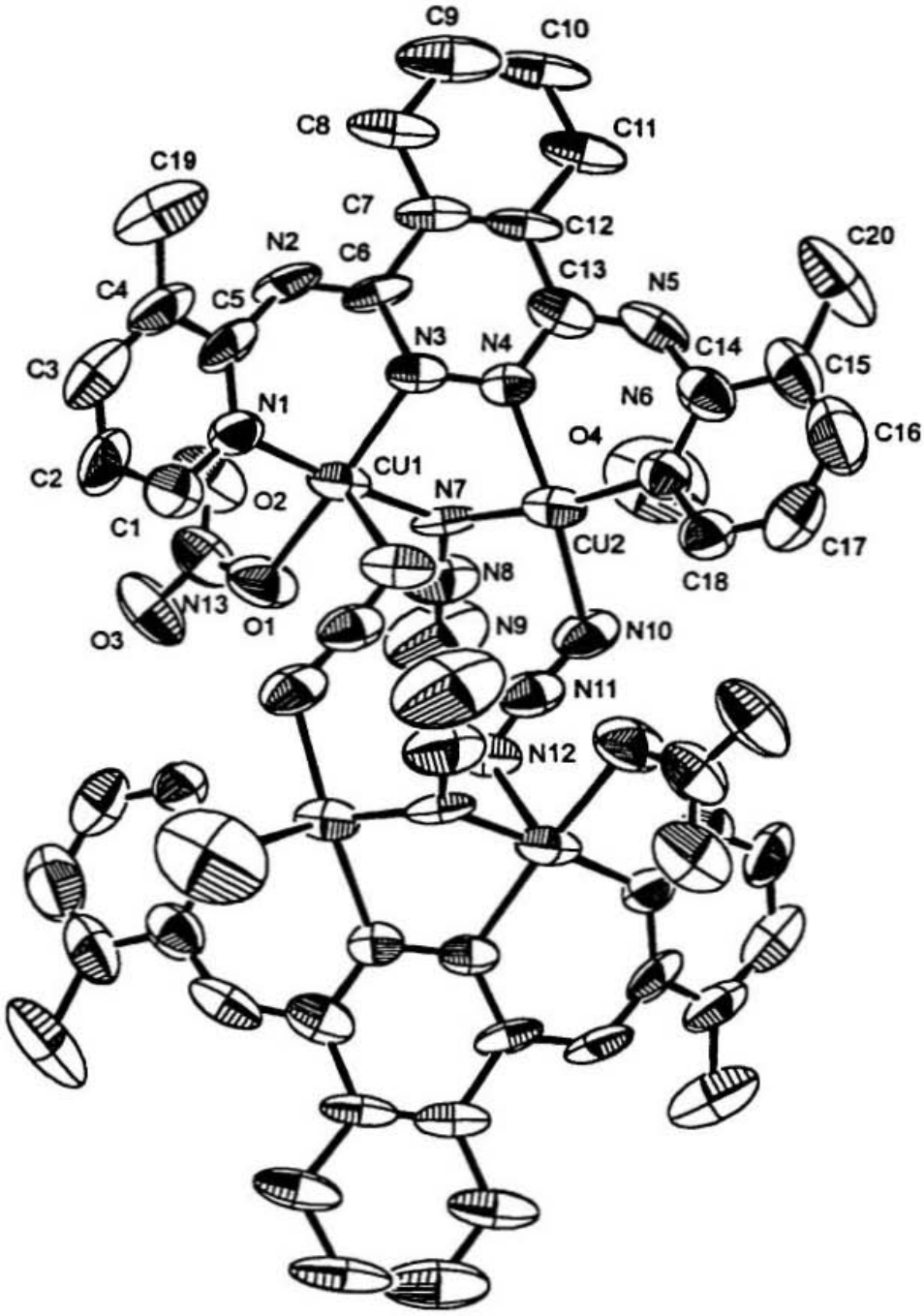

Fig. 4.4 Structural Representation of $[Cu_4(PAP3Me)_2(N_3)_4(NO_3)_2(H_2O)_2](NO_3)_2(H_2O)_{0.77}$ (2) with Hydrogen Atoms, Nitrate Counter Ions and Lattice Solvent Omitted (50% Probability Ellipsoids).

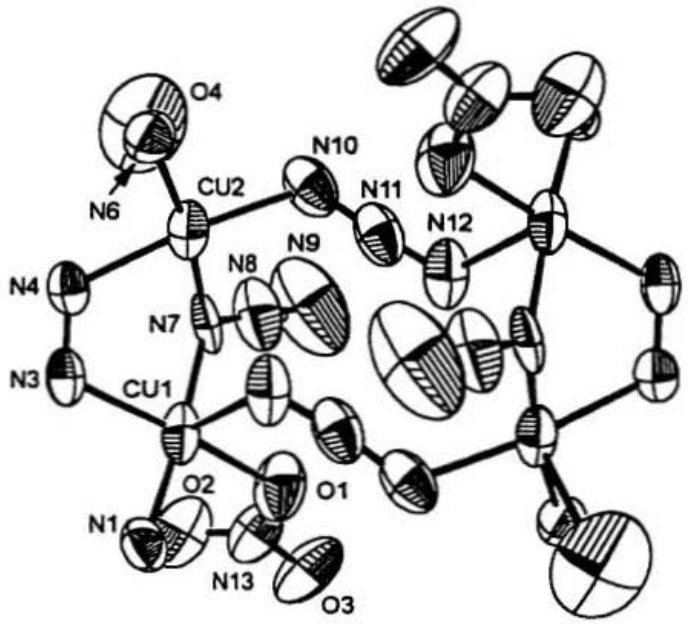

Fig. 4.5 Structural Representation of $[Cu_4(PAP3Me)_2(N_3)_4(NO_3)_2(H_2O)_2](NO_3)_2(H_2O)_{0.77}$ (2): Detailed View of the Tetranuclear Core.

coordination sphere about Cu(1) is completed by an equatorial pyridine nitrogen (Cu(1)-N(1) 1.96(1)Å) and an equatorial monodentate nitrate (Cu(1)-O(1) 1.981(9)Å), while an equatorial pyridine nitrogen (Cu(2)-N(6) 1.99(1)Å) and a long axial water contact (Cu(2)-O(4) 2.563(2)Å) complete the coordination around Cu(2). This gives two five-coordinate Cu(II) centres with different donor sets; for Cu(1), the equatorial (axial) donor set is $N_3O(N)$, while for Cu(2) it is $N_4(O)$. The separation between the two Cu(II) centres is 3.163(6)Å, and the μ_2-1,1 bridge angle is 109.4(5)°. The fold angle of the μ_2-1,1 azide out of the Cu(II)-diazine plane, as defined for **1**, is 57.7(7)°. Again, the ligand PAP3Me shows a *syn* twist of the pyridine mean planes (defined by N(1) and N(6)) of 37.5(6)° and 38.9(7)°, respectively. The Cu(II) centres are displaced from their

N_3O (Cu(1)) and N_4 (Cu(2)) mean equatorial donor planes by 0.056(2)Å (Cu(1)) and 0.070(2)Å (Cu(2)) towards N(12) and O(4), respectively, and there is a dihedral angle of 53.1(5)° between the Cu(II) least square planes.

$[Cu_2(PAP3Me)(N_3)_3(CH_3OH)](ClO_4)(H_2O)$ (3)

The structure of the binuclear cation in **3** is shown in Fig.4.6, and bond distances and angles relevant to the Cu(II) coordination spheres are given in Table 4.4. In addition to the binuclear moiety and perchlorate counter ion, another poorly defined fragment is found in the lattice. This is apparently lattice solvent as suggested by the elemental analysis. However, attempts to refine this fragment as lattice solvent were unsuccessful, and the peaks were defined as half occupancy C, N, and S. This choice has no chemical significance, and was used only because these gave the best refinement of the parameters for the rest of the structure. The geometrical and thermal parameters of these sites were then fixed for the final round of least squares refinement to ensure that the solution converged and that the structure refined to reasonably low estimated standard deviations, and reasonably low R_1 and wR_2.

Unlike the previously discussed structures **1** and **2** , **3** does not form a tetranuclear structure, but instead occurs as the isolated binuclear complex. The two essentially square pyramidal Cu(II) centres are linked by three different bridges. They are bridged equatorially by the ligand diazine moiety (Cu(1)-N(3)

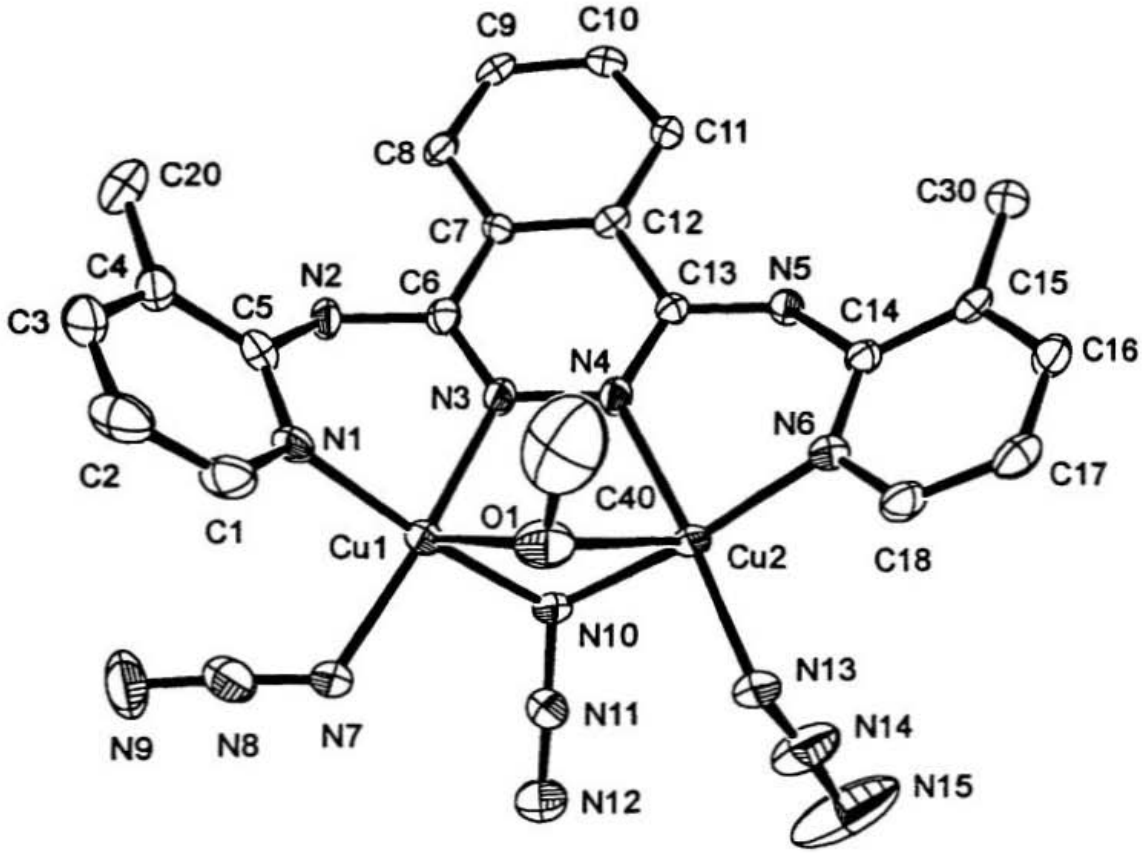

Fig. 4.6 Structural Representation of $[Cu_2(PAP3Me)(N_3)_3(CH_3OH)](ClO_4)(H_2O)$ (3) with Hydrogen Atoms, Perchlorate Counter Ion and Lattice Fragment Omitted (50% Probability Ellipsoids).

2.009(5)Å, Cu(2)-N(4) 2.018(5)Å) and a μ_2-1,1 azide (Cu(1)-N(10) 2.004(5)Å, Cu(2)-N(10) 1.990(5)Å), while a methanol molecule forms a weak axial bridge with long contacts (Cu(1)-O(1) 2.407(5)Å, Cu(2)-O(1) 2.689(6)Å). The coordination sphere around both metal centres is completed by an equatorial pyridine nitrogen (Cu(1)-N(1) 1.996(6)Å, Cu(2)-N(6) 2.003(5)Å) and an equatorial, terminal azide (Cu(1)-N(7) 1.972(6)Å, Cu(2)-N(13) 1.966(6)Å). The

Table 4.4 Selected Bond Distances (Å) and Angles (°) for $[Cu_2(PAP3Me)(N_3)_3(CH_3OH)](ClO_4)(H_2O)$ (3).

Cu(1)-N(7)	1.972(6)	Cu(2)-N(13)	1.966(6)
Cu(1)-N(1)	1.996(6)	Cu(2)-N(10)	1.990(5)
Cu(1)-N(10)	2.004(5)	Cu(2)-N(6)	2.003(5)
Cu(1)-N(3)	2.009(5)	Cu(2)-N(4)	2.018(5)
Cu(1)-O(1)	2.407(5)	Cu(2)-O(1)	2.689(6)
Cu(1)-Cu(2)	3.140(2)	N(3)-N(4)	1.380(7)
Cu(1)-N(10)-Cu(2)	103.6(2)	N(10)-Cu(2)-N(6)	172.7(2)
N(7)-Cu(1)-N(1)	93.9(2)	N(13)-Cu(2)-N(4)	174.4(2)
N(7)-Cu(1)-N(10)	93.5(2)	N(10)-Cu(2)-N(4)	86.1(2)
N(1)-Cu(1)-N(10)	171.8(2)	N(6)-Cu(2)-N(4)	86.7(2)
N(7)-Cu(1)-N(3)	167.4(2)	N(4)-Cu(2)-O(4)	83.3(2)
N(1)-Cu(1)-N(3)	87.2(2)	N(6)-Cu(2)-O(1)	100.7(2)
N(10)-Cu(1)-N(3)	84.7(2)	N(13)-Cu(2)-O(1)	91.2(2)
N(7)-Cu(1)-O(1)	103.7(2)	N(10)-Cu(2)-O(1)	78.7(2)
N(1)-Cu(1)-O(1)	95.8(2)	Cu(1)-N(10)-N(11)	118.0(4)
N(1)-Cu(1)-O(1)	85.8(2)	Cu(2)-N(10)-N(11)	120.7(4)
N(3)-Cu(1)-O(1)	88.7(2)	N(10)-N(11)-N(12)	179.2(7)
N(13)-Cu(2)-N(10)	92.7(2)	Cu(1)-N(3)-N(4)	116.3(4)
N(13)-Cu(2)-N(6)	94.5(2)	Cu(2)-N(4)-N(3)	115.3(4)

separation between the two Cu(II) centres is 3.140(2)Å, while the angle at the μ_2-1,1 azide bridge is 103.6(2)°. The fold angle of the μ_2-1,1 azide out of the Cu(II)-diazine plane is 61.7(3)°. The PAP3Me ligand exhibits a *syn* twist with angles of 44.6(3)° and 23.2(3)° between the pyridine rings, as defined by N(1) and N(6) respectively, and phthalazine mean planes. The Cu(II) centres are also slightly displaced from their N_4 mean equatorial planes towards O(1) by 0.137(4)Å (Cu(1)) and 0.048(3)Å (Cu(2)), and the dihedral angle between the mean equatorial planes is 56.5(2)°.

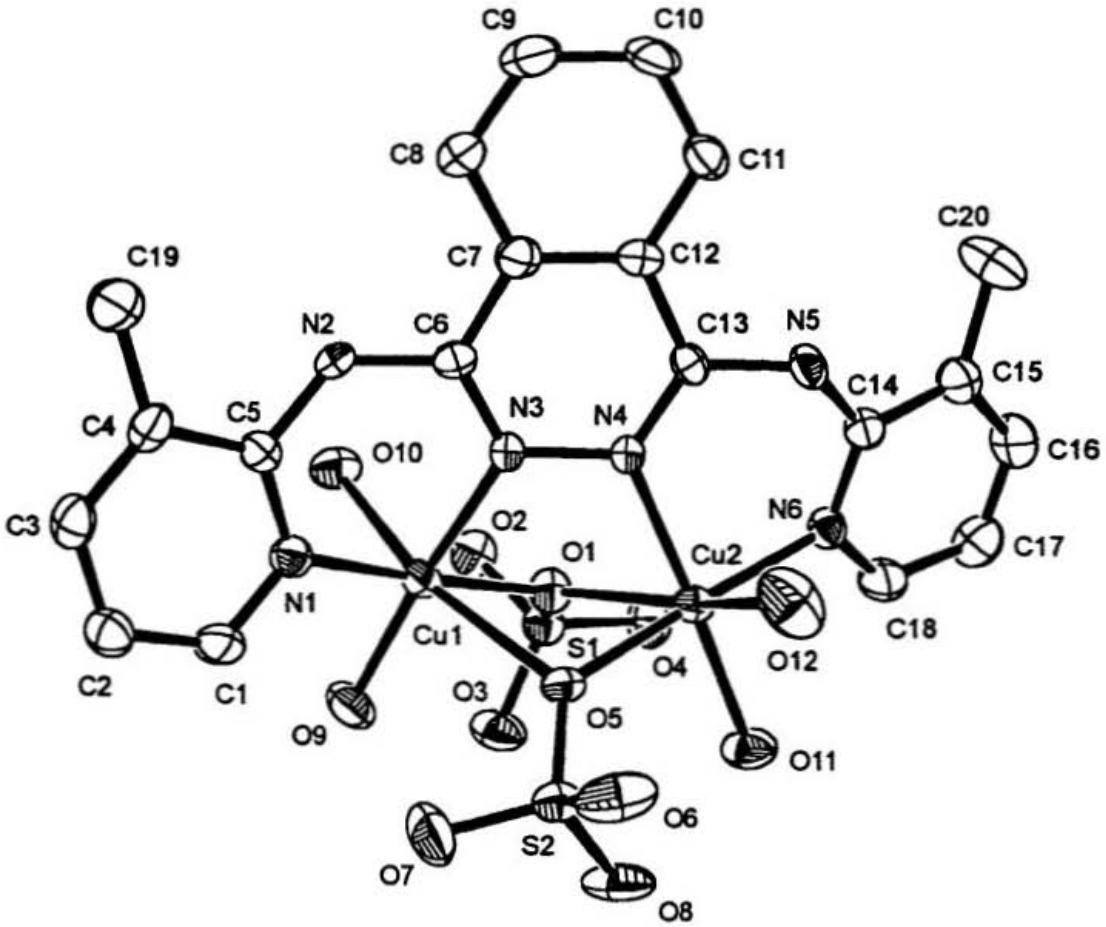

Fig. 4.7 Structural Representation of $[Cu_2(PAP3Me)(SO_4)_2(H_2O)_4](H_2O)_{1.5}$ (6) with Hydrogen Atoms and Lattice Solvent Omitted (50% Probability Ellipsoids).

$[Cu_2(PAP3Me)(SO_4)_2(H_2O)_4](H_2O)_{1.5}$ (6)

The structure of a representative binuclear unit of **6** is shown in Fig.4.7. The structure is unusual in that there are three such binuclear units in each asymmetric unit, which are chemically identical but crystallographically independent. One of the binuclear units (residue #3) contains a disordered sulfate bridge in which the non-coordinated oxygen atoms could not be modelled

Table 4.6 Geometrical Data for $[Cu_2(PAP3Me)(SO_4)_2(H_2O)_4](H_2O)_{1.5}$ (6) for all Three Binuclear Centres in Asymmetic Unit.

	Residue #1	Residue #2	Residue #3
Pyridine-Phthalazine Dihedral Angles	32.58(18)° 30.84(18)°	30.04(18)° 35.30(18)°	32.12(18)° 31.30(18)°
Angle Between Cu(II) Least Squares Planes	38.73(15)°	36.62(15)°	36.32(15)°
Cu(1/3/5) Displacement	0.019(1) Å	0.095(1) Å	0.026(1) Å
Cu(2/4/6) Displacement	0.019(1) Å	0.034(1) Å	-0.051(1) Å

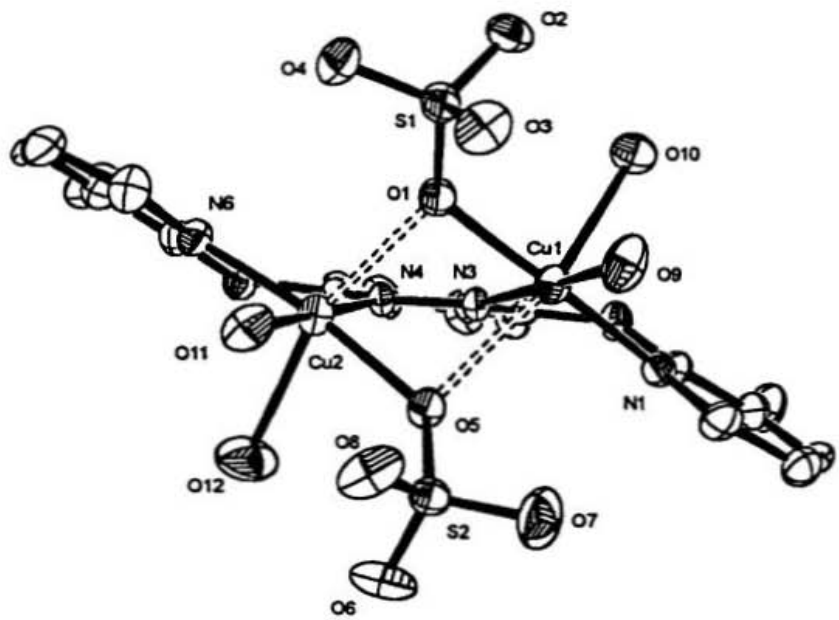

Fig. 4.8 Structural Representation of $[Cu_2(PAP3Me)(SO_4)_2(H_2O)_4](H_2O)_{1.5}$ (6): View of Binuclear Centre Showing Axial (==) / Equitorial (—) Sulfate Bridges.

Table 4.5(a) Selected Bond Distances (Å) and Angles (°) for $[Cu_2(PAP3Me)(SO_4)_2(H_2O)_4](H_2O)_{1.5}$ (6): Binuclear Residue #1.

Cu(1)-O(1)	2.013(3)	O(5)-Cu(1)-N(3)	79.8(1)
Cu(1)-O(5)	2.460(3)	O(9)-Cu(1)-O(10)	89.7(1)
Cu(1)-O(9)	1.989(3)	O(9)-Cu(1)-N(1)	94.4(1)
Cu(1)-O(10)	2.299(3)	O(9)-Cu(1)-N(3)	175.1(1)
Cu(1)-N(1)	2.001(4)	O(10)-Cu(1)-N(1)	90.5(1)
Cu(1)-N(3)	2.008(4)	O(10)-Cu(1)-N(3)	93.1(1)
Cu(2)-O(1)	2.361(3)	N(1)-Cu(1)-N(3)	88.9(2)
Cu(2)-O(5)	2.064(3)	O(1)-Cu(2)-O(5)	80.6(1)
Cu(2)-O(12)	2.361(3)	O(1)-Cu(2)-O(11)	97.7(1)
Cu(2)-O(11)	1.949(3)	O(1)-Cu(2)-O(12)	157.9(1)
Cu(2)-N(4)	2.012(4)	O(1)-Cu(2)-N(4)	78.8(1)
Cu(2)-N(6)	2.028(4)	O(1)-Cu(2)-N(6)	104.5(1)
Cu(1)-Cu(2)	3.222(2)	O(5)-Cu(2)-O(11)	87.8(1)
N(3)-N(4)	1.381(5)	O(5)-Cu(2)-O(12)	82.2(1)
		O(5)-Cu(2)-N(4)	90.3(1)
Cu(1)-O(5)-Cu(2)	90.4(1)	O(5)-Cu(2)-N(6)	174.8(1)
Cu(1)-O(1)-Cu(2)	94.5(1)	O(11)-Cu(2)-O(13)	95.4(1)
O(1)-Cu(1)-O(5)	79.2(1)	O(11)-Cu(2)-N(4)	176.2(1)
O(1)-Cu(1)-O(9)	89.1(1)	O(11)-Cu(2)-N(6)	92.4(1)
O(1)-Cu(1)-O(10)	89.0(1)	O(12)-Cu(2)-N(4)	87.5(1)
O(1)-Cu(1)-N(1)	176.5(1)	O(12)-Cu(2)-N(6)	92.6(2)
O(1)-Cu(1)-N(3)	87.7(1)	N(4)-Cu(2)-N(6)	89.2(2)
O(5)-Cu(1)-O(9)	96.8(1)	Cu(1)-N(3)-N(4)	116.9(3)
O(5)-Cu(1)-O(10)	166.4(1)	Cu(1)-N(4)-N(3)	115.9(3)
O(5)-Cu(1)-N(1)	100.9(1)		

as single sites due to rotation of the group around the S(5)-μ_2O(25) bond. The non-coordinated oxygen atoms of this group were refined as two half occupancy sites each to account for this. In addition, not all of the hydrogen atoms of the water molecules were found.

The occurrence of three crystallographically independent binuclear units in the asymmetric unit is unusual, especially since the complex crystallises in the

Table 4.5(b) Selected Bond Distances (Å) and Angles (°) for $[Cu_2(PAP3Me)(SO_4)_2(H_2O)_4](H_2O)_{1.5}$ (6): Binuclear Residue #2.

Cu(3)-O(13)	2.017(3)	O(17)-Cu(3)-N(9)	77.3(1)
Cu(3)-O(17)	2.543(3)	O(21)-Cu(3)-O(22)	99.5(1)
Cu(3)-O(21)	1.982(3)	O(21)-Cu(3)-N(7)	92.4(2)
Cu(3)-O(22)	2.271(4)	O(21)-Cu(3)-N(9)	165.3(1)
Cu(3)-N(7)	2.004(4)	O(22)-Cu(3)-N(7)	89.4(1)
Cu(3)-N(9)	1.990(4)	O(22)-Cu(3)-N(9)	95.0(1)
Cu(4)-O(13)	2.425(3)	N(7)-Cu(3)-N(9)	89.7(2)
Cu(4)-O(17)	2.025(3)	O(13)-Cu(4)-O(17)	83.7(1)
Cu(4)-O(24)	2.436(4)	O(13)-Cu(4)-O(23)	99.6(1)
Cu(4)-O(23)	1.944(3)	O(13)-Cu(4)-O(24)	160.8(1)
Cu(4)-N(10)	1.997(4)	O(13)-Cu(4)-N(10)	79.5(1)
Cu(4)-N(12)	2.002(4)	O(13)-Cu(4)-N(12)	100.4(1)
Cu(3)-Cu(4)	3.211(2)	O(17)-Cu(4)-O(23)	90.6(1)
N(9)-N(10)	1.372(5)	O(17)-Cu(4)-O(24)	81.6(1)
		O(17)-Cu(4)-N(10)	89.3(1)
Cu(3)-O(13)-Cu(4)	92.1(1)	O(17)-Cu(4)-N(12)	174.9(1)
Cu(3)-O(17)-Cu(4)	88.6(1)	O(23)-Cu(4)-O(24)	92.9(1)
O(13)-Cu(3)-O(17)	89.9(1)	O(23)-Cu(4)-N(10)	179.2(1)
O(13)-Cu(3)-O(21)	88.2(1)	O(23)-Cu(4)-N(12)	91.5(1)
O(13)-Cu(3)-O(22)	88.4(1)	O(24)-Cu(4)-N(10)	87.9(1)
O(13)-Cu(3)-N(7)	177.7(1)	O(24)-Cu(4)-N(12)	93.7(1)
O(13)-Cu(3)-N(9)	90.3(1)	N(10)-Cu(4)-N(12)	88.6(2)
O(17)-Cu(3)-O(21)	88.0(2)	Cu(3)-N(9)-N(10)	116.5(3)
O(17)-Cu(3)-O(22)	166.7(1)	Cu(4)-N(10)-N(9)	116.6(3)
O(17)-Cu(3)-N(7)	101.3(1)		

relatively high symmetry (for a coordination complex at least) space group $P2_1/n$. One possible explanation for this lies in the extensive hydrogen bonding network which is observed (See Appendix C), especially that connecting the lattice solvent to the binuclear units. This could force small deviations in the structural parameters of the individual binuclear units to accommodate the combination of this network and the crystal packing. Since the three binuclear residues of the

Table 4.5(c) Selected Bond Distances (Å) and Angles (°) for $[Cu_2(PAP3Me)(SO_4)_2(H_2O)_4](H_2O)_{1.5}$ (6): Binuclear Residue #3.

Cu(5)-O(25)	1.999(3)	O(32)-Cu(5)-N(15)	78.4(1)
Cu(5)-O(32)	2.534(3)	O(36)-Cu(5)-O(37)	90.5(1)
Cu(5)-O(36)	1.963(3)	O(36)-Cu(5)-N(13)	93.1(2)
Cu(5)-O(37)	2.335(4)	O(36)-Cu(5)-N(15)	176.8(1)
Cu(5)-N(13)	1.993(4)	O(37)-Cu(5)-N(13)	94.7(1)
Cu(5)-N(15)	2.004(4)	O(37)-Cu(5)-N(15)	91.9(1)
Cu(6)-O(25)	2.416(3)	N(13)-Cu(5)-N(15)	88.8(2)
Cu(6)-O(32)	2.052(3)	O(25)-Cu(6)-O(32)	81.3(1)
Cu(6)-O(38)	2.318(4)	O(25)-Cu(6)-O(38)	162.3(1)
Cu(6)-O(39)	1.988(3)	O(25)-Cu(6)-O(39)	89.4(1)
Cu(6)-N(16)	1.996(4)	O(25)-Cu(6)-N(16)	78.7(1)
Cu(6)-N(18)	1.988(3)	O(25)-Cu(6)-N(18)	104.5(1)
Cu(5)-Cu(6)	3.246(2)	O(32)-Cu(6)-O(38)	84.2(1)
N(15)-N(16)	1.381(5)	O(32)-Cu(6)-O(39)	88.1(1)
		O(32)-Cu(6)-N(16)	90.8(1)
Cu(5)-O(25)-Cu(6)	94.2(1)	O(32)-Cu(6)-N(18)	174.2(1)
Cu(5)-O(32)-Cu(6)	89.5(1)	O(38)-Cu(6)-O(39)	100.2(1)
O(25)-Cu(5)-O(32)	79.4(1)	O(38)-Cu(6)-N(16)	91.4(1)
O(25)-Cu(5)-O(36)	89.9(1)	O(38)-Cu(6)-N(18)	90.0(2)
O(25)-Cu(5)-O(37)	85.8(1)	O(39)-Cu(6)-N(16)	168.1(2)
O(25)-Cu(5)-N(13)	177.0(1)	O(39)-CU(6)-N(18)	92.4(2)
O(25)-Cu(5)-N(15)	88.3(1)	N(16)-Cu(6)-N(18)	89.9(2)
O(32)-Cu(5)-O(36)	98.7(1)	Cu(5)-N(15)-N(16)	117.7(3)
O(32)-Cu(5)-O(37)	162.4(1)	Cu(6)-N(16)-N(15)	116.1(3)
O(32)-Cu(5)-N(13)	99.6(1)		

asymmetric unit differ only slightly in bond lengths and bond angles, the general trends observed for one are relevant to the other two. The structure of just one binuclear unit (residue #1) will be discussed in detail here, and the bond distances and angles relevant to the Cu(II) coordination spheres in all three are given in Table 4.5 with other relevant geometric data for all three reported in Table 4.6. The binuclear Cu(II) moiety is triply bridged by the equatorial diazine

of the PAP3Me ligand (Cu(1)-N(3) 2.008(4)Å, Cu(2)-N(4) 2.012(4)Å) and two axial / equatorial μ_2-O sulfate bridges (Cu(1)-O(1) 2.013(3)Å, Cu(2)-O(1) 2.361(3)Å and Cu(1)-O(5) 2.460(3)Å, Cu(2)-O(5) 2.064(3)Å). The different axial / equatorial bond lengths can be easily seen in Fig. 4.8, which shows a view of **6** looking down the axis of the PAP3Me phthalazine plane. The occurrence of axial / equatorial bridges in polydentate diazine ligands is not uncommon,[27,28,89-94] but these are generally monatomic chloride or bromide bridges. Sulfate bridges, on the other hand, are relatively rare in polynuclear Cu(II) systems. They are generally bidentate, bridging via two oxygen atoms,[95-97] or tridentate via three oxygen atoms.[98-100] The μ_2-O sulfate bridging mode via a single oxygen, however, is almost unprecedented. Only one example has been reported in the literature[101] in the complex $[Cu(HL)(SO_4)]_2$ (HL = pyridine-2-carbaldehyde thiosemi-carbazone), which also contains an axial / equatorial sulfate bridge. It is interesting to note that binuclear Cu(II) complexes of the same ligand containing analogous acetate[101] and dihydrogenphosphate[102] ligands bridging via a single oxygen atom have also been reported. The coordination sphere about each Cu(II) centre in **6** is completed by an equatorial pyridine nitrogen of the PAP3Me ligand (Cu(1)-N(1) 2.001(4)Å, Cu(2)-N(6) 2.208(4)Å) and two water molecules, one of which is equatorial (Cu(1)-O(9) 1.989(3)Å, Cu(2)-O(12) 1.949(3)Å) and the other axial (Cu(1)-O(10) 2.299(3)Å, Cu(2)-O(11) 2.361(3)Å). This gives each Cu(II) centre a six coordinate, distorted octahedral coordination sphere. The

Cu-O(sulfate)-Cu bridge angles are not equal (Cu(1)-O(1)-Cu(2) 94.5(1)°, Cu(1)-O(5)-Cu(2) 90.4(1)°). The two Cu(II) metal centres are separated by 3.222(2)Å and the dihedral angle between the two N_2O_2 mean equatorial planes is 38.75(15)°. The Cu(II) centres are both displaced slightly from the N_2O_2 mean equatorial planes by 0.019(1)Å towards O(10) (Cu(1)) and O(12) (Cu(2)), respectively. The ligand PAP3Me in **6** is twisted as well, but in this case it shows a pronounced *anti* rather than *syn* twist, with angles of 32.58(18)° (N(1)) and 30.84(18)° (N(6)) between the pyridine mean planes and the phthalazine mean planes.

4.2.2 Comparison of the Cu(II) / PAP3Me μ_2-1,1 Azide Bridged Complexes

As was noted in Chapter 3, the PAP3Me ligand was chosen for this study in the hopes that the steric influence of the 3-methyl group would push the observed μ_2-1,1 azide bridge angle for the PAPR group of ligands below that already observed, so as to investigate the magnetic behaviour as the magnetic crossover angle is approached. One interesting result, however, has been that the observed angles for the PAP3Me series of Cu(II) / N_3^- complexes fall in a relatively large range, from a value typical of the Cu(II) / PAP6Me azide complexes (109.4(5)° for **2**) to a value very far below that for the Cu(II) / PAP series of complexes (103.6(2)° for **3**), while the bridge angle for **1** (107.22(10)° at 150K) is about as was expected. The reasons for this variation are not

immediately clear from the structures of the complexes. Regardless of the cause, the results allow a valuable comparison of the magnetic and spectroscopic data over a wide range of angles for a series of complexes with the same primary ligand.

In terms of the other structural parameters, the three structures reported here are similar to each other and previously reported Cu(II) / PAPR azide complexes,[38,58,59] with a few exceptions. The angles between the Cu(II) mean equatorial planes for **2** and **3** are typical, but in the case of **1** the angle is almost twice as large (82.25(8)° at 150K) as for the other two complexes. Another interesting feature is found in **3**, in which one of the pyridine-phthalazine dihedral angles is nearly twice that of the other (44.6(3)° vs 23.2(3)°). The two angles are usually similar, as for **1** and **2**, the greatest variation previously reported having been 23.1° and 33.6° for $[Cu_2(PAP)(N_3)Br_3]\cdot CH_2Cl_2$.[59] On the other hand, the three complexes reported herein show similar azide 'out of plane' fold angles, and comparable bond distances and angles. They also show decreasing Cu(II)-Cu(II) separation with decreasing μ_2-1,1 azide bridge angle, as expected.

4.3 Spectroscopy

4.3.1 Infrared and Electronic Spectra of the Cu(II) / PAP3Me Complexes

The primary means for elucidating the composition and structure of the Cu(II) / PAP3Me complexes reported herein has been a combination of infrared

and electronic spectroscopy. While X-ray crystallography is certainly the ideal and only truly unambiguous means for this determination, IR and UV/Vis spectroscopy have their own strengths. Certainly, in those situations in which it proves impossible to obtain X-ray quality crystals, one must rely on spectroscopy. However, spectroscopy has the advantage of immediate results as well. The determination of a crystal structure from start to finish can take from days to months, whereas the spectra of the same complex can be obtained as soon as a clean, dried sample is prepared, allowing rapid preliminary assignment of composition and structure.

Relevent spectroscopic data for the azide complexes **1** - **5** are given in Table 4.7, while data for the other Cu(II) / PAP3Me complexes **6** - **9** are given in Table 4.8. For the azide complexes **1** - **5**, by far the most critical feature of the infrared spectra is the antisymmetric stretch (ν_3 or ν_{as}) of the azide ligand (Fig.4.9). Ionic azides have symmetrical N-N bonds, such as for NH_4N_3,[103] in which each bond is 1.15Å in length and the antisymmetric stretching frequency

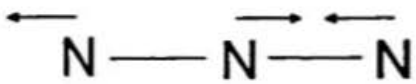

Fig. 4.9 Antisymmetric (ν_3) Stretch of the Azide Ion.

occurs at 2030 cm^{-1} . Upon coordination, the bond containing the coordinated nitrogen is weakened and lengthened, while the other N-N bond becomes stronger and shorter. For example, the structure of **1** at 150K shows a

Table 4.7 Infrared and Electronic Spectral Data for Cu(II) / PAP3Me Azide Complexes.

Complex	IR, cm^{-1}			λ_{max}, nm (ε, $M^{-1} cm^{-1}$)	
	N_3^- (ν_3 Stretch)	Pyridine Ring Breathing	Anion / Anionic Ligand	Solution	Mull
$[Cu_4(PAP3Me\text{-}H)_2(N_3)_6]$ **(1)**	2110 2049 2037	1003	-	420 (10500) 455 (7430) 600 (390)	410 [465]* 610
$[Cu_4(PAP3Me)_2(N_3)_4(NO_3)_2(H_2O)_2](NO_3)_2$ **(2)**	2097 2052	1006	1755, 1738, 1722 ($\nu_1+\nu_4$ NO_3^-)	405 (10300) 630 (270)	370 [425] 610
$[Cu_2(PAP3Me)(N_3)_3(CH_3OH)](ClO_4)(H_2O)$ **(3)**	2087 2051	1010	1085 (ν_3 ClO_4^-)	410 (11900) 610 (290)	400 590
$[Cu_2(PAP3Me)(N_3)_2Cl_2](CH_3OH)_{1.5}$ **(4)**	2082 2037	1018	284 (ν Cu-Cl)	410 (9900) 635 (370)	360 [430] 680
$[Cu_4(PAP3Me)_2(N_3)_5Br_3]$ **(5)**	2098 2060 2046	998	316 (ν Cu-Br)	410 (9400) 630 (330)	370 [430] 630

* [] indicates a shoulder.

Table 4.8 Infrared and Electronic Spectral Data for the Remaining Cu(II) / PAP3Me Complexes.

Complex	IR, cm^{-1}			λ_{max}, nm (ε, $M^{-1} cm^{-1}$)	
	Anion / Anionic Ligand	Pyridine Ring Breathing	OH^- (νOH^-)	Solution	Mull
$[Cu_2(PAP3Me)(SO_4)_2(H_2O)_4](H_2O)$ **(6)**	951, 967, 1036, 1103, 1138, 1183 (SO_4^{2-})	*	-	405 (11000) [420, (10500)] 670 (100)	370 [420]* 720
$[Cu_2(PAP3Me)Cl_4]$ **(7)**	307 (ν_t Cu-Cl) 267 (ν_b Cu-Cl)	1001	-	410 (9000) 720 (160)	420 660
$[Cu_2(PAP3Me)(OH)(NO_3)_3](H_2O)$ **(8)**	1753, 1741, [1738], 1731 ($\nu_1+\nu_4$ NO_3^-)	1007	3490	405 (8100) [420 (10500)] 690 (140)	370 [430] 630
$[Cu_2(PAP3Me)(OH)Br_3$ **(9)**	†	998	3605	395 (14900) [415 (15400)] 675 (190)	370 [440] 660

* [] indicates a shoulder.
* pyridine ring breathing band obscured by sulfate bands.
† weak spectrum. Cu-Br bands could not be unambiguously identified.

N(10)-N(11) bond length of 1.213(3)Å and a N(11)-N(12) bond length of 1.147(3)Å, with a stretching frequency of 2110 cm^{-1}. Therefore, as a general rule, as the strength of coordination increases, the frequency also increases.

Regarding the complexes of interest here, this means that the azide bands in the IR provide valuable information about its bonding mode. In general, it is observed that μ_2-1,1 azide stretches are found at a higher frequency than either μ_2-1,3 or terminal azide. So, for **1** - **5**, the highest energy band (ranging from 2110 cm^{-1} for **1** to 2082 cm^{-1} for **4**) in each complex's spectrum is associated with the μ_2-1,1 azide bridge. The other bands in the spectra can be assigned to other bonding modes. The spectrum of **1** shows two additional azide bands at 2049 cm^{-1} and 2037 cm^{-1}, which are due to the observed terminal and μ_2-1,3 azides. Likewise, **2** and **3** show only one extra azide band each, consistent with their structures, which show only one other type of azide besides the μ_2-1,1 bridges (μ_2-1,3 azide bridges for **2** and terminal azide for **3**). Of the two complexes for which there are no structural data, **4** has only one additional band at 2037 cm^{-1} indicating only one other type of azide, while **5** has two additional bands at 2060 cm^{-1} and 2046 cm^{-1}, which suggests the presence of both terminal and μ_2-1,3 azides. A note of caution must be included here, since it has been observed that a single type of azide can give rise to more than one band in asymmetric binuclear systems.[58] Analysis for **5**, however, suggests the presence

of a tetranuclear core similar to **1** and **2** and five azide ligands, which agrees well with the presence of all three types of azide in the complex.

Other bands of interest associated with the bridging ligands are also observed in a number of other complexes. Complexes **8** and **9** show quite sharp bands at 3490 cm^{-1} and 3605 cm^{-1}, which are consistent with the OH^- bridge observed in each. The bridging sulfates found in **6** also give a very distinctive series of infrared bands in the range 951 cm^{-1} to 1183 cm^{-1}, for a total of 6 bands altogether. This is the range in which the ν_1 and ν_3 vibrations of SO_4^{2-} are usually found. Ionic sulfate normally exhibits only one broad ν_3 band at about 1100 cm^{-1}, ν_1 being IR inactive for T_d symmetry. By lowering the symmetry however, degenerate ν_3 vibrations split and the Raman active mode ν_1 is also observed.[103] The bridging sulfate ligands in **6** are nominally C_{3v} symmetry, and should give two ν_3 bands, in addition to the ν_1 vibration. The spectrum of **6** is more complicated than this, however, a consequence of the presence of three different binuclear units in the asymmetric unit, one of which contains a disordered sulfate.

Other bands of interest due to anions and/or other coordinated ligands are observed in some of the complexes. It is known[104] that the nitrate $\nu_1+\nu_4$ combination bands which are found in the range 1700 - 1800 cm^{-1} can be used for structural diagnosis. Complex **2** shows three bands in this region, while **8** shows four bands. For **2**, these are found at 1755 cm^{-1}, 1738 cm^{-1} and 1722 cm^{-1}.

This is consistent with the observed structure, which shows both ionic and monodentate coordinated nitrate. The band at 1738m^{-1} is best associated with the ionic nitrate, while the other two can be assigned to the monodentate nitrate. For **8**, the nitrate combination bands are observed at 1753 cm^{-1}, 1741 cm^{-1}, [1738 cm^{-1}] and 1731 cm^{-1}. Although it is difficult to assign specific vibrations to bonding modes in this case, the appearance of four bands suggests the presence of both monodentate and bidentate nitrate ligands. As for other anions, the spectrum of **3** shows a single strong, broad band at 1085 cm^{-1} associated with the ν_3 vibration of T_d symmetry perchlorate.[103] This is consistent with the observed structure which shows an ionic perchlorate in the lattice.

The Cu(II)-halide stretches found in the far infrared region are also of interest in determining halide coordination modes around the Cu(II) centres.[105] In general, if only one band is observed, the complex contains only terminal halide ligands. In cases where there are bridging halides as well, two bands are usually observed, with the one at lower energy being due to the bridge, a consequence of weaker bonding relative to the terminal ligand. This can be seen quite clearly in the spectrum of **7**, which exhibits Cu(II)-Cl bands at 307 cm^{-1} and 267 cm^{-1}, indicating the presence of both terminal and bridging halide in this complex. Unfortunately, for **9** it is difficult to unambiguously assign Cu(II)-Br bands due to the weakness of the spectrum. Examining these bands for the azide complexes also proves to be somewhat more difficult. This is due to the presence of a

multitude of Cu(II)-nitrogen stretching bands which lie in the same region as the Cu(II)-halide bands. As a result, although only one Cu(II)-halide band can be identified unambiguously for **4** (284 cm^{-1}) and **5** (316 cm^{-1}), it is possible that a second band does appear, but it is obscured by the Cu(II)-nitrogen bands arising from the PAP3Me ligand and azide coordination about the Cu(II) centres. Unequivical assignment of the halide bonding modes in **4** and **5** is therefore impossible.

One other band of interest associated with the PAP3Me ligand is observed in complexes **1** - **9**. If one considers that the ligand PAP3Me is essentially a substituted pyridine ligand, the pyridine ring breathing band can be used as a guide to the coordination of the pyridine moiety. In the free ligand, this band is found at 988 cm^{-1}. Upon coordination, this band increases in energy generally to ≥1000 cm^{-1}.[106] For complexes **1** - **9**, this band is observed in the range 998 cm^{-1} for **5** and **9** to 1018 cm^{-1} for **4**. The presence of this band agrees with the structures observed for **1** - **3**, and suggests for **4** - **5** and **7** - **9**, that in all of the complexes both pyridine moieties of PAP3Me are coordinated. For **6**, this band is not observed due to the presence of the complicated sulfate bands in the same region, which obscure the weaker ring breathing band. Coordination of both pyridine moieties, however, is confirmed by the X-ray structure.

The electronic spectra of all of the complexes are remarkably similar. The spectra are all characterised by intense charge transfer bands in the 360nm to

470nm region, with much less intense d-d transitions in the 590nm-720nm range. The charge transfer bands have their origin in two different transitions. First of all, complexes of PAPR ligands all show a fairly intense $\pi \rightarrow \pi^*$ transition below about 400nm.[106] For the free ligand PAP3Me, this transition is found at 375nm.[107] The other transitions which contribute to the bands in this range involve the other ligands, notably the azide, halide, and hydroxide ligands. Very intense $\pi^*_{azide} \rightarrow Cu$ charge transfer bands are observed for equatorial Cu / azide species at ≥405nm.[46,108-110] For bridging azides, according to group theory, this band should be split into two. In practice, however, only one band is usually seen. Similarly, halide and hydroxide complexes also show strong ligand to metal charge transfer bands in a comparable range.[111]

For all of the complexes reported herein then, we would expect to see two intense charge transfer bands; one below ~400nm associated with the PAP3Me ligand and one above ~400nm associated with the azide or halide ligands. As can be seen in Tables 4.7 and 4.8, in most of the complexes this is the case. In the spectra of some complexes, however, only one band is observed. For example, **3** shows only one mull transmittance band at 400nm (410nm in DMF solution), and **7** shows only one band at 420nm (410nm in DMF solution). This is undoubtedly due to overlap between two charge transfer bands of similar energy. Indeed, the charge transfer bands in these examples are quite broad, indicating the combination of more than one band in this region.

The d-d transition bands are likewise similar for all of the complexes. All are very broad in both the mull transmittance and DMF solution spectra, thereby making any structural assignment based on these bands difficult. A few observations should be noted however. First, all of the complexes exhibit d-d transitions in the range 590nm to 720nm, which are typical for five or six coordinate Cu(II) complexes. This agrees well with the crystal structures, which all show five or six coordinate Cu(II) centres. Secondly, the wavelength of the d-d band differs only slightly for mull transmittance and DMF solution. This suggests that the geometry of the Cu(II) centres is essentially the same in the DMF solution as in the solid state. In contrast, a shift in wavelength is observed for the charge transfer bands in several complexes, for example in **4** (410nm in DMF to 360nm in mull) and **8** (450nm in DMF, 370nm in mull).

4.3.2 Proposed Structures Based on Spectroscopic and Analytical Data

The suggested structures of those complexes for which X-ray crystallographic data could not be obtained are based reasonably on the spectroscopic and analytical data, and comparison with the structurally characterised complexes. Diagramatic representations of the structures of **4** - **5** and **7** - **9**, determined by this procedure, are shown in Fig.4.10 and Fig.4.11 respectively. An unambiguous determination of the structure of the azide complexes proved especially difficult, due to the variety of bonding modes

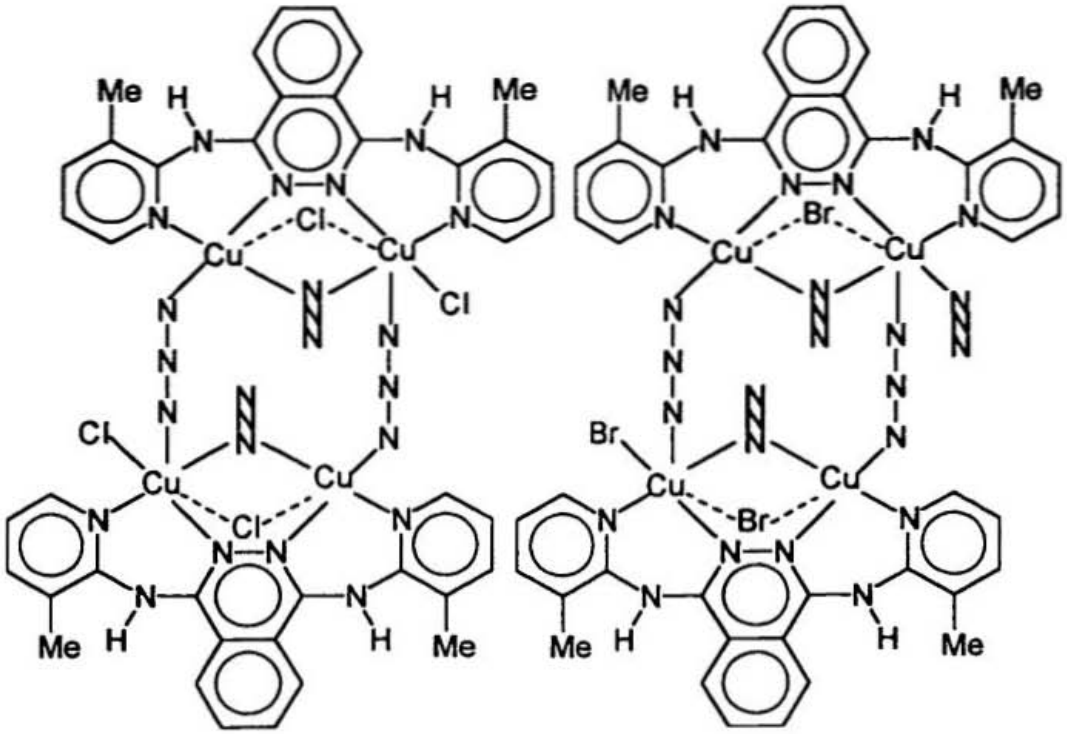

(4)A (5)

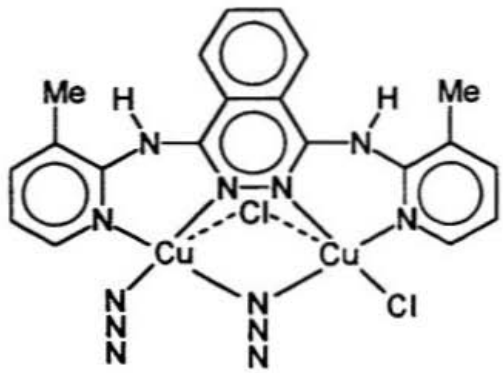

(4)B

Fig. 4.10 Proposed structure of $[Cu_2(PAP3Me)(N_3)_2Cl_2](CH_3OH)_{1.5}$ (4) and $[Cu_4(PAP3Me)_2(N_6)_6Br_2]$ (5) Based on Spectroscopic and Analytical Data.

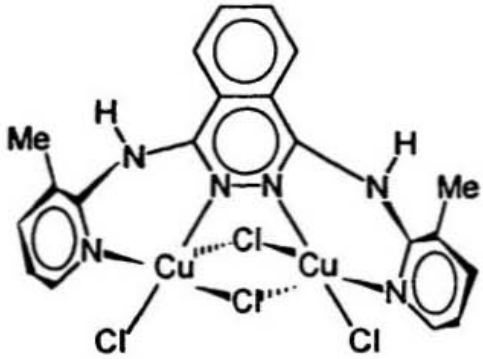

(7)

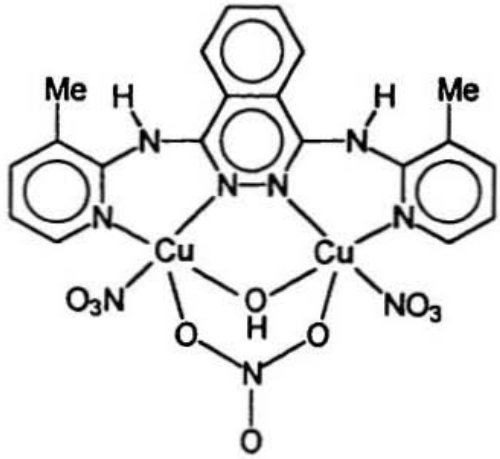

(8)

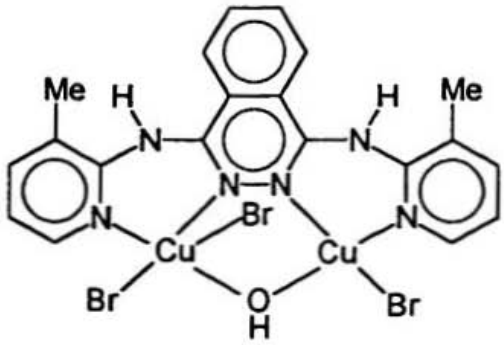

(9)

Fig. 4.11 Proposed Structure of $[Cu_2(PAP3Me)Cl_4]$ (7) { (-----) axial contact, (——)equitorial contact}, $[Cu_2(PAP3Me)(OH)(NO_3)_3](H_2O)$ (8) and $[Cu_2(PAP3Me)(OH)Br_3]$ (9) Based on Spectroscopic and Analytical Data.

available to the azide ligands. As is seen in the crystal structures of **1** and **2**, the azide ligand can form several types of bridges as well as act as a terminal ligand, all of which are difficult to distinguish by spectroscopic means. For **4**, it is uncertain if the complex exists as a simple binuclear unit, or as a tetranuclear structure similar to **1** and **2**. A proposed structure for each case, which agrees

with the available data, is shown in Fig.4.10. It should be noted that the apical chloride ligands are shown as bridges with broken lines representing the bonds. This indicates that it is uncertain if the chloride ligands are bridging or terminal, for the reasons outlined in the previous section. A similar uncertainty is illustrated for **5** with respect to the bromide ligands. In this case, however, we can be quite certain that a tetranuclear unit is formed on the basis of the analytical data. As for the methanol solvent indicated by the analytical data for **4**, it is most likely that this exists as lattice solvent. There are no bands observed in the far infrared which could be attributed to Cu(II)-oxygen stretches for coordinated methanol, although the possibility cannot be discounted. It is possible that any such bands are obscured by the intense and numerous Cu(II)-nitrogen bands found in the same region.

Assigning appropriate structures to **7** - **9**, as shown in Fig.4.11, is more straightforward because of their similarity to previously studied binuclear Cu(II) complexes of the PAPR class of ligands. For **7**, both terminal and bridging chloride ligands are evident from the infrared spectrum. The chloride bridges are most likely axial / equatorial, similar to the μ_2-O-SO_3 bridges in **6**. This bridging mode is often observed in halide complexes of related diazine ligands.[27,28,89-94] In addition, the magnetic behaviour of **6** and **7** are essentially identical (*vide supra*), suggesting identical magnetic exchange pathways via the phthalazine diazine

bridge only, a consequence of the orthogonal nature of the other axial / equatorial bridges in both complexes.

The magnetic behaviours of **8** and **9** also aid in assigning appropriate structures to both complexes. Both are relatively strongly coupled (-2J >300 cm^{-1}, *vide supra*) for hydroxy bridged PAPR complexes.[93] This suggests the presence of fairly large hydroxide bridge angles, perhaps around 110°. Since the PAP3Me ligand should result in a somewhat smaller angle, there must be other structural features which would account for this angle. For **8**, it is likely that the bidentate nitrate observed in the infrared spectrum is bridging the two Cu(II) centres in an axial position, a situation which is known to give increased Cu-Cu separations, and hence larger bridge angles, in other Cu(II) / PAPR systems.[93] The coordination sphere around each Cu(II) centre is completed by equatorial, monodentate nitrate ligands. For **9**, it is difficult to tell on the basis of the infrared spectrum if there is a bridging axial bromide ligand, often observed in similar complexes, due to the inconclusive infrared data. The large magnetic coupling value, however, suggests that there is no axial bromine bridge. This would result in a smaller hydroxy bridge angle of ~100°, [93] which would give much weaker magnetic coupling (<200 cm^{-1}) than is actually observed. The three bromide ligands are thus most likely all terminal, two equatorial and one axial.

Although not all of these structural assignments are certain, it is important to note that from the point of view of magnetic properties, the uncertainty is not a

critical problem. The proposed structures exhibit the same type of magnetic bridges between the Cu(II) centres. The proposed azide structures all contain only diazine and μ_2-1,1 azide magnetic bridges, while the hydroxy structures contain diazine and hydroxy magnetic bridges. Apart from playing a role in determining the dimensions of the binuclear centre, the presence or absence of an axial bridging ligand is irrelevant, since it would link non-magnetic orbitals.

4.4 Magnetism

4.4.1 Magnetochemistry of the Cu(II) / PAP3Me / Azide Complexes

The primary interest in this study was to investigate the magnetochemical behaviour of the Cu(II) / PAP3Me complexes and establish magnetostructural correlations. The experimental variable temperature magnetic susceptibility data for complexes **1** - **3** are shown in Fig.4.12. Also included are the μ_2-1,1 azide bridge angles and the energy differences between the antisymmetric and symmetric molecular orbital (Δ's) as calculated from Extended Hückel molecular orbitals calculations using the structural data. The observed χ_M vs. T plots are typical of weakly coupled binuclear Cu(II) antiferromagnetic systems, with the susceptibility rising to a maximum as temperature decreases, and then dropping off at lower temperature. The T(χ_{max}) values are a rough reflection of coupling constants, and these agree with the trend in Δ values, as expected on the basis of (2.30). However, there is an apparent anomaly in the correlation between the

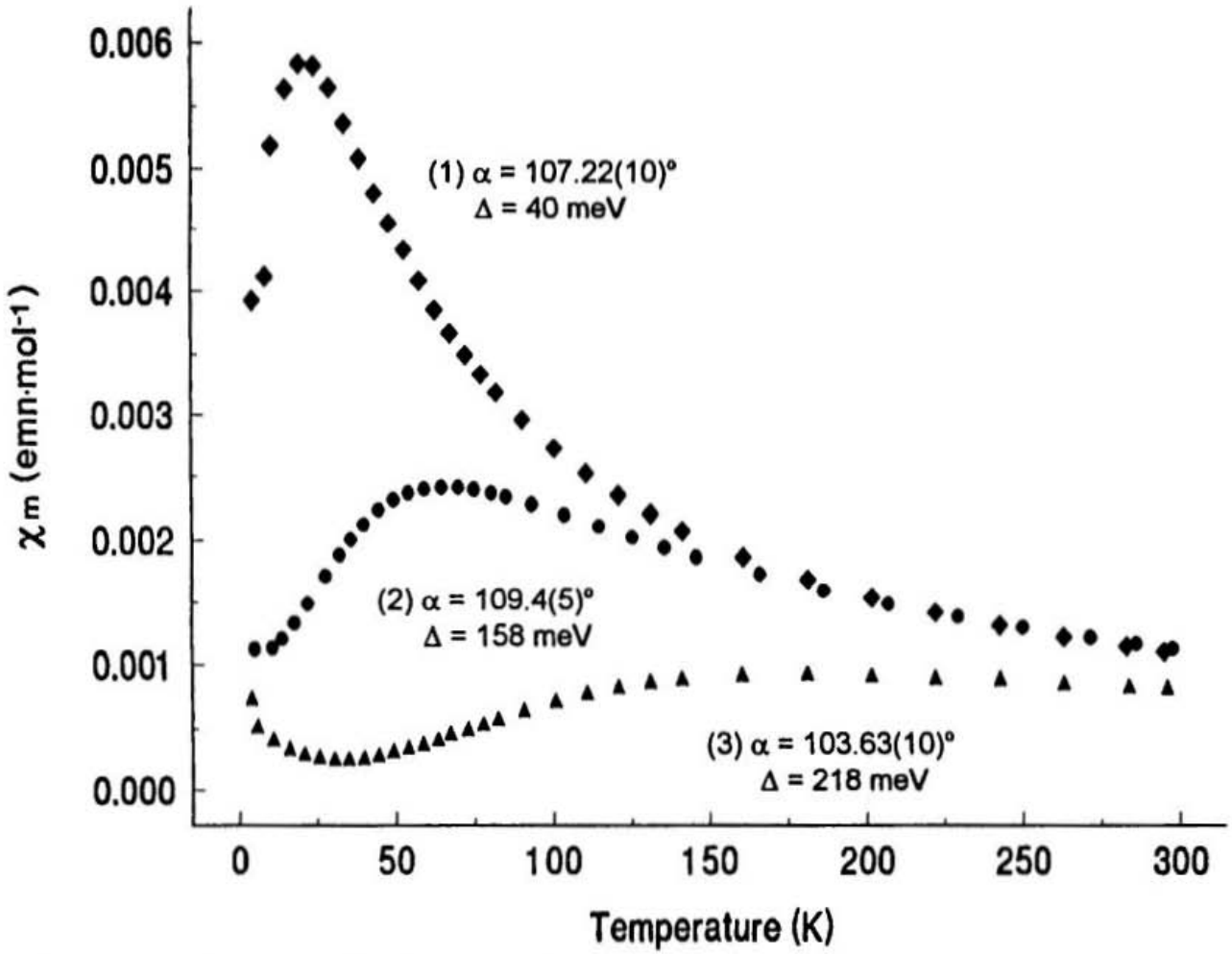

Fig. 4.12 Experimental Variable Temperature Magnetic Susceptibility Data for $[Cu_4(PAP3Me\text{-}H)_2(N_3)_4](1)$ (◆), $[Cu_4(PAP3Me)_2(N_3)_4(NO_3)_2(H_2O)_2](NO_3)_2$ (2) (●), and $[Cu_2(PAP3Me)(N_3)_3(CH_3OH)](ClO_4)$(3) (▲).

μ_2-1,1 azide bridge angle and the observed coupling. Based on the magnetostructural correlation for μ_2-1,1 azide / diazine bridged systems discussed in Chapter 3, the antiferromagnetic coupling should decrease with decreasing μ_2-1,1 azide bridge angle. Complexes **1** and **2** follow this correlation, but complex **3** with the smallest bridge angle, exhibits a maximum at a higher temperature than either **1** or **2**, and therefore is most strongly coupled.

Table 4.9 Variable Temperature Magnetic Parameters for Complexes (1)-(3), Data Fitted to the Bleaney-Bowers Equation† (Model I).

	-2J (cm^{-1})	g	ρ	10^6TIP (emu/mol)	θ (K)	10^2R
(1)	5.1(2)	2.00(1)	0.001	30	-36	3.9
(2)	38(2)	2.19(4)	0.0085	29	-79	2.46
(3)	152(9)	2.1(1)	0.009	37	-99	2.06

$$^{\dagger}\chi_m = \left[\frac{Ng^2\beta^2}{k(T-\theta)}\left(\frac{1}{3+e^{2x}}\right)\right](1-\rho) + \left(\frac{Ng^2\beta^2}{4kT}\right)\rho + N\alpha$$

Where x = J/kT
J = exchange integral
g = Landé splitting facter
ρ = fraction of paramagnetic impurity
Nα = temperature independant paramagnetism
θ = Weiss-like correction
$R = [\Sigma(\chi_{obs} - \chi_{calc})^2 / \Sigma\chi_{obs}^2]^{1/2}$

An attempt was made to fit the variable temperature susceptibility data for **1** - **3** to the Bleaney-Bowers equation. The results are tabulated in Table 4.9. The 10^2R values indicate a relatively poor fit to the experimental data overall. Of

particular interest, however, are the θ values used. In order to get any semblance of a reasonable fit of the experimental data to the Bleaney-Bowers equation, abnormally large negative values of θ had to be used (from -36K for **1** to -99K for **3**). Small θ corrections would normally account for weak intermolecular ferromagnetic or antiferromagnetic exchange interactions, and would be typical for simple binuclear systems. While significant intermolecular contacts are observed in the form of μ_2-1,3 azide bridges between binuclear units (and forming the one dimensional chain in **1**) for **1** and **2**, these are orthogonal contacts which would not make a significant contribution to the exchange. The large negative θ values are therefore anomalous.

Such a large negative θ suggests that in order to successfully model the magnetic coupling in these complexes, one must assume the presence of more than a single -2J value. On the basis of this observation, several models were used in an attempt to fit the experimental magnetic data:

I. Bleaney Bowers Model

As discussed in the preceding paragraph.

II. Tetranuclear Model

Although it has already been noted that the μ_2-1,3 azide bridges between the binuclear units should not propagate significant antiferromagnetic exchange, a fit to a rectangular

tetranuclear exchange model was attempted. A schematic representation of the model is shown in Fig.4.13. Since the exchange pathways across the μ_2-1,3 azide bridges should be similar, the expression for magnetism can be simplified by assuming $-2J_2 \approx -2J_3$. The appropriate Hamiltonian can be derived from equation (2.14) and the Van Vleck equation (2.8), and then solved to give an expression for the magnetic susceptibility[112] of the form:

$$\chi_M = F(-2J_1,-2J_2,g,T)(1-\rho) + F(g,T)\rho + N\alpha \qquad (4.1)$$

where the symbols have their usual meaning. Although both dimer and monomer impurity are often included in such equations, it was considered appropriate to use just monomer impurity in this case due to the essentially binuclear origin of the complexes.

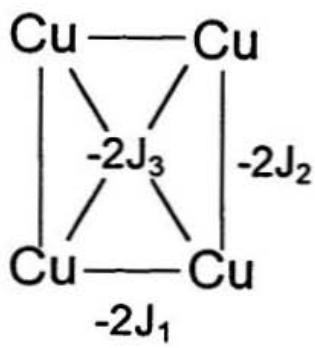

Fig. 4.13 Retangular Tetranuclear Magnetic Exchange Model.

III. Variable Temperature -2J Model

There has been some precedent in the literature for a temperature dependent -2J value. In particular, changes in the -2J values have been documented for several very weakly antiferromagnetically coupled Cu(II) systems,[77,113] the change being attributed to lattice shrinkage effects. A temperature dependent -2J has also been invoked in several other cases[114-115] involving stronger antiferromagnetic coupling. The possibility exists, therefore, that the unusual magnetic coupling observed for the complexes **1** - **3** could be modelled by a variable temperature -2J. Therefore, the Bleaney-Bowers equation was modified by replacing -2J with the empirical function for -2J versus temperature (4.2).

$$-2J = -2J_{RT} - L(299-T)^2 \qquad (4.2)$$

A quadratic expression was chosen since it gave a better fit to the experimental data than a linear expression.

The experimental data and the non-linear least squares best fit line for the different models (including the Bleaney-Bowers equation) for complexes **1**, **2** and **3** are shown in Fig.4.14, Fig.4.15, and Fig.4.16 respectively. The numerical data for Models II - III are reported in Table 4.10. A quick glance at both the χ_M vs. T plots and the 10^2R values in both Table 4.9 and Table 4.10 reveals that none of

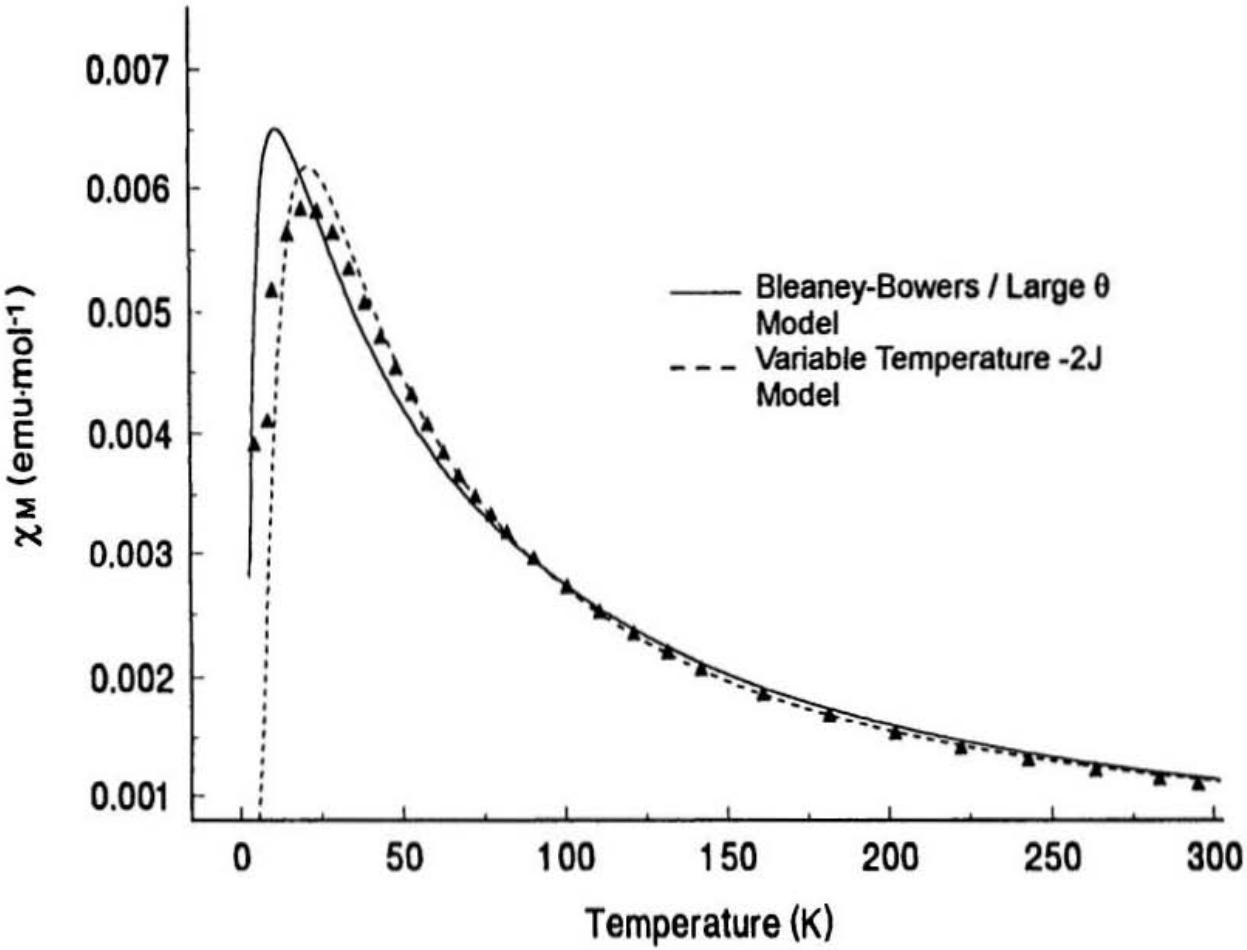

Fig. 4.14 Variable Temperature Magnetic Susceptibilty Data for $[Cu_4(PAP3Me\text{-}H)_2(N_3)_6]$(1) with Least Squares Lines for the Bleaney-Bowers Equation (I) (——), and Variable Temperature -2J Model (III) (------).

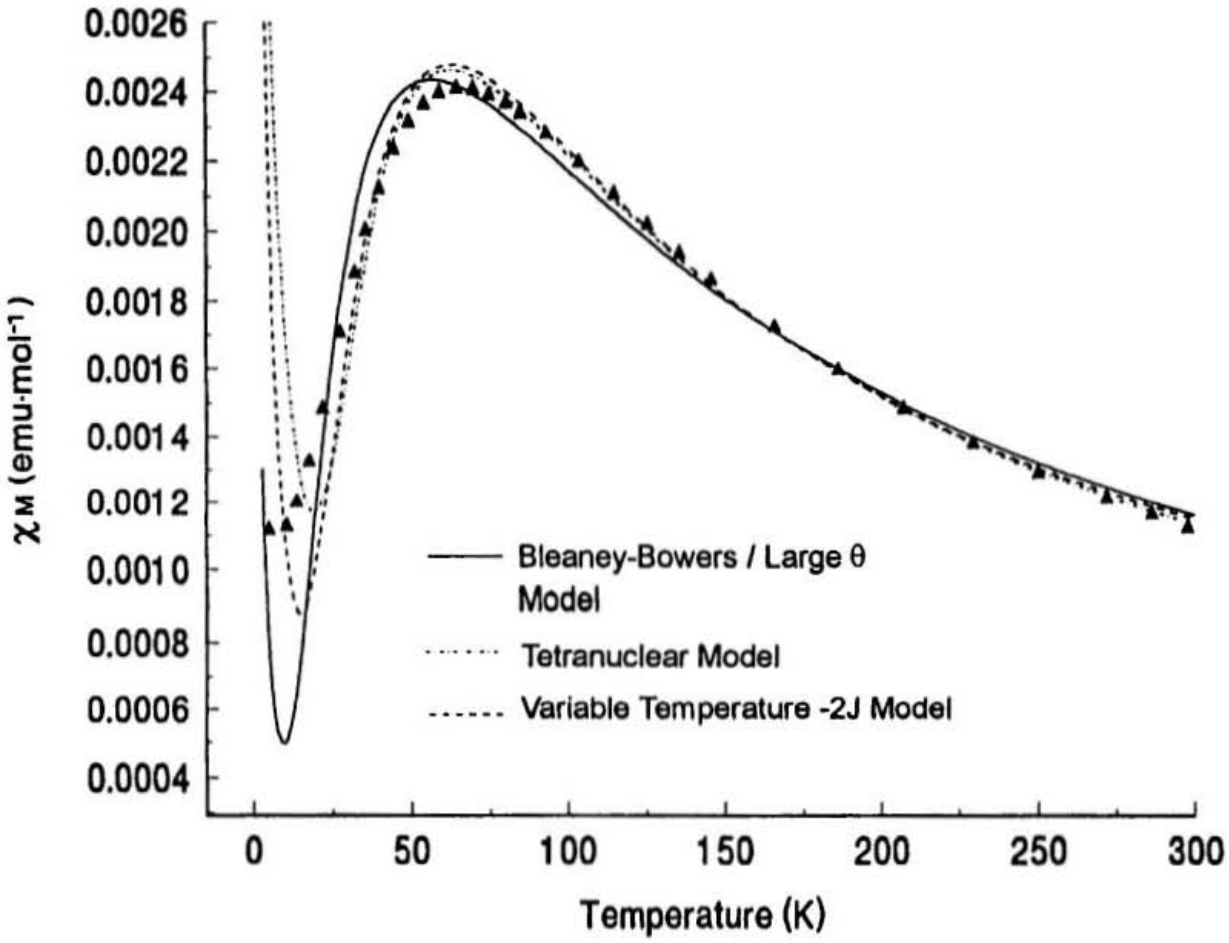

Fig. 4.15 Variable Temperature Magnetic Susceptibilty Data for $[Cu_4(PAP3Me)_2(N_3)_4(NO_3)_2(H_2O)_2](NO_3)_2$ (2) with Least Squares Lines for the Bleaney-Bowers Equation (I) (——), Tetranuclear Model (II) (-·-·-), and Variable Temperature -2J Model (III) (------).

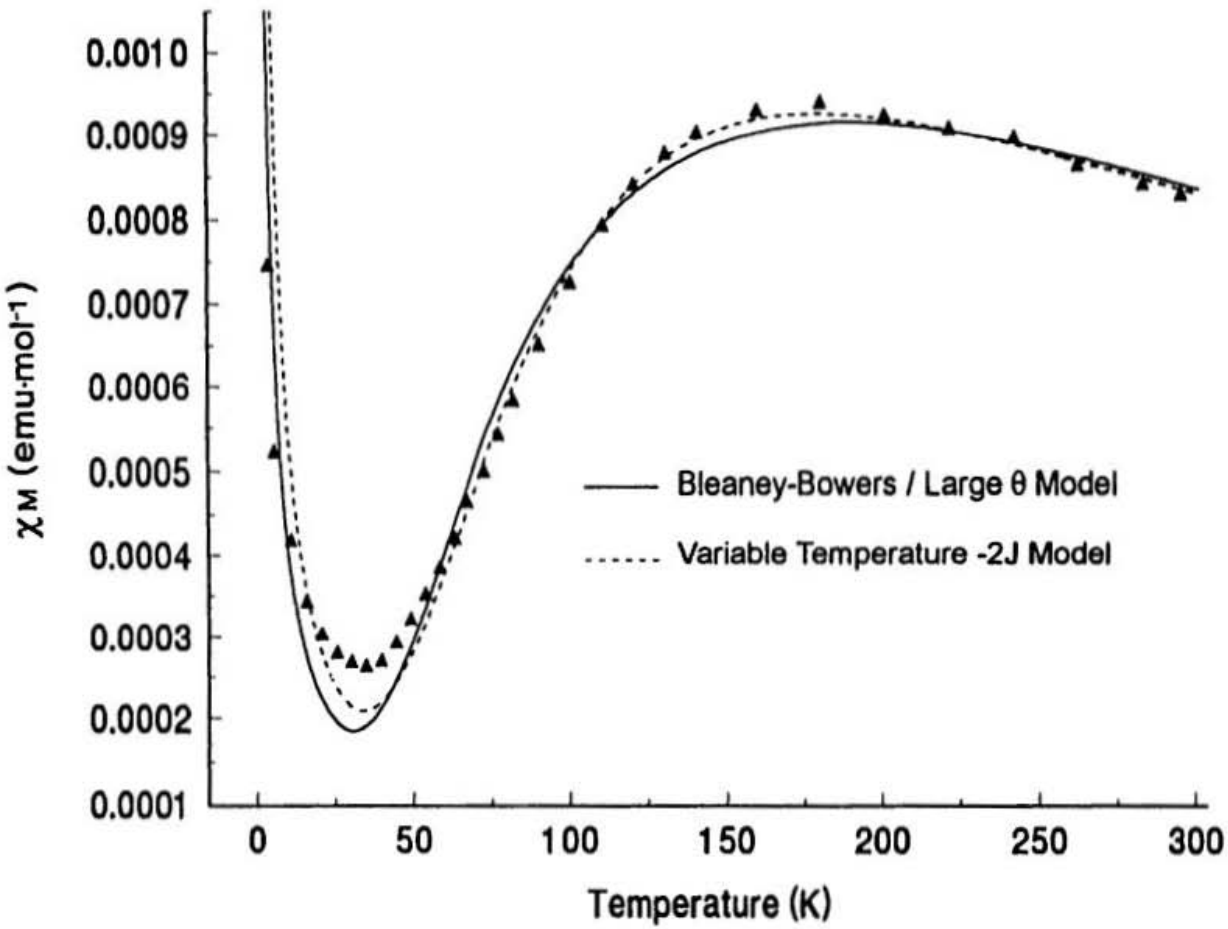

Fig. 4.16 Variable Temperature Magnetic Susceptibilty Data for $[Cu_2(PAP3Me)(N_3)_3(CH_3OH)](ClO_4)$(3) with Least Squares Lines for the Bleaney-Bowers Equation (I) (——), and Variable Temperature -2J Model (III) (------).

the proposed models are particularly well suited to fitting the experimental data. The problems with the Bleaney-Bowers model have already been addressed. For the tetranuclear model, the only complex which gave a sensible fit was **2**, the experimental data for **1** fitting only when a g value of less than 2 was used. Complex **3**, on the other hand, is not even tetranuclear, so the use of such a model would be quite inappropriate. This illustrates another problem, that the model is not generally applicable.

Table 4.10 Variable Temperature Magnetic Data for Complexes (1)-(3), Using the Tetranuclear (II) and Variable Temperature -2J (III) Models.

	Model II						
	$-2J_A$ (cm^{-1})	$-2J_B$ (cm^{-1})	g	ρ	10^6TIP (emu/mol)	θ (K)	10^2R
(1)	-	-	-	-	-	-	-
(2)	40.3(4)	20	2.04(1)	0.051	63	-2	1.57
(3)	-	-	-	-	-	-	-
	Model III						
	$-2J_{RT}$ (cm^{-1})	L (*10^3)	g	ρ	10^6TIP (emu/mol)	θ (K)	10^2R
(1)	110	1.009(9)	2.03(1)	0.0005	25	0	2.33
(2)	150	1.01(2)	2.13(1)	0.025	20	0	1.67
(3)	250	1.081(7)	2.01(1)	0.014	25	0	1.36

The best model appears to involve a variable temperature -2J, both in terms of a sound physical and theoretical basis supporting the model, as well as giving in general the best fits to the experimental data. Unfortunately, the model is not in agreement with the variable temperature crystal structure of **1**. As has already been noted, the structure of **1** changes very little as the temperature

changes. Some relevant bond angles and distances for the binuclear Cu(II) centre of **1** at the four different temperatures are given in Table 4.11. The μ_2-1,1 azide bridge angle changes only by ~0.5° between 290K and 90K, and then increases again at 50K. While this angle change is a physical reality, it is not significant enough to account for the observed anomalous magnetism. Using the previously reported correlation[59] for azide bridge angle with -2J, the two extreme values for the μ_2-1,1 azide bridge angle in **1** give -2J values of 68 cm^{-1} (290K) and 50 cm^{-1} (90K), a difference of only 18 cm^{-1}. Using (4.2) and the L value for **1** from Table 4.10 gives -2J values of 110 cm^{-1} (290K) and 66 cm^{-1} (90K), for a difference of 44 cm^{-1}.

Table 4.11 Selected Bond Distances for $[Cu_4(PAP3Me\text{-}H)_2(N_3)_6]$ (1) From the Variable Temperature X-Ray Data.

	50K	90K	150K	290K
Cu(1)-N(10)	1.990(3)	1.992(2)	1.987(2)	1.984(3)
Cu(2)-N(10)	1.967(3)	1.966(2)	1.964(2)	1.963(3)
Cu(1)-N(3)	1.969(3)	1.961(2)	1.958(2)	1.959(3)
Cu(2)-N(4)	2.024(3)	2.019(2)	2.015(2)	2.017(3)
N(3)-N(4)	1.384(4)	1.391(3)	1.391(2)	1.394(3)
Cu(2)-N(10)-Cu(1)	107.23(13)	107.16(10)	107.22(10)	107.60(14)
N(3)-Cu(1)-N(10)	85.33(11)	85.33(8)	85.64(8)	85.81(12)
N(10)-Cu(2)-N(4)	84.84(11)	84.88(8)	84.93(8)	85.26(11)
N(4)-N(3)-Cu(1)	117.4(2)	117.42(13)	117.08(13)	117.2(2)
N(3)-N(4)-Cu(2)	116.2(2)	116.15(13)	116.44(13)	116.3(2)

The experimental data and the non-linear least squares best fit lines for complexes **4** and **5** are shown in Fig.4.17. The most notable feature of these

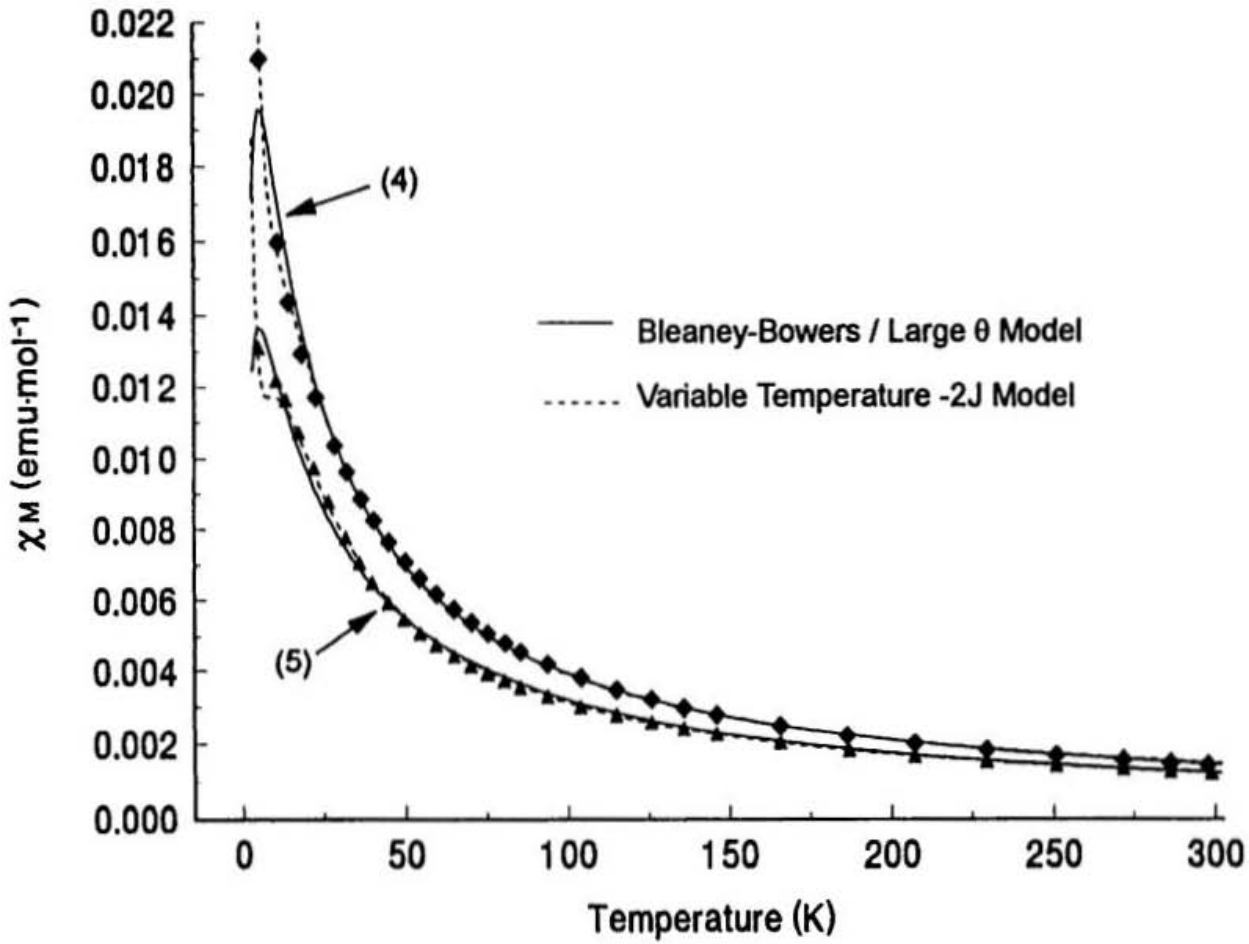

Fig. 4.17 Variable Temperature Magnetic Susceptibilty Data for $[Cu_2(PAP3Me)(N_3)_2Cl_2](CH_3OH)_{1.8}$(4) (◆) and $[Cu_4(PAP3Me)_2(N_3)_6Br_2]$ (5) (▲) with Least Squares Lines for the Bleaney-Bowers Equation (I) (——), and Variable Temperature -2J Model (III) (------).

plots is that there is no obvious maximum as is expected for an antiferromagnetic system. The systems are so weakly coupled that the maximum lies at a temperature below that of the lowest measured temperature (< 5K). ESR spectra for the two complexes show only very weak signals, confirming that the two centres are coupled and not simply isolated paramagnetic centres. It would appear then that **4** and **5** both lie very close to the crossover between ferromagnetism and antiferromagnetism.

Table 4.12 Variable Temperature Magnetic Data for Complexes (4)-(5), Using the Bleaney-Bowers Equation (I) and Variable Temperature -2J Model (III).

	Model I					
	$-2J$ (cm^{-1})	g	ρ	10^6TIP (emu/mol)	θ (K)	10^2R
(4)	2.7(4)	2.17(1)	0.00004	44.5	-12.5	1.74
(5)	2.2(3)	2.00(1)	0.00005	42	-17.6	2.12
	Model III					
	$-2J_{RT}$ (cm^{-1})	L ($*10^3$)	g	ρ	10^6TIP (emu/mol)	θ (K)	10^2R
(4)	97(5)	0.884(2)	2.28(1)	0.23	20	0	1.99
(5)	100(3)	0.95(2)	2.06(1)	0.14	59	0	1.18

Similar problems manifest themselves in complexes **4** and **5** as were observed for **1** - **3** with respect to fitting the experimental data to a model for the magnetic coupling. The best fit parameters for the Bleaney-Bowers model and variable temperature -2J model are shown in Table 4.12. Neither complex gives a good fit of the experimental data to the Bleaney-Bowers equation unless relatively large negative θ values are included, albeit not as large as was

required for **1 - 3**. Fitting to the variable temperature -2J model does not give a significantly improved data fit, and in fact presents yet another problem: a very large paramagnetic impurity must be used to fit the data. In fact, 23% and 14% paramagnetic impurities had to be assumed for **4** and **5**, respectively. Such large ρ values are simply unrealistic, a conclusion further supported by the very weak ESR signals. One would expect a relatively strong ESR signal if there was in fact that large a paramagnetic impurity. As for **1 - 3** then, it appears that the magnetic data for **4 - 5** cannot be reasonably fitted using the available models for magnetic exchange. It would be most helpful to have structural data on these compounds, but so far X-ray quality crystals have not been produced.

The question then arises as to whether there are any other properties which could provide a rationale for the unusual magnetic behaviour of complexes **1 - 5**. In fact, a possible origin is found in the Extended Hückel calculations performed on the crystal structures **1 - 3**. The Φ_S and Φ_{AS} orbitals for each structure are shown in Fig.4.18. For complexes **1** and **2**, the most notable characteristic is the asymmetry in both orbitals. Ideally in a symmetric case, each orbital should contain equal contributions from both halves of the binuclear centre. In complexes **1** and **2**, Φ_S is centred largely on one Cu(II) centre, while Φ_{AS} is centred on the other. They also show significant orbital contribution from the pyridine rings. This phenomenon is particularly pronounced for **2**, in which the Φ_S and Φ_{AS} orbitals are almost completely localised on opposite Cu(II)

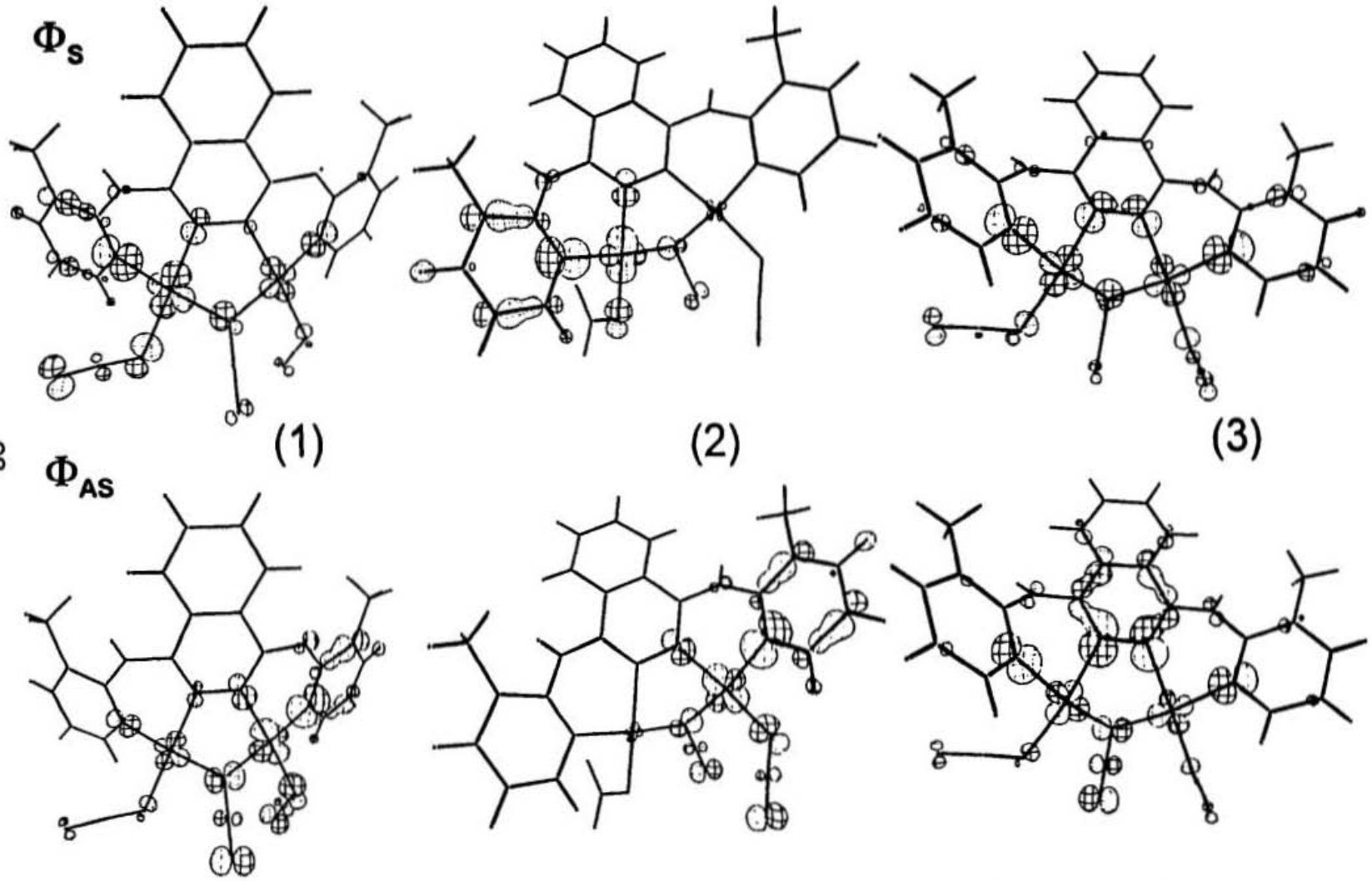

Fig. 4.18 Extended Hückel Molecular Orbital Calculations for Complexes (1)-(3): Φ_s and Φ_{AS} Orbitals.

centres. The reasons for this anomaly are not clear. Asymmetry in the bond lengths and/or bond angles for the two Cu(II) centres is an obvious possibility, but the differences in these parameters are no greater than that observed for similar systems in which no anomalous magnetism is observed.[58,59] The precise cause remains a mystery.

The Extended Hückel calculations also provide an explanation for the unusually strong coupling observed for **3**. As previously noted, since **3** contains the smallest μ_2-1,1 azide bridge angle, it would be expected to have the weakest antiferromagnetic (or even ferromagnetic) coupling. However, recalling Hoffman's and Kahn's work on dibridged systems, at some angle below that of accidental orthogonality, it is expected that antiferromagnetic coupling should again predominate. In such a case, the main difference would be an inversion of the energies of the molecular orbitals. That is, Φ_S and Φ_{AS} switch relative energy, with Φ_S now being at higher energy than Φ_{AS}. EHMO calculations on **3**, however, reveal that this is not so: Φ_S still lies lower in energy than Φ_{AS}. What is interesting is the strong phthalazine contribution to the molecular orbitals, especially to Φ_{AS}. Generally, the only contribution observed from the phthalazine is localised on the diazine nitrogen atoms. The delocalization over the phthalazine ring suggests that it is making a much larger contribution to the overall antiferromagnetic coupling than is usual. Therefore, even though at such a small azide bridge angle it is expected that coupling should be very weakly

antiferromagnetic or ferromagnetic, the diazine bridge dominates, resulting in relatively strong antiferromagnetic coupling.

4.4.2 Magnetochemistry of the Other Cu(II) / PAP3Me Complexes

In contrast to the unusual magnetic properties observed for the azide complexes **1** - **5**, the non-azide complexes **6** - **9** all exhibit magnetic coupling typical for binuclear Cu(II) systems. The data were successfully fitted to the Bleaney-Bowers equation with no difficulty. The best fit data for complexes **6** - **9** are reported in Table 4.13. The experimental data and non-linear least squares best fit lines for **6** - **7** and **8** - **9** are plotted in Fig.4.19 and Fig.4.20, respectively.

Table 4.13 Variable Temperature Magnetic Parameters for Complexes (6)-(9), Fitted to the Bleaney-Bowers Equation.

	$-2J$ (cm^{-1})	g	ρ	10^6TIP (emu/mol)	θ (K)	10^2R
(6)	95.2(5)	2.21(1)	0.0305	105	-7	0.86
(7)	94.7(3)	2.05(1)	0.00865	82.8	-8	0.48
(8)	327(2)	2.01(1)	0.03	62	-3	1.36
(9)	313(4)	2.06(1)	0.044	54	-2	2.66

The four complexes can be separated into two groups based on their magnetic behaviour. Both **6** and **7** are weakly antiferromagnetically coupled, and in fact have essentially the same coupling value of ~95 cm^{-1}. This is quite interesting in light of their structures. Complex **6** contains only one magnetic bridge, that being the phthalazine diazine, since the two μ_2-O-SO_3 bridges link the Cu(II) centres via axial / equatorial contacts. Based on spectroscopic and

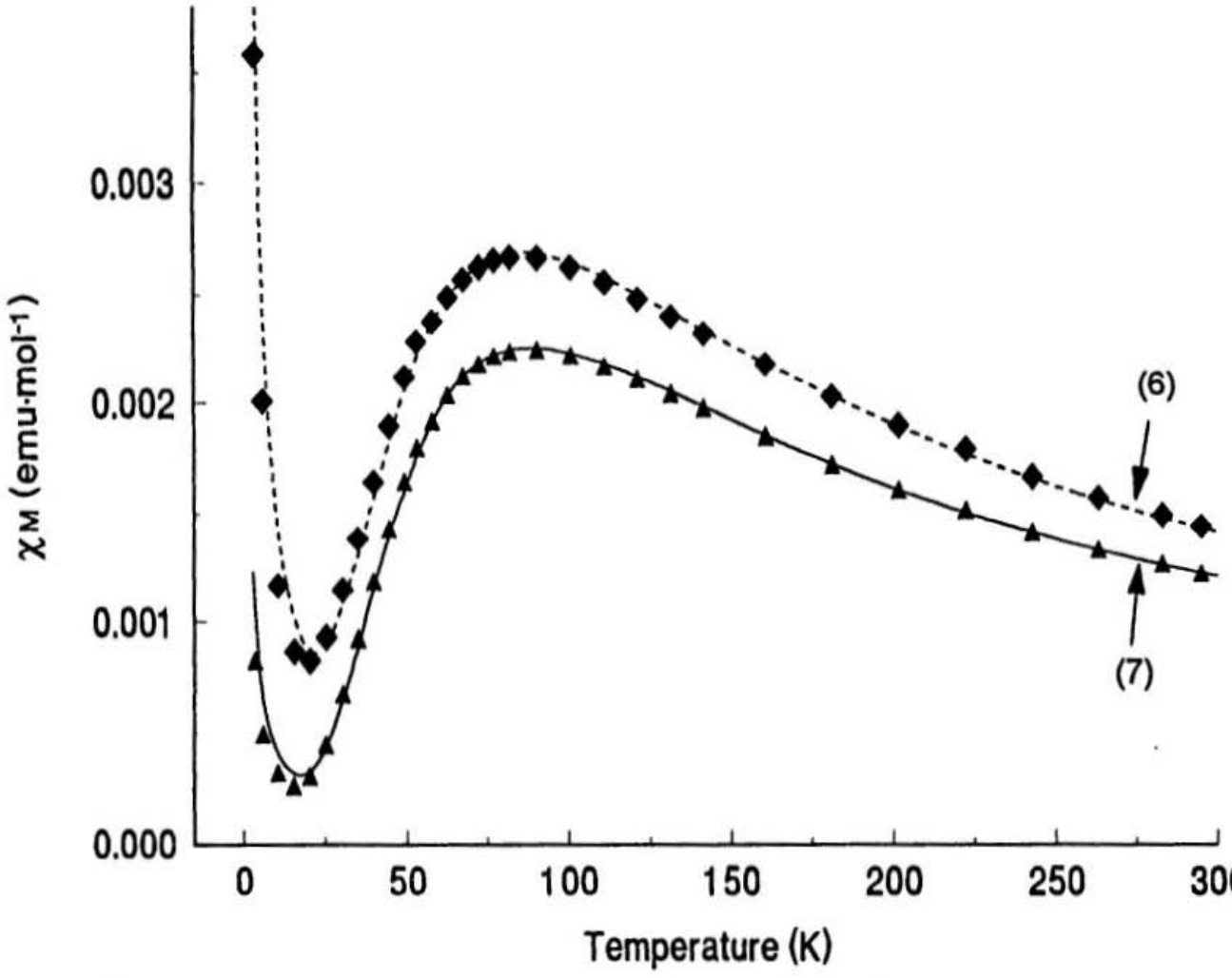

Fig. 4.19 Variable Temperature Magnetic Susceptibility Data for $[Cu_2(PAP3Me)(SO_4)_2(H_2O)_4](H_2O)$(6) (◆) and $[Cu_2(PAP3Me)Cl_4]$ (7) (▲) with Bleaney-Bowers Equation Least Squares Best Fit Lines.

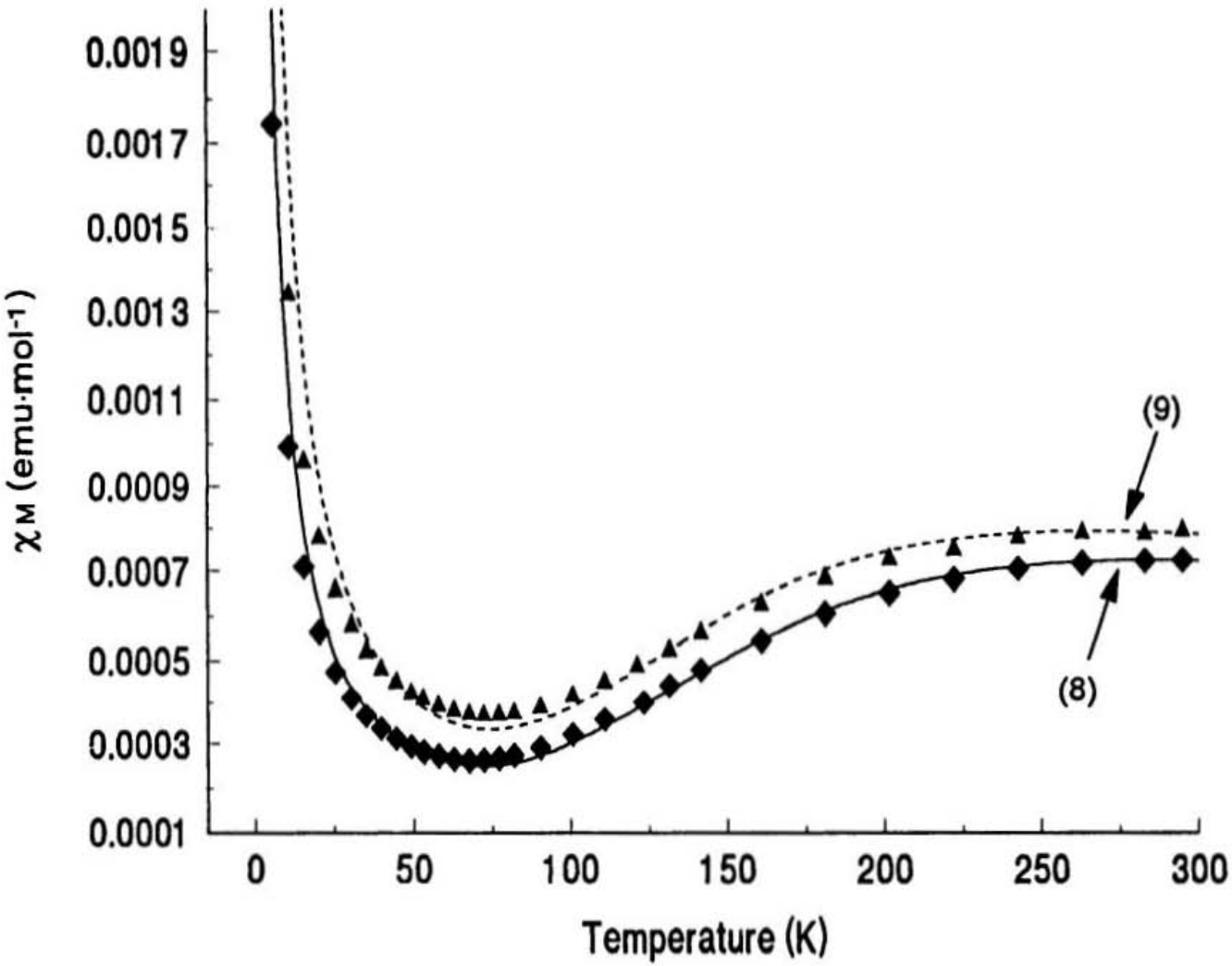

Fig. 4.20 Variable Temperature Magnetic Susceptibilty Data for $[Cu_2(PAP3Me)(OH)(NO_3)_2](NO_3)(H_2O)$ (8) (◆) and $[Cu_2(PAP3Me)(OH)Br_3]$ (9) (▲) with Bleaney-Bowers Equation Least Squares Best Fit Lines.

analytical evidence, it appears that complex **7** is also coupled only through the diazine bridge, the chlorine bridges again being axial / equatorial. These two complexes lend support to the assumption which was made earlier, that the contribution of the diazine bridge to the overall antiferromagnetic coupling is essentially constant. So, as previously stated, the change in magnetic coupling in the μ_2-1,1 azide complexes can reasonably be attributed to the changing μ_2-1,1 azide bridge angle alone.

One other feature of the magnetic behaviour for **6** - **7** is worth noting. Both required somewhat larger than usual negative θ values. Again, these are nowhere near as extreme as for **1** - **5**, and likely do represent minor intermolecular antiferromagnetic exchange components. For **6**, the most obvious pathway for this is via the extensive hydrogen bonding network previously noted (Appendix C). Unfortunately, for **7** there are no structural data and therefore no indication of the origin of this intermolecular exchange term.

Similar to **6** - **7**, complexes **8** - **9** also form a matched pair in terms of magnetic behaviour. The profile of the χ_M vs T plot for both is very similar, and the magnitude of the coupling is also similar, as would be expected. Both complexes are more strongly coupled than **6** and **7**, due to the presence of both diazine and hydroxy magnetic bridges. Moderate to strong antiferromagnetic coupling through hydroxy bridges is well documented, as is the combination of diazine and hydroxy bridges.[93] The magnitude of the coupling does in fact agree

well with other Cu(II)-hydroxy complexes of the PAPR series of ligands, and suggests a relatively large hydroxy bridge angle of ~110°. The similar coupling values for **8** - **9** suggest similar hydroxy bridge angles as well. Small negative θ values were again required to fit the data, although the pathway of intermolecular exchange is uncertain due to the absence of structural data. Fairly significant paramagnetic impurity is also observed in both the best fit data and the χ_M vs T plot. The other parameters used to fit the data are typical. The 10^2R value for **9** is a little large, but this is most likely not an indication of a poor model for the behaviour, but rather due to the rather small sample size (~15mg) available for the variable temperature experiment.

4.5 EHMO Model Studies of the Cu(II), μ_2-1,1 Azide / Diazine Bridged System

The extensive range of both bonding modes and magnetic behaviour observed for azide bridged transition metal complexes has spawned a number of semiquantitative Extended Hückel molecular orbital model calculations in attempts to better understand and predict the magnetic behaviour of azide systems. As discussed in Chapter 3, these include Kahn's original studies on the μ_2-1,1 azide dibridged Cu(II) system,[32,47] several μ_2-1,3 azide models,[39,51-53] and Ni(II) and Mn(II) μ_2-1,1 azide models.[39,69] All of these studies have focused, however, on systems with just azide bridges. In contrast, the theoretical examination of azide mixed bridge systems has been largely neglected. To date,

only qualitative work concerning complementarity and countercomplementarity in hetero bridged azide systems[116-118] and a recent semiquantitative examination of such systems concerning complementarity and countercomplementarity effects in μ_2-1,1 azide / pyridazine and μ_2-1,1 azide / carboxylato systems,[33] respectively, have been reported. Neither of these studies, however, examined in detail the change in the magnetic coupling as a consequence of controlled variation in the geometry around the dibridged metal centres, but were performed to aid elucidation of the mechanism of magnetic exchange in specific complexes. In contrast to azide complexes, the diazine bridge has received much less attention theoretically. Apart from the aforementioned hetero dibridged system, only one Extended Hückel study of binuclear model systems containing solely pyridazine bridges has been reported.[119]

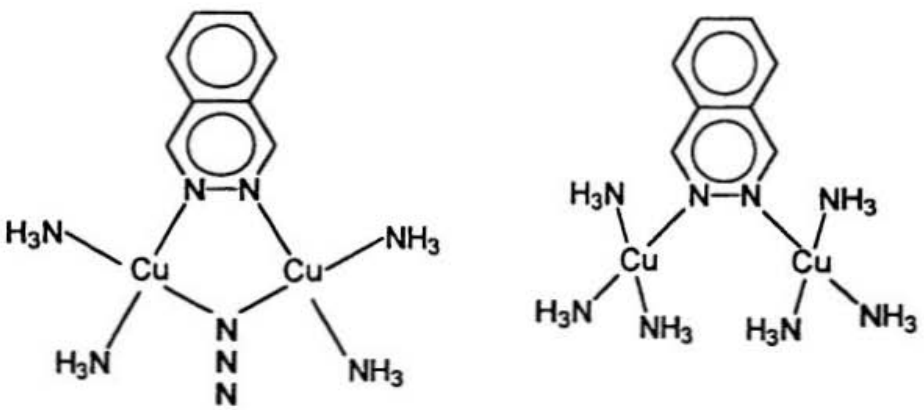

M1 **M2**

Fig. 4.21 Model Complexes Used in the EHMO Study: Phthalazine μ_2-1,1 Azide Bridged (M1) and Phthalazine Bridged (M2).

Table 4.14 Angles and Bond Distances Used for the EHMO Model Complexes M1 and M2.

C-C	1.40Å
C-H	1.10Å
C-N	1.32Å
N-N(diazine)	1.38Å
Phthalazine Angles	120°
N-N(azide)	1.20Å
Cu-N(diazine)	1.99Å
Cu-N(amine)	1.97Å
Cu-N(azide)	1.96Å
N-Cu-N (all)	90°

In an effort to better understand what types of geometric changes in the binuclear centre of the PAP3Me / μ_2-1,1 azide system affect the magnitude of the antiferromagnetic exchange, a series of Extended Hückel calculations were carried out on model complexes containing both a μ_2-1,1 azide and a phthalazine bridge (**M1**), and containing just a phthalazine bridge (**M2**), as shown in Fig.4.21. Bond distances and angles used for the phthalazine moiety and the bond distances used for the Cu(II) coordination sphere are given in Table 4.14. For the phthalazine moiety, standard values were used, while for the Cu(II) coordination sphere average values were calculated from the available crystal structures. A total of five geometric changes were examined:

I. Variation of Cu-N_3-Cu Angle in Model Complex M1

The correlation between the μ_2-1,1 azide bridge angle and the magnitude of the observed coupling constant is the primary

Table 4.15 Five Membered Chelate Ring Angles (°) Used in EHMO Model I Calculations.

Cu-N_3-Cu	N(diazine)-Cu-N(azide)	N(diazine)-N(diazine)-Cu
90	114.5	110.5
95	110.2	112.3
100	105.9	114.1
105	101.7	115.8
110	97.6	117.4
115	93.6	118.9
120	89.6	120.4
125	85.7	121.8

focus of the present study. Therefore, the variation of the Φ_S and Φ_{AS} energies with changing μ_2-1,1 azide angle is of particular interest. Using model complex **M1**, the azide bridge angle was varied from 90-125°, while retaining the planar five membered chelate ring. In order to accomplish this, the other chelate ring angles had to also be varied, the relevant values being given in Table 4.15.

II. Variation of $N_{diazine}$-$N_{diazine}$-Cu-N_{ammine} Torsion Angle in Model Complex M2

Using model complex **M2**, the torsion angles defined by the diazine nitrogen atoms, Cu(II) centres and ammonia nitrogen were varied. That is to say, the $Cu(NH_3)_3$ coordination moiety was twisted such that it was no longer coplanar with the

phthalazine. These were both twisted in the same direction over a range 50-130°. In addition to the constant values given in Table 4.14, the Cu-$N_{diazine}$-$N_{diazine}$ angle was held constant at 117°.

III. Variation of Cu-$N_{diazine}$-$N_{diazine}$ Angle in Model Complex M2

The most critical change which may occur in the bridge geometry of the diazine is that of the Cu-N-N angle. The two angles in **M2** were varied over the range 110-125°, which easily covers the observed values for the Cu(II) / PAPR complexes. For this model study, the two $Cu(NH_3)_3$ moieties were twisted out of the phthalazine plane by 60° .

IV. Trigonal Distortion of Azide Out of Cu_2N_2(diazine) Plane in Model Complex M1

This geometric distortion takes the planar model complex **M1** and twists the bridging azide out of the plane of the molecule, while maintaining a constant Cu-N_3-Cu bridge angle. All other angles in the five member chelate ring also remained constant, these values being: Cu-$N_{diazine}$-$N_{diazine}$ 120°, N-Cu-N 90°, and Cu-N_3-Cu 120°.

V. Fold of Bridging Azide out of Cu_2N_2(diazine) Plane in Model Complex M1

This distortion again involves moving the bridging azide out of the Cu_2N_2(diazine) plane. However, in this case, it folds out of the plane along the Cu-Cu axis. This can be likened to folding an envelope flap from open to closed. Again, as above, all of the angles in the five membered chelate ring are kept constant, using the same values as in **IV**. In addition, the square planar coordination geometry about the Cu(II) centres is retained as much as is possible.

The internal coordinate input files for these five studies are given in Appendix E, and the results of the these studies are presented as plots of the Φ_S and Φ_{AS} orbital energies versus the appropriate geometric distortion in Fig.4.22 - 4.26 for EHMO calculations **I-V**, respectively. Recalling that the antiferromagnetic coupling term $J_{AF} \propto (\varepsilon_{AS}-\varepsilon_S)^2$, any plot which shows significant changes in the energy difference between the Φ_S and Φ_{AS} orbitals should in turn result in changes in the antiferromagnetic coupling term. Fig.4.22 shows the results for **I** involving just the variation of Cu-N_3-Cu angle. On the basis of Kahn's molecular orbital calculations on the dibridged μ_2-1,1 azide systems,[32,47] and Thompson's experimental correlation for μ_2-1,1 azide bridge angle versus magnetic coupling,[59] it is expected that the Φ_S and Φ_{AS} orbitals should exhibit accidental orthogonality at some point, in the range 100° -110°. In fact, although

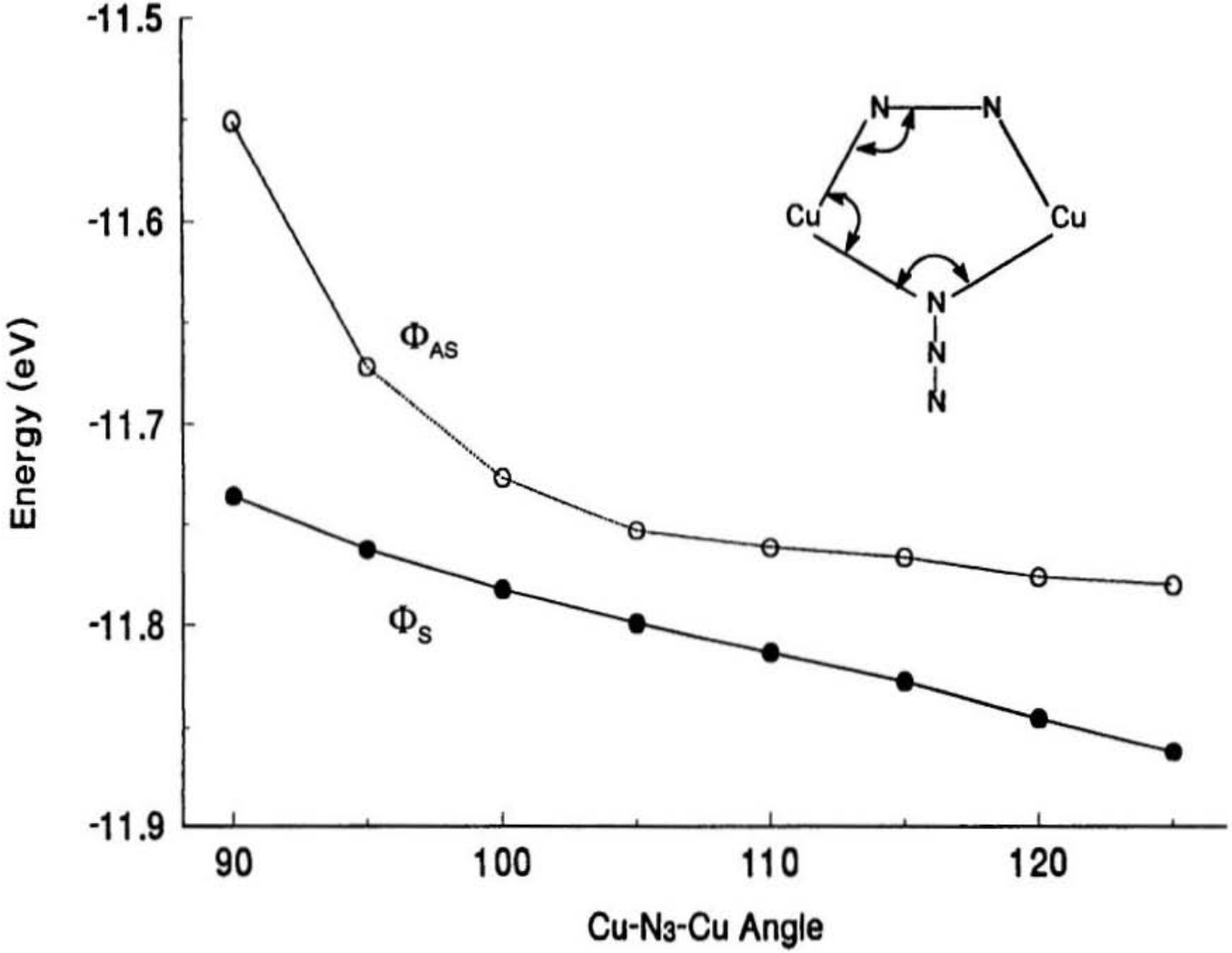

Fig. 4.22 Variation of Φ_s and Φ_{AS} Molecular Orbital Energies as a Function of Cu-N_3-Cu Angle in a Planar Five-Membered Ring (EHMO Model I).

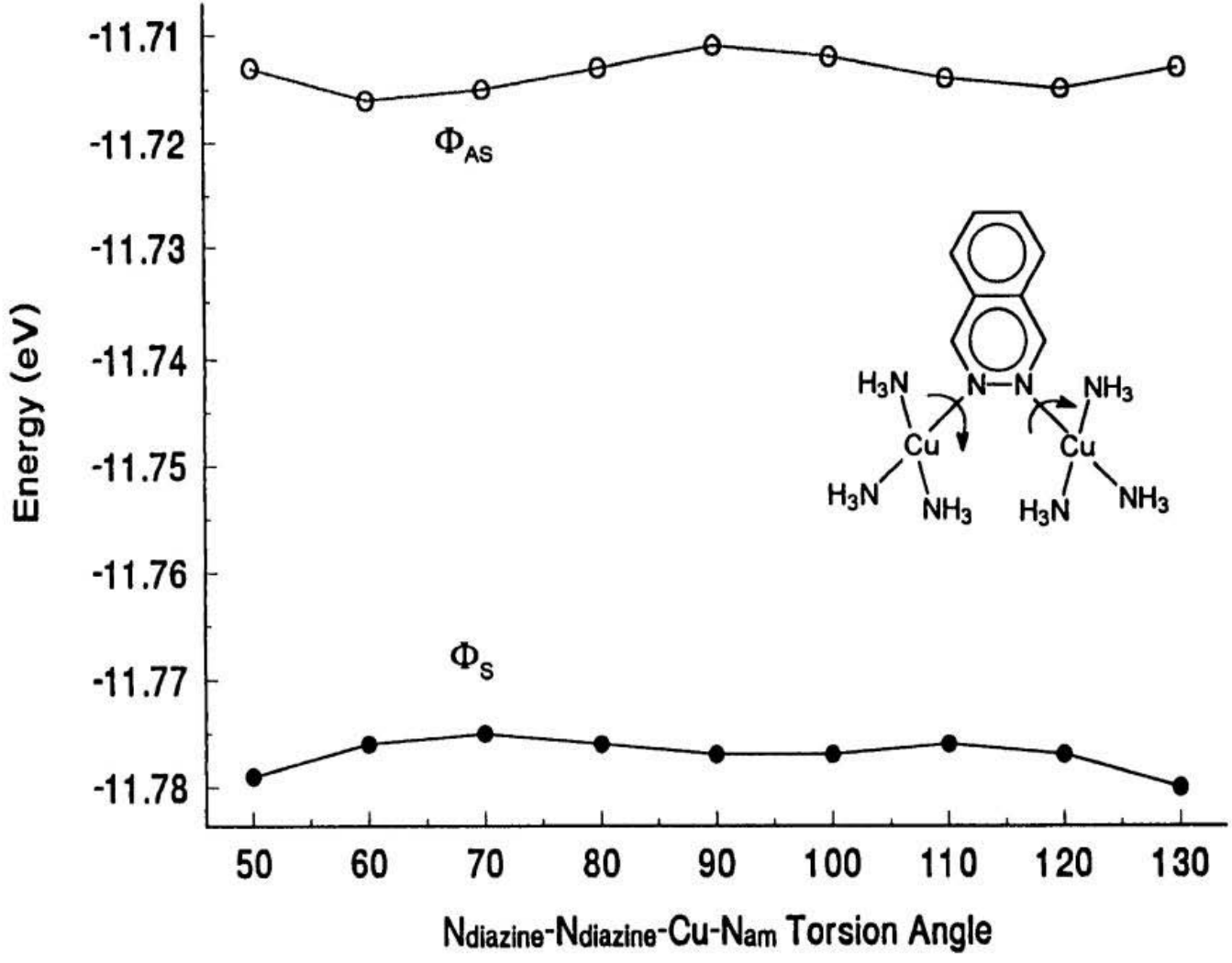

Fig. 4.23 Variation of Φ_s and Φ_{AS} Molecular Orbital Energies as a Function of $N_{diazine}$-$N_{diazine}$-Cu-N_{ammine} Torsion Angle (EHMO Model II).

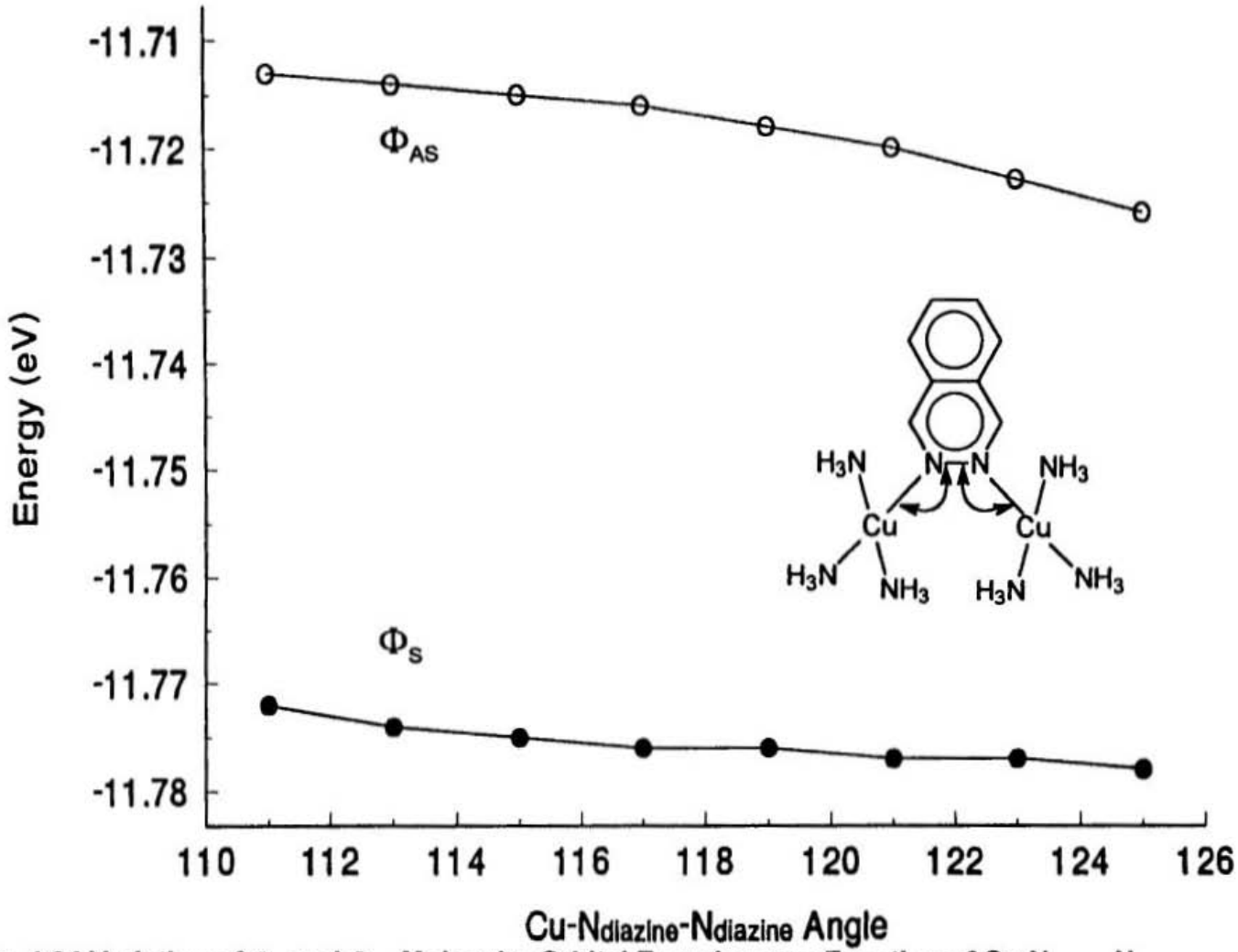

Fig. 4.24 Variation of Φ_s and Φ_{AS} Molecular Orbital Energies as a Function of Cu-$N_{diazine}$-$N_{diazine}$ Angle (EHMO Model III).

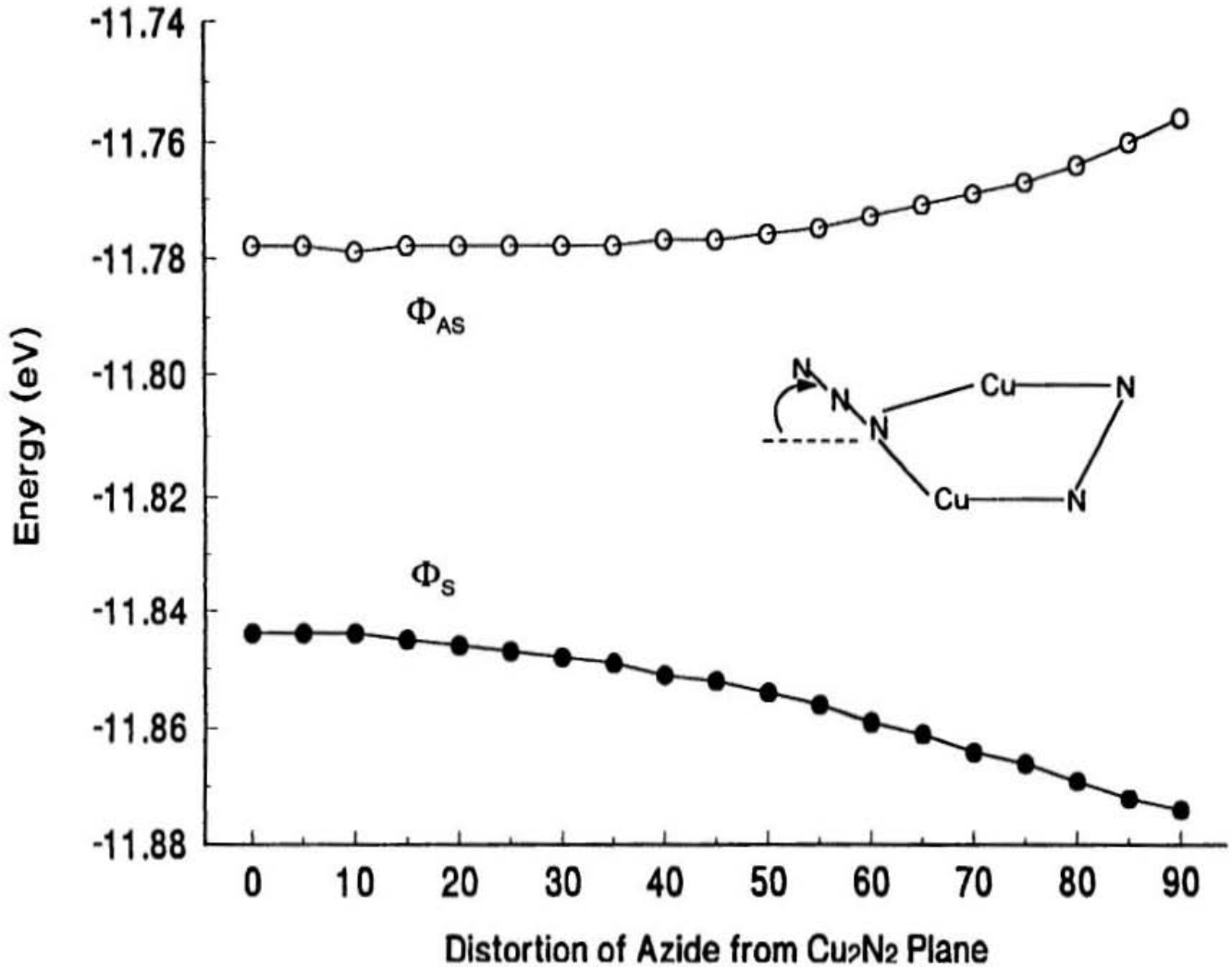

Fig. 4.25 Variation of Φ_s and Φ_{AS} Molecular Orbital Energies as a Function of Trigonal Distortion of the Bridging Azide Out of the $Cu_2N(diazine)_2$ Plane (EHMO Model IV).

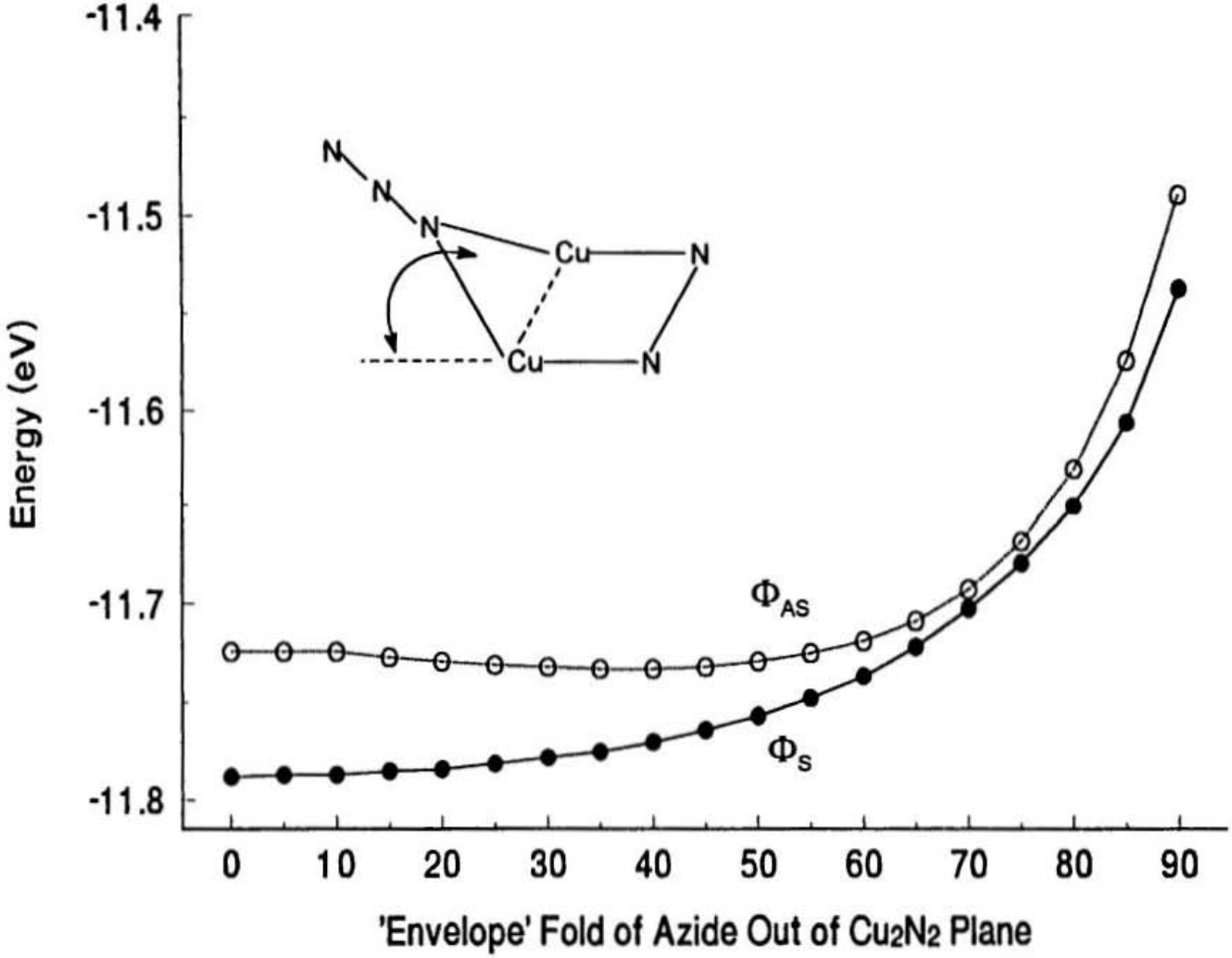

Fig. 4.26 Variation of Φ_s and Φ_{AS} Molecular Orbital Energies as a Function of the Bridging Azide Fold Out of the $Cu_2N(diazine)_2$ Plane, Along the Cu-Cu Axis (EHMO Model V).

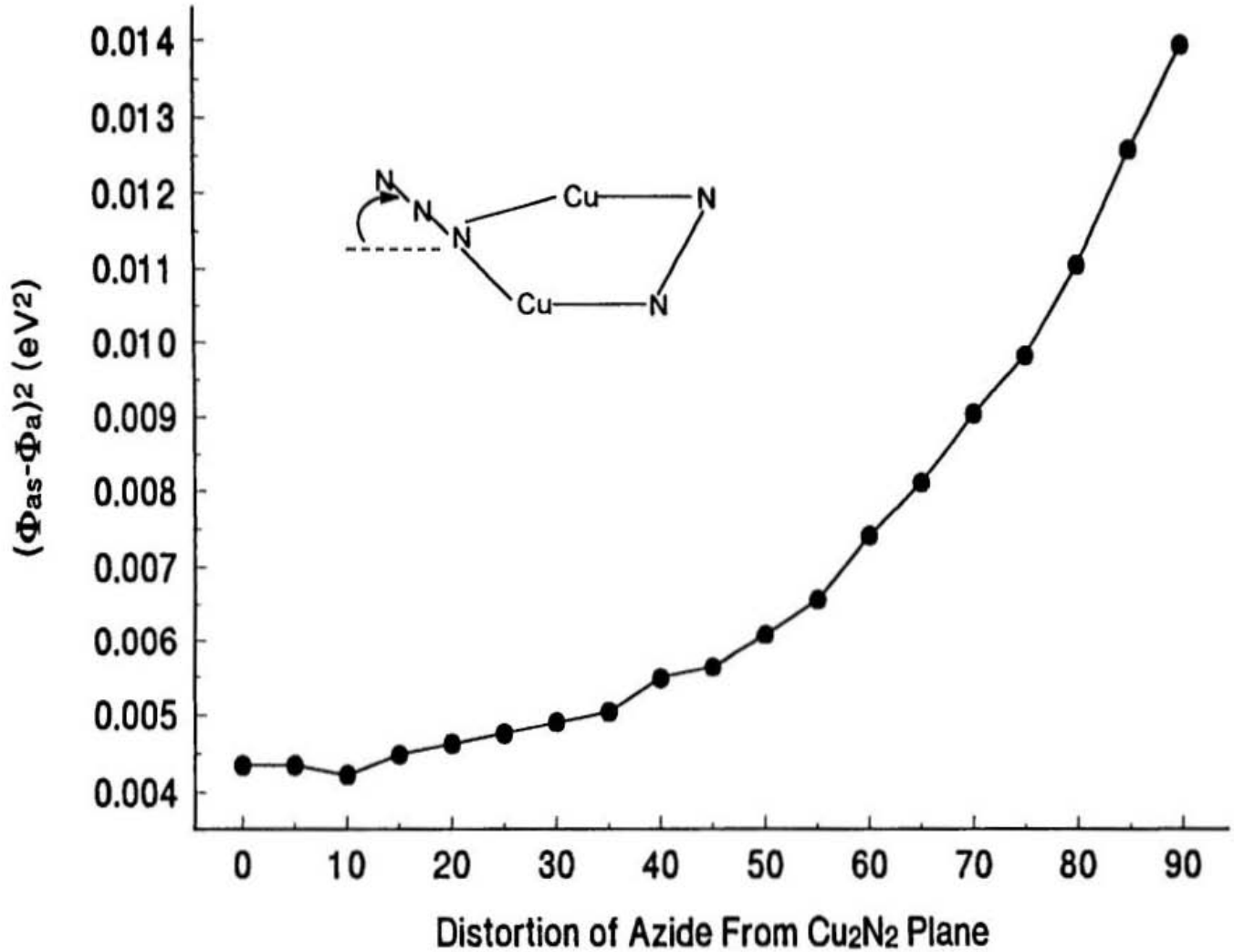

Fig. 4.27 Variation of the Square of the Φ_s and Φ_{As} Energy Gap as a Function of Trigonal Distortion of the Bridging Azide Out of the Cu_2N(diazine)$_2$ Plane (EHMO Model IV).

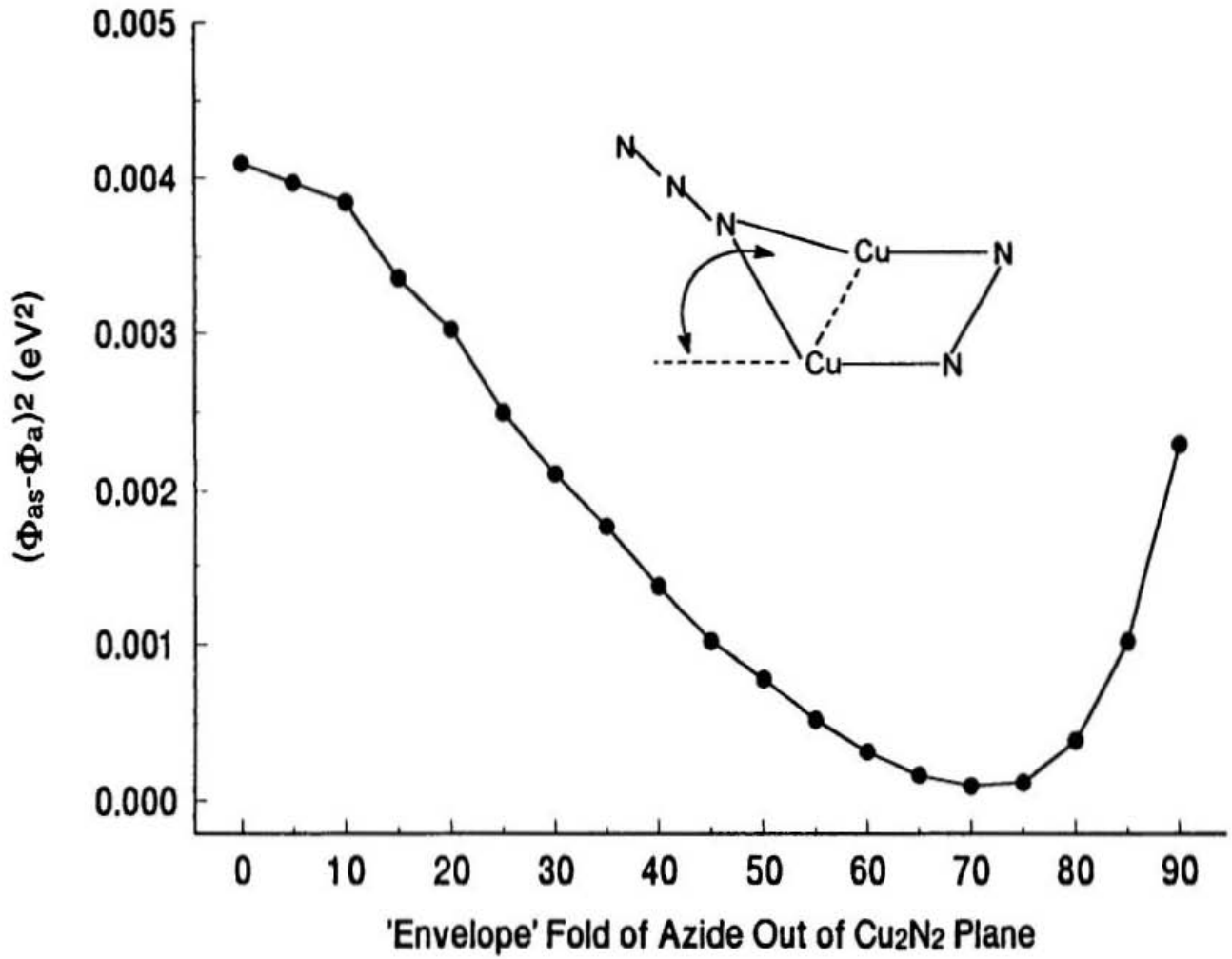

Fig. 4.28 Variation of the Square of the Φ_s and Φ_{AS} Energy Gap as a Function of the Bridging Azide Fold Out of the $Cu_2N(diazine)_2$ Plane, Along the Cu-Cu Axis (EHMO Model V).

Φ_{AS} does approach Φ_S, it then curves away, such that no crossover is observed. While at first this appears to present a contradiction to the observed magnetic properties of μ_2-1,1 azide / diazine systems, closer examination reveals problems with the chosen model. Keeping the five membered chelate ring flat creates distortions in other ring angles as the azide bridge angle is changed. In particular, the N-Cu-N angles are varying significantly from the ideal square planar geometry of 90°, as illustrated in Table 4.15. Since this is also changing the orbital overlap of the Cu(II) centres with the magnetic bridges, clearly there are too many parameters changing at the same time to isolate cause and effect relationships for the individual geometric distortions. The planar ring model is therefore a poor choice for investigating the behaviour of the μ_2-1,1 azide bridge in combination with a second diazine bridge.

The other model studies were attempts to investigate the various geometric changes individually and independently. Calculations **II** and **III** were carried out to investigate changes in coupling through the diazine bridge. Twisting the $Cu(NH_3)_3$ moieties in **II** serves two purposes: firstly, the two Cu(II) centres in Cu(II) / PAPR complexes are always twisted from coplanar, as can be seen in the angles between the Cu(II) least squares planes from the X-ray crystallographic data for **1** - **3** and **6**. Secondly, it is impossible to use two coplanar Cu(II) centres in model complex **M2** due to overlap between the ammonia groups. EHMO calculation **II** was performed to ensure twisting of the

planes will not interfere with the observation of possible coupling changes in other models in which this distortion proved necessary. As is seen in Fig.4.23, this is the case, with an essentially constant energy gap between Φ_S and Φ_{AS}.

Calculation **III** shows a gradual decrease in the energy gap at the upper angles investigated. Experimental data for Cu(II) / PAP3Me azide complexes, however, show that the Cu-$N_{diazine}$-$N_{diazine}$ angle is always <120°, below which angle the energy difference is essentially constant. The assumption that the diazine contribution to the antiferromagnetic coupling in Cu(II) / PAPR complexes is essentially constant appears to be consistent with these molecular orbital calculations. This is in contrast to Escuer et al.[119] in which an EHMO study of binuclear complexes linked by two pyridazine bridges showed maximum coupling at an M-N-N angle of 135°. This discrepancy is likely due to the fact that the N-Cu-N angle had to also be varied in the dibridged model, and as was shown in **I** this can also have an effect on the J_{AF}. In fact, at M-N-N =135°, the N-Cu-N angle was 90°, the angle of optimal overlap with the $d_{x^2-y^2}$ Cu(II) orbital.

In contrast, calculations **IV-V** involving distortion at the bridging azide show significant dependence of the antiferromagnetic coupling on the distortion angle, as illustrated in Fig.4.25 and Fig.4.26. For the trigonal distortion in **IV**, the energy difference (Φ_{AS} -Φ_S) is essentially constant at small angles. As the distortion increases, however, the energy difference increases to a maximum at 90°. The plot of $(\varepsilon_{AS}-\varepsilon_S)^2$ versus trigonal distortion angle in Fig.4.27 suggests then

that J_{AF} will increase with increasing angle. In contrast, calculation **V** (Fig.4.26) shows a decrease in the energy difference as the fold angle increases. This in turn implies a decrease in J_{AF} as the angle increases, as illustrated in the

Table 4.16 Experimental Azide Distortions.

	Trigonal Distortion	Fold Angle
1	358.1° (50K) to 359.1° (290K)	58.39(19)° (50K) to 57.5(2)° (290K)
2	353.4°	57.7(7)°
3	342.3°	61.7°

$(\varepsilon_{AS}-\varepsilon_{S})^2$ versus fold angle plot in Fig.4.28. Note that the results at higher angles (> ~75°) are not reliable due to distortions which begin to occur in the Cu(II) coordination geometry. It is apparent, however, from Fig.4.28 that a minimum J_{AF} should be expected at a fold angle of ~70°.

The question which now arises is how do the EHMO results compare to the observed azide distortions in complexes **1** - **3**. Relevent experimental data are given in Table 4.16. For trigonal distortion, the quoted angles are the sum of the angles around the bridging nitrogen of the μ_2-1,1 azide. If the azide is planar, this value should be 360°. As can be seen, for **1** this value is very close to 360°, indicating no distortion in this complex. For **2** and **3**, slightly larger distortions are observed. They are not likely to be large enough to have any significant influence, however, since the distortion has to be relatively large before there is any noticeable change in $(\varepsilon_{AS}-\varepsilon_{S})^2$ and hence J_{AF}. The azide fold angle along the

Cu-Cu axis, however, appears to be more significant. For all three complexes, the fold is ~60°, which lies near the minimum in the $(\varepsilon_{AS}-\varepsilon_{S})^2$ versus angle plot. This implies that the observed coupling for **1** - **3** is less than that in similar complexes with a planar azide structure. Unfortunately, no planar μ_2-1,1 azide / diazine complexes with comparable angles are known, so experimental confirmation of this hypothesis is not possible.

The final question concerns whether these results can offer a possible explanation for the unusual magnetic properties observed for **1** - **3**. Unfortunatelly, this appears not to be the case. Regardless of any variation in the observed coupling which occurs due to geometric changes in a complex, the data should still fit the Bleaney-Bowers equation. This is supported by the observation that other μ_2-1,1 azide / diazine complexes[58,59] with similar distortions to those examined here (apart from larger μ_2-1,1 azide bridge angles) are found to fit quite well to the Bleaney-Bowers equation.

4.6 Conclusions

The magnetostructural chemistry of a series of coordination complexes derived from Cu(II) and the ligand 1,4-bis(3'-methyl-2'-pyridyl)aminophthalazine (PAP3Me) has been presented. From the same basic Cu_2PAP3Me binuclear core, a series of quite structurally distinct and intriguing structures are formed. The complexes **1** - **3** are illustrative examples of the diversity of the coordination

modes of the azide ligand. These complexes include examples of simple binuclear μ_2-1,1 azide systems (**3**), tetranuclear complexes consisting of two binuclear units linked via μ_2-1,3 azide bridges (**1,2**), and a one dimensional chain via μ_2-1,3 azide bridges, which simultaneously act as μ_2-1,1 azide bridges (**1**). The non-azide complex **6** is meanwhile notable for the unusual μ_2-O-SO_3 bridges, an almost unprecedented bonding mode for the sulfate ligand.

The magnetic properties of the azide complexes **1** - **5** prove to be anomalous in comparison to previously studied Cu(II) diazine / μ_2-1,1 azide bridged complexes. At large μ_2-1,1 bridge angles, antiferromagnetic coupling is observed, while at small angles ferromagnetic coupling predominates. The complexes presented here have intermediate angles, around the critical angle where the magnetic properties change in sign, and it is found that such systems **do not** fit the Bleaney-Bowers equation for magnetic exchange in binuclear Cu(II) complexes. Several models were used in attempts to fit the magnetic data, and while the causes of this anomaly are uncertain, the data fits best if a variable temperature coupling constant is used. Variable temperature X-ray crystallographic studies were carried out to determine if the variable temperature -2J can be rationalised in terms of changing bridge geometry, but the results indicate that this is not the case. The non-azide complexes **6** - **9** exhibit magnetic coupling typical for binuclear Cu(II) systems. Of particular interest are complexes **6** and **7**. The magnetic coupling in both of these is essentially identical, and

coupling occurs via just the phthalazine diazine bridge. This observation supports the assumption made in the azide bridged complexes that the contribution of the diazine to the overall antiferromagnetic coupling is essentially constant.

An Extended Hückel molecular orbital study was undertaken to further explore the factors which affect the magnitude of magnetic exchange in antiferromagnetic μ_2-1,1 azide systems. It was found that in addition to changes in the angle at the azide bridge, deviation of the azide from the Cu-diazine plane also plays a role in determining the magnitude of the antiferromagnetic component of the exchange.

Chapter 5. Ni(II) and Mn(II) Complexes of the Ligand PHP6Me

5.1 Synthesis of the Ligand and Complexes

The ligand 1,4-bis((6-methylpyridine-2-carboxaldiimino)amino)phthalazine (PHP6Me) was prepared using the literature procedure[86,120] by reaction of 2-acetylpyridine and 1,4-dihydrazinophthalazine[121] in refluxing methanol.

$[Ni_2(PHP6Me\text{-}H)(N_3)_3(CH_3OH)]$ (10)

$Ni(BF_4)_2 \cdot 6H_2O$ (0.340g, 1.00mmol) and PHP6Me (0.200g, 0.500mmol) were dissolved in refluxing CH_3OH (50mL) to give a dark red solution. Subsequent addition of a solution of NaN_3 (0.160g, 2.50mmol) in H_2O (10mL) resulted in no visible change. After refluxing 3 hours, the solution was filtered and left to cool, yielding a dark red-brown powder after several days. This was filtered off and washed with CH_3OH. Yield: 0.250g (75%). Anal. Calc'd for $[Ni_2(C_{22}H_{19}N_8)(N_3)_3(CH_3OH)]$, C: 41.17 H: 3.46 N: 35.49; Found, C: 40.85, H: 3.10, N: 35.30.

$[Ni_2(PHP6Me\text{-}H)(N_3)_3(H_2O)_{3.5}(CH_3CH_2OH)_{0.5}]$ (11)

A solution of $Ni(BF_4)_2 \cdot 6H_2O$ (0.172g, 0.505mmol) in hot H_2O (15mL) was added to a solution of PHP6Me (0.100g, 0.252mmol) in hot CH_3CH_2OH (100mL) to give a burgundy solution. Subsequent addition of a solution of NaN_3 (0.062g, 1.00mmol) in hot H_2O (5mL) gave a darker burgundy solution. This was heated

for a few minutes, and then filtered. After several days, a dark red microcrystalline product formed, which was filtered off and washed with cold CH_3CH_2OH. Yield: 0.065g (36%). Calc'd for $[Ni_2(C_{22}H_{19}N_8)(N_3)_3(H_2O)_{3.5}(CH_3CH_2OH)_{0.5}]$, C: 38.10, H: 4.04, N: 32.85; Found, C: 38.20, H: 3.86, N: 33.21.

$[Ni_2(PHP6Me\text{-}2H)(N_3)_2(H_2O)_2(CH_3OH)_2]$ (12)

A solution of $Ni(BF_4)_2 \cdot 6H_2O$ (0.128g, 0.376mmol) in hot H_2O (10mL) and a solution of NaN_3 (0.024g, 0.370mmol) in hot H_2O (10mL) were added to a solution of PHP6Me (0.075g, 0.190mmol) in hot CH_3OH (30mL) to give a dark red solution. Subsequent addition of a solution of triethylamine (0.100g, 1.00mmol) in CH_3OH (5mL) gave a dark purple solution. This was heated for a few minutes, and then left to cool. After several days, a dark purple powder formed, which was filtered off and washed with cold CH_3OH. Yield: 0.070g (54%). Anal Calc'd for $[Ni_2(C_{22}H_{18}N_8)(N_3)_2(H_2O)_2(CH_3OH)_2]$, C: 41.41, H: 4.35, N: 28.18; Found. C: 41.07, H: 3.42, N: 28.00.

$[Ni_2(PHP6Me\text{-}H)(N_3)_3(CH_3OH)_2]$ (13)

A solution of NaN_3 (0.048g, 0.738mmol) in CH_3OH (10mL) was added to a solution of $[Ni_2(PHP6Me)Cl(H_2O)_4]Cl_3(H_2O)_4$[86] (0.107g, 0.134mmol) in refluxing CH_3OH (60mL) to give a dark purple solution. After refluxing 3.5 hours, the solution was filtered and left to cool, yielding a very dark purple powder after

several hours. This was filtered off and washed with CH_3OH. Yield: 0.068g (72%). Anal. Calc'd for $[Ni_2(C_{22}H_{19}N_8)(N_3)_3(CH_3OH)_2]$, C: 40.99, H: 4.03, N: 33.87; Found, C: 40.86, H: 3.50, N: 33.77.

$[Ni_2(PHP6Me)Cl(NCS)_2(H_2O)(CH_3CH_2OH)][Ni_2(PHP6Me)Cl(NCS)(H_2O)]Cl_3$ (14)

A solution of KSCN (0.072g, 0.740mmol) in H_2O (2mL) was added to a solution of $[Ni_2(PHP6Me)Cl(H_2O)_4]Cl_3(H_2O)_4$[86] (0.150g, 0.188mmol) in refluxing CH_3CH_2OH (55mL) to give a dark orange solution. After refluxing for 2 hours, the solution was filtered hot and left to cool, yielding a red-orange microcrystalline product after several days. This was then filtered off and washed with cold CH_3CH_2OH. X-ray quality crystals were prepared by ether diffusion into a sample of the reaction solution diluted with CH_3CH_2OH. Yield: 0.050g (36%). Anal. Calc'd for $[Ni_2(C_{22}H_{20}N_8)Cl(NCS)_2(H_2O)(CH_3CH_2OH)][Ni_2(C_{22}H_{20}N_8)Cl(NCS)(H_2O)]Cl_3$, C: 40.26, H: 3.46, N: 18.21; Found, C: 39.65, H: 3.63, N: 18.10.

$[Mn_2(PHP6Me\text{-}H)(N_3)_3(H_2O)_{2.5}]$ (15)

$MnCl_2 \cdot 4H_2O$ (0.197g, 1.00mmol) and PHP6Me (0.200g, 0.500mmol) were dissolved in refluxing CH_3OH (60mL) to give a red solution. Subsequent addition of a solution of NaN_3 (0.132g, 2.00mmol) in H_2O (3mL) gave a darker red solution, which after refluxing 2 hours yielded an ochre red precipitate. This was filtered and washed with CH_3OH, then immediately transferred to a Schlenk tube,

dried under vacuum and stored under N_2. Yield: 0.150g (44%). Anal. Calc'd for $[Mn_2(C_{22}H_{19}N_8)(N_3)_3](H_2O)_{2.5}$, C: 39.00 H: 3.58 N: 35.15; Found, C: 39.12 H: 3.32 N: 35.02.

$[Mn_2(PHP6Me)(NCS)Cl_3(H_2O)]$ (16)

$MnCl_2 \cdot 4H_2O$ (0.098g, 0.500mmol) and PHP6Me (0.100g, 0.250mmol) were dissolved in refluxing CH_3CH_2OH (80mL) to give a red-orange solution. Subsequent addition of a solution of KSCN (0.100g, 1.00mmol) in H_2O (2mL) gave a slightly darker solution. After refluxing for 2 hours, the solution was filtered and left to cool. After several days, a red-orange microcrystalline product formed, which was filtered off and washed with cold CH_3CH_2OH. Yield: 0.040g (23%). Anal. Calc'd for $[Mn_2(C_{22}H_{20}N_8)(NCS)Cl_3(H_2O)]$, C: 40.10, H: 3.23, N: 18.31; Found, C: 40.00, H: 3.65, N: 18.56.

5.2 Spectroscopy and Structure

Relevent infrared spectroscopic data for complexes **10** - **16** are given in Table 5.1. One notable feature of complexes of the PHP6Me ligand is the ease with which the ligand can be deprotonated at the exocyclic NH sites. PHP6Me and the related ligand APHP (APHP = 1,4-bis((pyrid-2-ylacetaldiimino)amino) phthalazine) form Cu(II) complexes in which the ligand can be monodeprotonated by simply carrying out the reaction in dilute alcoholic solution,

Table 5.1 Infrared Spectral Data for Ni(II) / PHP6Me and Mn(II) / PHP6Me Azide and Thiocyanate Complexes.

Complex	IR, cm^{-1}		
	N_3^- (ν_3 Stretch) OR NCS^- (C≡N Stretch)	C=N Stretch	Pyridine Ring Breathing
$[Ni_2(PHP6Me\text{-}H)(N_3)_3(CH_3OH)]$ **(10)**	2073 2033	1618, 1602 1562, 1556 1530,1495	1004[b]
$[Ni_2(PHP6Me\text{-}H)(N_3)_3(H_2O)_{3.5}(CH_3CH_2OH)]$ **(11)**	2074 2034	1617, 1602 1562, 1555 1530, 1497	1002[b]
$[Ni_2(PHP6Me\text{-}2H)(N_3)_2(H_2O)_2(CH_3OH)_2]$ **(12)**	2062 2033 2020	1597, 1548 1498	1038[b]
$[Ni_2(PHP6Me\text{-}H)(N_3)_3(CH_3OH)_2]$ **(13)**	2072 2031 2020	1611, 1602 1556, 1526 1489	1004[b]
$[Ni_2(PHP6Me)Cl(NCS)_2(H_2O)(CH_3CH_2OH)]$ $[Ni_2(PHP6Me)Cl(NCS)(H_2O)_2]Cl_3$ **(14)**	2097 2045	1623, 1599 1591, 1565 1525	1004
$[Mn_2(PHP6Me\text{-}H)(N_3)_3](H_2O)_{2.5}$ **(15)**	2109, 2083 2060 [2034][a]	1618, 1596 1560, 1543 1529, 1493	1008
$[Mn_2(PHP6Me)(NCS)Cl_3(H_2O)]$ **(16)**	2066 [2048] [2036]	1614, 1595 1573, 1563 1525	1004

[a] [] indicates a shoulder.
[b] very weak bands.

Table 5.2 Electronic Spectral Data for Ni(II) / PHP6Me Azide and Thiocyanate Complexes.

Complex	λ_{max}, nm (ε, $M^{-1}cm^{-1}$)		
	ν_1	ν_2	CT Bands
$[Ni_2(PHP6Me\text{-}H)(N_3)_3(CH_3OH)]$	[940][a,b] (220)	640 (5900)	310 (5800), 340 (5900) [390] (4550, 525 (4300)
(10)	950[c]	[675]	330, 535
$[Ni_2(PHP6Me\text{-}H)(N_3)_3(H_2O)_{3.5}(CH_3CH_2OH)]$ **(11)**	950 (300)	610 (5000) 630 (5000)	310 (5500), 335 (5700) [390] (4550), [485] (3200) 530 (3650)
	980, [860]	[640]	330, 530
$[Ni_2(PHP6Me\text{-}2H))(N_3)_2(H_2O)_2(CH_3OH)_2]$ **(12)**	[950] (110)	635 (7800) 605 (8000)	310 (7100), 340 (8200) [390] (6700), [480] (3350) [525] (4600)
	1020	715	345, [550]
$[Ni_2(PHP6Me\text{-}H)(N_3)_3(CH_3OH)_2]$	[970] (90)	600 (6800) 640 (7100)	310 (11500), 340 (10500) [390] (6700), 525 (8500)
(13)	940	[640]	335, 520
$[Ni_2(PHP6Me)Cl(NCS)_2(H_2O)(CH_3CH_2OH)][Ni_2(PHP6Me)Cl(NCS)(H_2O)_2]Cl_3$	†	†	310 (12200), 410 (8300) [425](6950), 510 (2500) [525] (2500)
(14)	1010	[610]	310, 425, 515

[a] [] indicates a shoulder.
[b] DMF solution spectrum
[c] mull spectum.
† bands not observed.

whereas removal of both protons requires the use of base, such as triethylamine.[122] For Ni(II) and Co(II), however, complexes of the neutral ligand are usually formed.[86] Note, however, that the Ni(II) / azide complexes **10 - 13** and the Mn(II) / azide complex **15**, all contain the monodeprotonated ligand (except for **12**, in which both protons are removed by addition of triethylamine) while the thiocyanate complexes **14** and **16** contain the neutral ligand. This is a function of the basicity of the azide and thiocyanate ions: the azide ion is a stronger base than the thiocyanate ion,[123] such that while azide is able to deprotonate the ligand, thiocyanate is not.

Table 5.3 Electronic Spectral Data for Mn(II) / PHP6Me Azide and Thiocyanate Complexes.

Complex	λ_{max}, nm (ε, M^{-1} cm^{-1})	
	Mull	**Solution**
$[Mn_2(PHP6Me\text{-}H)(N_3)_3](H_2O)_{2.5}$ **(15)**	310, [435][a] 540 880, [1000]	†
$[Mn_2(PHP6Me)(NCS)Cl_3(H_2O)]$ **(16)**	325, 435 [530]	310 (10800) 420 (10200) [520] (580)

[a] [] indicates a shoulder.
† solubility in DMF too low to obtain spectrum.

Although the presence of a mono- or dianionic ligand can usually be determined from the elemental analysis data, the C=N stretching region of the PHP6Me ligand is also characteristic for the three types of ligand: neutral, monoanionic and dianionic. This is based on the number of bands, as well as the

energy of the highest and lowest lying bands. The criteria are outlined in Table 5.4. Examing the data for complexes **10 - 16**, it is observed that the analytical data are indeed in good agreement with the C=N infrared data.

Table 5.4 Criteria For Determining Charge on the Ligand PHP6Me, Based on the Ligand C=N Stretching Bands.

	Number of Bands	Highest Band (cm^{-1})	Lowest Band (cm^{-1})
Neutral	Five or Six	> 1600	~ 1525
Monoanionic	Five or Six	> 1600	< 1500
Dianionic	Three or Four	~ 1600	< 1500

For the azide complexes **10 - 13** and **15**, the criteria for assigning bonding modes based on the frequency of the antisymmetric stretch is the same as that for the Cu(II) complexes, as discussed in Chapter 4. The higher frequency band can be associated with the μ_2-1,1 bridge, and other bands with μ_2-1,3 or terminal azides. For **10 - 13** and **15**, the highest frequency band lies between 2109 cm^{-1} and 2062 cm^{-1}, in the range typically observed for μ_2-1,1 azide. All of the complexes also exhibit either one (**10 - 11**), two (**12 - 13**), or three (**15**) other bands. As previously noted, the presence of more than one azide band in this region can be interpreted in one of two ways, indicating either the presence of more than one azide bonding mode, or the presence of asymmetry in the binuclear centre. Without X-ray structural data for any of the complexes to use

as a comparison, it is difficult to determine what causes the splitting of the azide band in these particular complexes.

Determining the bonding mode of thiocyanate should be further complicated, in comparison to azide, since thiocyanate is an ambidenate ligand and can bond via either the sulfur or the nitrogen. However, the first row transition series generally forms N-bonded complexes in preference to S-bonded. With this in mind, we need mostly be concerned with three types of bonding: N-terminal, μ_2(N)-1,1 and μ_2(N,S)-1,3, which are analogous to the three azide bonding types. The relative frequencies of the different bonding modes are inverted, however, in comparison to azide. The μ_2(N)-1,1 thiocyanate is found at lower frequency (2030-2000 cm^{-1}) than μ_2(N,S)-1,3 thiocyanate (>2100 cm^{-1}), while N-terminal thiocyanate usually falls somewhere in between. Based on these criteria, it would appear that attempts to prepare μ_2(N)-1,1 bridged thiocyanate complexes were unsuccessful, since the ν(C≡N) bands for **14** and **16** lie above 2030 cm^{-1}. This is supported by a preliminary crystal structure of **14** (Fig.5.1), which shows that the Ni(II) centres are bridged by the phthalazine diazine and chloride, with N-terminal thiocyanate ligands. The asymmetric unit contains two different binuclear units, which may be responsible the presence of two thiocyanate bands in the infrared (2097 cm^{-1} and 2045 cm^{-1}).

Similar to PAP3Me, the ligand PHP6Me can be considered essentially as a substituted pyridine, and so the pyridine ring breathing band can be used to

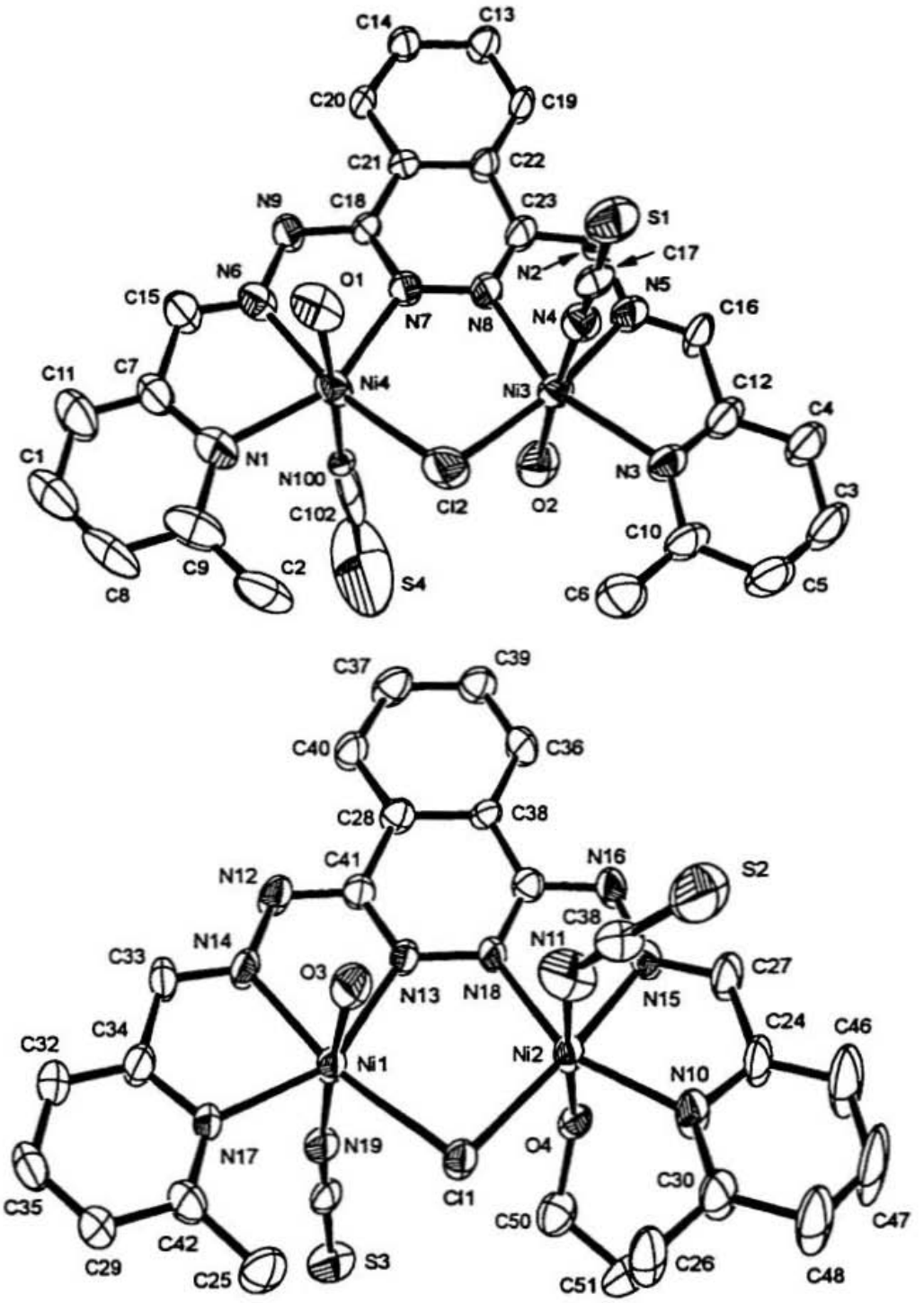

Fig. 5.1 Preliminary Structural Representation of $[Ni_2(PHP6Me)Cl(NCS)_2(H_2O)(CH_3CH_2OH)][Ni_2(PHP6Me)Cl(NCS)(H_2O)_2]Cl_3$ (14) (50% Probability Ellipsoids).

indicate coordination of the pyridine moiety. In the free PHP6Me ligand, this band occurs at 993 cm^{-1}. For the Ni(II) / thiocyanate complex **14** and the Mn(II) complexes **15 - 16**, this band can is clearly observed in the range 1004-1008 cm^{-1}, indicating coordination of the pyridine moieties. For the Ni(II) / azide complexes **10 - 14**, however, the band is apparently very weak, and not as easily observed. Even considering this, assignment of the weak bands shown in Table 5.1 to this ring breathing is reasonable. The fact that a band is observed at about the right energy, and the absence of a band around 993 cm^{-1} which would indicate free pyridine moieties, would appear to support coordination of both pyridines. In addition, all other reported structures of complexes of PHP6Me[86,122] are shown to have coordination of both pyridine moieties.

The electronic spectra of the Ni(II) complexes **10 - 14** are recorded in Table 5.2, while the spectra of the Mn(II) complexes **15 - 16** are recorded in Table 5.3. The spectrum of the free ligand in DMF shows two $\pi \rightarrow \pi^*$ bands at 310nm (20700 $M^{-1}cm^{-1}$) and 425nm (22700 $M^{-1}cm^{-1}$). All of the complexes show intense (ε = 2500 - 12200 $M^{-1}cm^{-1}$), multiple charge transfer bands in the range 300-550nm, along with weaker d-d bands in the visible region in most cases.

Consider first the Mn(II) complexes **15 - 16**. High spin octahedral Mn(II) is a d^5 ion and has a ^6S ground term, which is not split by a crystal field. As a result, all d-d transitions are spin forbidden and the d-d region of the electronic spectrum should exhibit, at best, very weak bands. In fact, it is rarely possible to

observe d-d transitions in Mn(II) complexes with organic ligands since the weak tail of ligand absorption into the visible region is usually enough to mask the bands.[111] That being said, two bands are observed in the visible region in complex **15**, at 880nm and 1000nm. There are two possible explanations for this anomaly. Firstly, **15** is unstable in air, decomposing over a period of days to give a dark green-brown product. This is most likely the result of oxidation from a Mn(II) to a Mn(III) species. The presence of some Mn(III) decomposition product could be responsible for the d-d visible region bands, which for Mn(III) are often fairly intense.[111] The decomposition product of **15** does show two fairly intense bands in the mull transmittance spectrum at 820nm and 985nm. Secondly, the bands may be Mn(II) d-d bands, unusually intense due to distortions from octahedral geometry and / or intensity stealing from the higher energy charge transfer states.

That aside, the only bands normally expected in the spectra of the Mn(II) / PHP6Me complexes would be charge transfer bands. The Mn(II) / thiocyanate complex **16** has three bands between 325nm and 530nm in the mull transmittance spectrum, and similar bands in the DMF solution spectrum, while the Mn(II) / azide complex **15** mull transmittance spectrum exhibits three similar bands in the same region. Comparing these to the bands observed in the free ligand, the two lowest wavelength bands are clearly $\pi \rightarrow \pi^*$ PHP6Me bands, while the highest wavelength bands can be associated with some metal / ligand

charge transfer process. The ligand PHP6Me is an unsaturated derivative with relatively low energy π^* antibonding orbitals, so it can reasonably be assumed that these bands are metal→ligand in nature. Although no electrochemical data are available for the complexes reported here, positive oxidation potential (vs. SCE in DMF) have been observed for Cu(II) derivatives of the related ligand APHP (Cu(II)→Cu(III)) indicating the oxidizable nature of the Cu(II) centre, and supporting the metal→ligand origin of the charge transfer transitions.[120]

The spectra of the Ni(II) complexes are somewhat more complicated than the Mn(II) derivatives. The octahedral d^8 Ni(II) ion has a $^3A_{2g}$ ground state, and exhibits three characteristic d-d bands in the visible region: ν_1 ($^3T_{2g} \leftarrow {}^3A_{2g}$) in the range 1400-770nm, ν_2 ($^3T_{1g} \leftarrow {}^3A_{2g}$) in the range 900-500nm, and ν_3 ($^3T_{1g}(P) \leftarrow {}^3A_{2g}$) in the range 525-370nm.[111] It is immediately obvious that the ν_3 band will be masked in complexes **10 - 14** by the intense charge transfer bands in the same region. The other two bands are observed, however, as shown in Table 5.2. The only exception is the thiocyanate complex **14**: no d-d bands are observed in the DMF spectrum, due to high dilution of the solution. These bands are observed in the mull transmittance spectrum, however. It should also be noted that for several complexes (**11 - 13**), the ν_2 band is split into two components. This is a result of mixing between ν_2 and the spin forbidden transition ($^1E_g \leftarrow {}^3A_{2g}$), which often occurs in less than ideal octahedral symmetry. In addition, the ν_2 band is much more intense than the ν_1, which is atypical for Ni(II) systems. This arises

from intensity stealing, in which the d-d bands increase in intensity by coupling with charge transfer bands of similar energy. The ν_1 band in **11** is also split, a phenomenon frequently observed as the symmetry goes from octahedral to D_{4h}. This lower symmetry state has two transitions ($^3B_{2g} \leftarrow {}^3A_{2g}$ and $^3E_{gg} \leftarrow {}^3A_{2g}$) in this region, as opposed to just one for octahedral symmetry.

The charge transfer spectra of **10 - 14** are in general agreement with that observed for the Mn(II) complexes, with some minor differences. The mull transmittance spectra of complexes **10 - 13** show two rather than three bands, undoubtedly due to overlap between two broad charge transfer bands of similar energy. The solution spectra, on the other hand, give the opposite variation. Instead of three bands, four or five are observed. The reasons for this are not clear, but may be due to changes in the chromophore as a function of the strongly coordinating DMF solvent.

Assigning structures to the Ni(II) and Mn(II) complexes of PHP6Me proves to be a much more challenging exercise than for the Cu(II) / PAP3Me complexes. This is partly due to a lack of X-ray crystal structures which can be utilised as a 'standard', allowing correlation of spectroscopic data with structural features which can then be extended to other complexes for which no structures are available. The greater tendency, as compared to Cu(II), of Ni(II) and Mn(II) to form extended polymeric systems with azide also presents a problem, as it is

difficult on the basis of spectroscopic and analytical data alone to tell if one is dealing with a simple binuclear system or extended networks.

These considerations aside, some useful deductions can be made on the basis of both the analytical and spectroscopic data, as well as comparison with other complexes of the ligand PHP6Me. It is apparent that the basic structure is a binuclear moiety, bridged by the phthalazine diazine and a second exogenous bridge. For the azide complexes **10** - **13** and **15**, based on the infrared data, this bridge is obviously a μ_2-1,1 azide. Also note that **10** and **11** are nearly identical spectroscopically, and would appear to contain structurally similar binuclear units. For the thiocyanate complex **14**, the bridge is chloride, as shown in the preliminary X-ray structure. Since the Mn(II) / thiocyanate complex **16** is very similar spectroscopically to **14**, it is reasonable to assume a similar binuclear chloride bridged, terminal N-thiocyanate structure for it. Whether the azide complexes are simple binuclear structures or more complex extended systems is difficult to tell based on the available data, however. Even the magnetic data (*vide supra*) are ambiguous, such that they cannot to used to help determine the nature of the azide complexes.

There is a further note concerning the preliminary structure of **14**. The analytical data agree with this structure, except on one point. The X-ray structure, as shown in Fig.5.1, has a fourth N-terminal thiocyanate (N(110)-C(102)-S(4)) not observed in the elemental analysis. The highly

distorted thermal ellipsoids suggest that this is a poor choice to model the observed peaks. However, neither S-terminal thiocyanate or ethanol solvent, the other most likely possibilities, gave any better refinement. It is difficult even to determine whether it is thiocyanate on the basis of charge balancing, since it proved difficult to unambiguously determine the number and position of the chloride counterions in the lattice. The structure of **14** reported here is, however, sufficient as a guide to the structure of both **14** and the related complex **16**.

5.3 Magnetism

The magnetic data for the Ni(II) and Mn(II) complexes are reported in Table 5.5 and Table 5.6, respectively. The room temperature magnetic moments were calculated using equation (5.1), where μ_{eff} is the effective magnetic moment

$$\mu_{eff} = 2.828(T^{*}(\chi_{M} - TIP))^{1/2} \qquad (5.1)$$

in Bohr magnetons (BM) and the other symbols have their usual meanings. Standard TIP values of 100 x 10^{-6} emu/mol (Ni(II)) and 0 x 10^{-6} emu/mol (Mn(II)) were used for these calculations. For an isolated octahedral Ni(II) system, μ_{eff} generally lies in the range 2.9 - 3.3 BM.[18] The values reported in Table 5.5 for complexes **10** - **14**, lie slightly below this range, with the exception of **11**. This suggests that these are antiferromagnetically coupled systems, although with the exception of **13**, the μ_{eff} values do not differ significantly enough from the values for an isolated system to draw any definite conclusions. Complex **13** is obviously

Table 5.5 Variable Temperature Magnetic Parameters for Complexes (10)-(14), Data Fitted to Ginsberg Equation.†

	μ_{eff} (BM)	J (cm^{-1})	g	Z'J'	D (cm^{-1})	ρ	10^2R
(10)	2.81	-21.9(5)	2.02(1)	0.001	2	0.12	2.6
(11)	3.04	-	-	-	-	-	-
(12)	2.73	-	-	-	-	-	-
(13)	2.45	-75.0(1)	2.19(1)	0.001	12	0.05	1.33
(14)	2.84	-10.0(1)	2.09(1)	0.0133	3.77	0	1.51

† of the form:

$$\chi_M = \chi(g,J,D,Z'J')(1-\rho) + \left(\frac{2g^2N\beta^2}{3kT}\right)\rho + N\alpha$$

Where J = exchange integral
g = Landé splitting facter
D = zero field splitting
Z' = dimer lattice coordination number
J' = interdimer exchange integral
ρ = fraction of paramagnetic impurity
Nα = temperature independant paramagnetism
$R = [\Sigma(\chi_{obs} - \chi_{calc})^2 / \Sigma\chi_{obs}^2]^{1/2}$

Table 5.6 Variable Temperature Magnetic Parameters for Complexes (15)-(16), Data Fitted to the Mn(II) Equation.†

	μ_{eff} (BM)	J (cm^{-1})	g	ρ	TIP ($*10^6$)	θ (K)	10^2R
(15)	5.58	-4.1(2)	2.00(1)	0.03	5	2	2.06
(16)	5.55	-	-	-	-	-	-

† $\chi_m = \left[\frac{Ng^2\beta^2}{k(T-\theta)}\left(\frac{55+30e^{10x}+14e^{18x}+5e^{24x}+e^{28x}}{11+9e^{10x}+7e^{18x}+5e^{24x}+3e^{28x}+e^{30x}}\right)\right](1-\rho) + \left(\frac{35Ng^2\beta^2}{12kT}\right)\rho + N\alpha$

Where x = J/kT
J = exchange integral
g = Landé splitting facter
ρ = fraction of paramagnetic impurity
Nα = temperature independant paramagnetism
θ = Weiss-like correction
$R = [\Sigma(\chi_{obs} - \chi_{calc})^2 / \Sigma\chi_{obs}^2]^{1/2}$

quite strongly coupled on the basis of a much reduced room temperature magnetic moment. The observation of two quite different μ_{eff} values for **10** and **11** is a little unusual, since they appear to be essentially structurally identical based on the spectroscopic data, and should therefore exhibit similar magnetic properties. For an isolated octahedral Mn(II) system, μ_{eff} usually lies in the range 5.7 - 6.0 BM. The Mn(II) complexes **15** - **16** both have μ_{eff} values which lie just below this range, indicating again that they are most likely antiferromagnetically coupled. Certain proof of this in both the Ni(II) and Mn(II) cases, however, must rely on the variable temperature magnetic data.

Variable temperature magnetic susceptibility data and reasonable fitting of the data to the appropriate equations were obtained for **10** and **13** - **15**. The χ_M vs. T experimental data and non-linear least squares best fit lines for **10**, **13** - **15** are shown in Fig.5.2 to Fig.5.5, respectively. As can be seen in both the numerical data and the χ_M vs. T plots, relatively poor data fits were obtained for all of the complexes, especially for **10** and **15**. Overall, however, the variable temperature data are consistent with the room temperature magnetic data: all of the complexes exhibit antiferromagnetic coupling, and the observed relative magnitudes of coupling for the three Ni(II) complexes are consistent with the observed μ_{eff} values.

The relatively strong antiferromagnetic coupling observed for the Ni(II) complexes **10** and **13** is presumably a function of coupling through azide

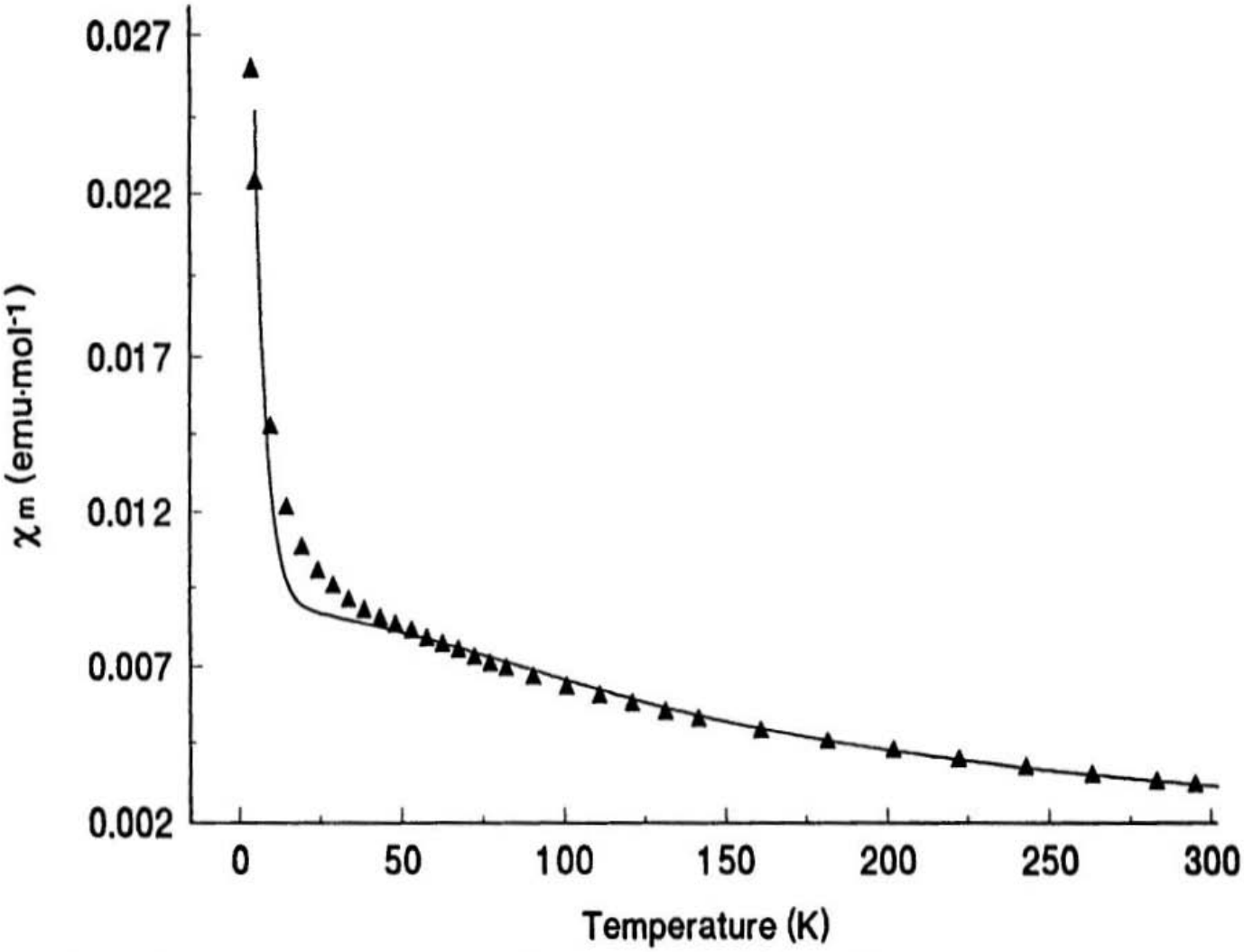

Fig. 5.2 Variable Temperature Magnetic Susceptibilty Data for $[Ni_2(PHP6Me\text{-}H)(N_3)_3(CH_3OH)]$ (10) with the Ginsberg Equation Least Squares Best Fit Line.

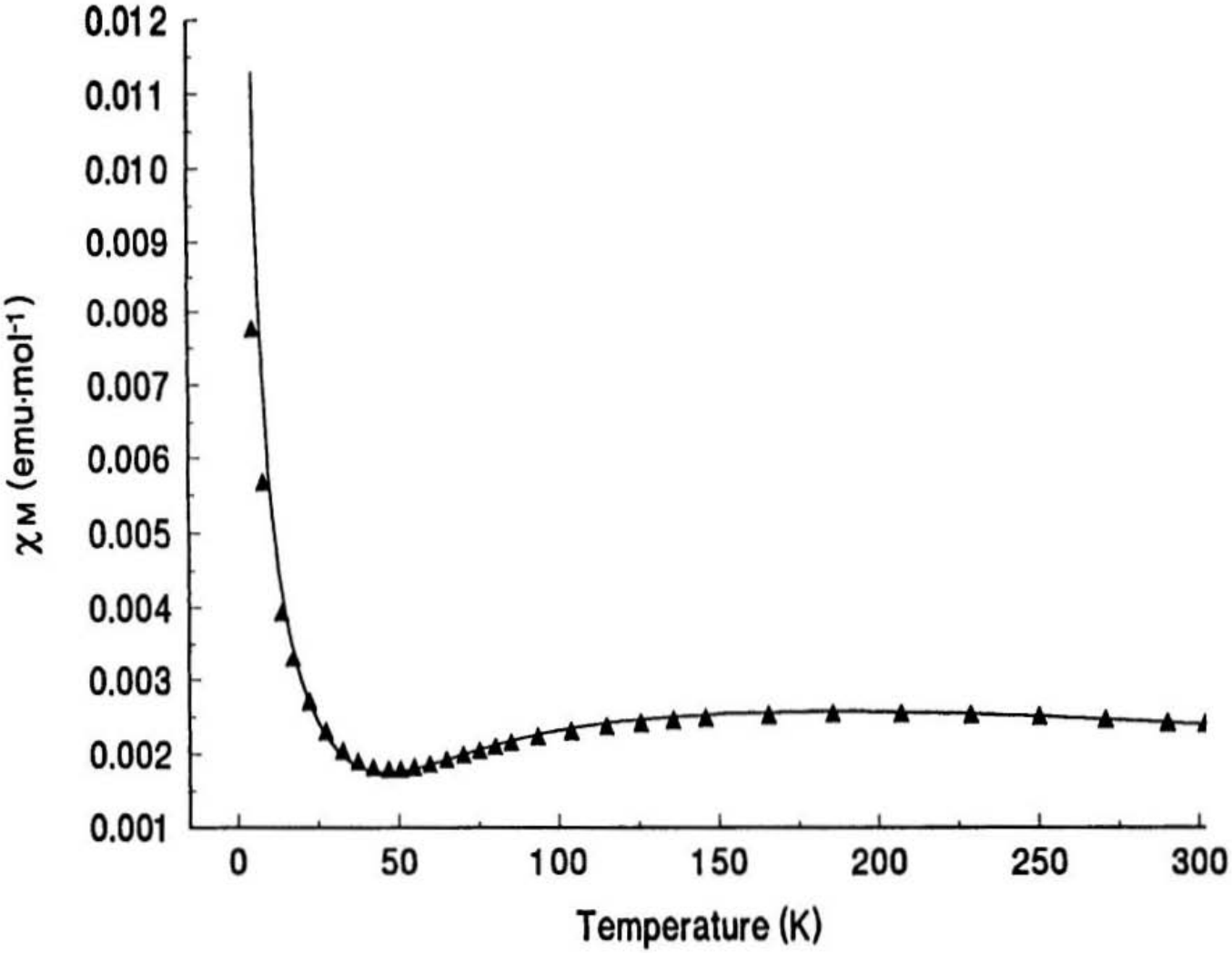

Fig. 5.3 Variable Temperature Magnetic Susceptibilty Data for $[Ni_2(PHP6Me\text{-}H)(N_3)_3(CH_3OH)_2]$ (13) with the Ginsberg Equation Least Squares Best Fit Line.

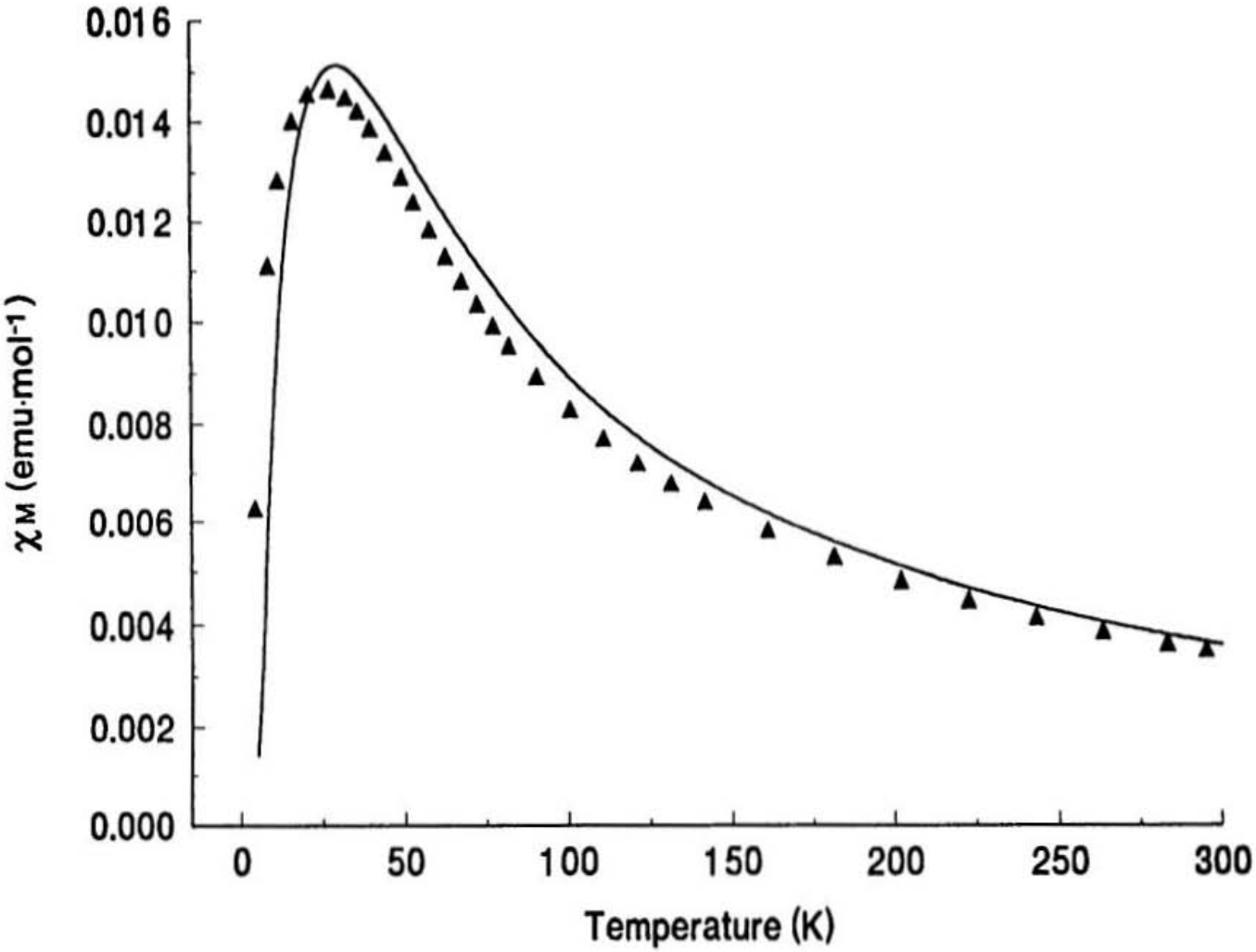

Fig. 5.4 Variable Temperature Magnetic Susceptibility Data for $[Ni_2(PHP6Me)Cl(NCS)_2(H_2O)(CH_3CH_2OH)][Ni_2(PHP6Me)Cl(NCS)(H_2O)]Cl_3$ (14) with the Ginsberg Equation Least Squares Best Fit Line.

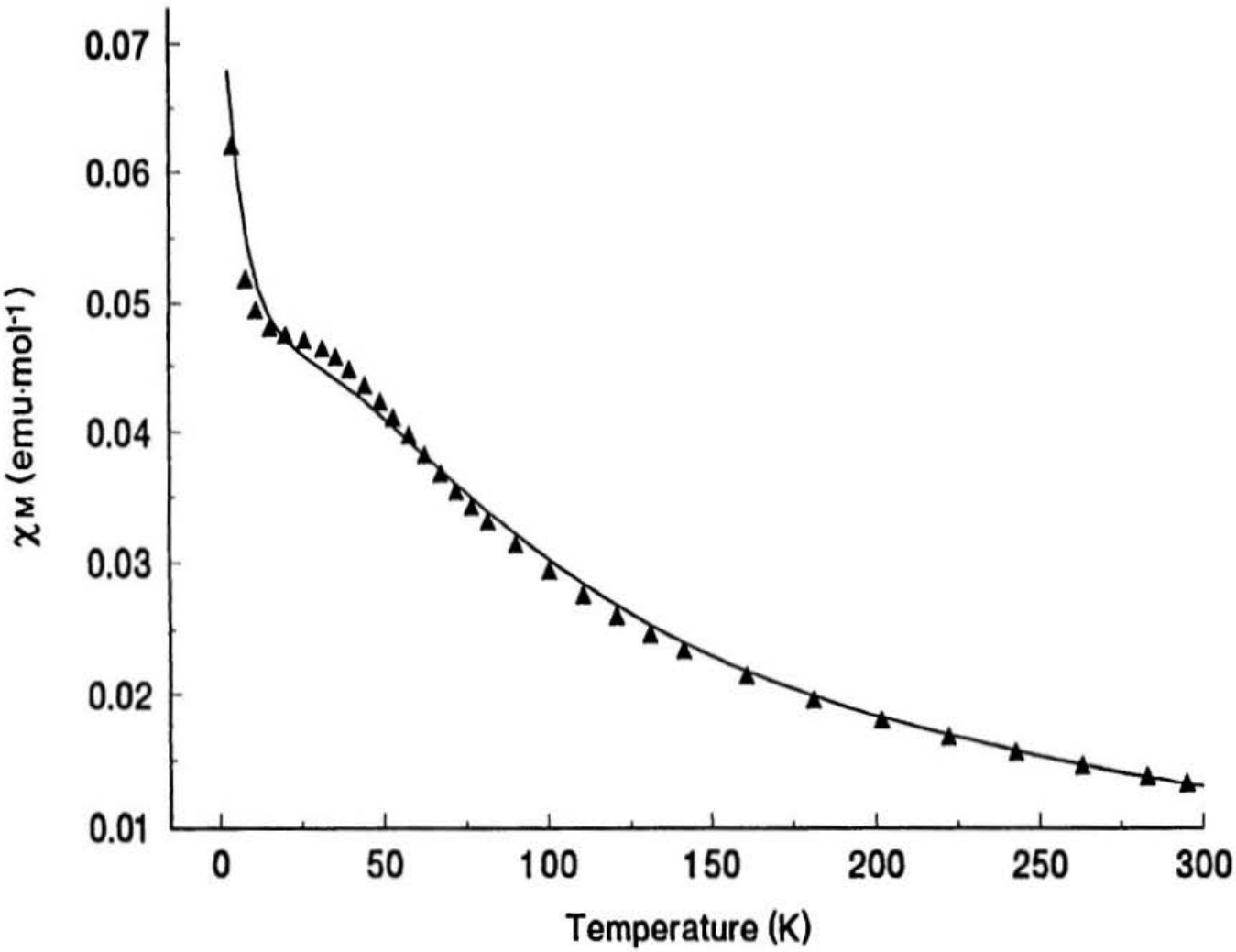

Fig. 5.5 Variable Temperature Magnetic Susceptibilty Data for $[Mn_2(PHP6Me\text{-}H)(N_3)_3(H_2O)_{2.5}]$ (13) with the Mn(II) Binuclear Equation (2.17) Least Squares Best Fit Line.

bridges. As has been noted, it is uncertain if this coupling is occurring solely through a μ_2-1,1 bridge, or a combination of μ_2-1,1 and μ_2-1,3 bridges. In fact, the poor data fit for **10** suggests that the system may be more complex than a simple binuclear system, even though attempts to fit the data to a 1D chain equation were unsuccessful. The need to include a high paramagnetic impurity of **12%** to get the data to fit to the Ginsberg equation is also an indication of problems with this system. The better fit for **13** supports the formulation of this system as a simple binuclear centre. Again, however, whether the coupling is mainly via μ_2-1,1 or μ_2-1,3 bridges is uncertain. Even bearing this in mind, it is exceptionally strongly coupled even for a μ_2-1,3 bridged Ni(II) binuclear system. For the thiocyanate complex **14**, the preliminary crystal structure indicates that the coupling must occur via the phthalazine diazine and chloride bridges. The magnitude of the coupling is in good agreement with the structurally analogous $[Ni_2(PHP6Me)Cl(H_2O)_4]\ Cl_3(H_2O)_4$[86] ($J$ = 12.99(6) cm^{-1}) from which it is derived, and which is also bridged by a phthalazine diazine moiety and chloride.

Similar to the Ni(II) / azide complexes, the Mn(II) / azide complex **15** is also antiferromagnetically coupled, although again the pathway of the magnetic exchange is uncertain. Of particular interest here is the TIP value. Generally, Mn(II) systems do not exhibit temperature independent paramagnetism because there is no appropriate excited state available for the required ground / excited state mixing to occur. The observed minor TIP term is probably due to the

presence of some oxidised Mn(III) impurity, which may also account for the poor overall data fit.

5.4 Conclusions

The synthesis and characterisation of some Ni(II) and Mn(II) coordination complexes of the ligand PHP6Me, and azide or thiocyanate has been presented. However, the available data proves to be inconclusive with respect to the structure of the complexes, and in particular precisely what types of bridging is exhibited by the azide ligands, and consequently how are the metal centres are magnetically coupled. The magnetic data are similarly inconclusive, with generally poor data fits being obtained using the appropriate equations for binuclear systems. The results presented here must therefore be considered only preliminary, and further investigation is required to establish magnetostructural correlations for the Ni(II) and Mn(II) azide / diazine bridged class of complexes.

References

1) P.K. Ross, E.I. Solomon, J. Am. Chem. Soc., **1991**, 113, 3246.

2) (a) R.R. Jacobson, Z. Tyeklár, A. Farooq, K.D. Karlin, S. Liu, J. Zubieta, J. Am. Chem. Soc., **1988**, 110, 3690.
(b) Z. Tyeklár, R.R. Jacobson, N. Wei, N.N. Murthy, J. Zubieta, K.D.Karlin, J. Am. Chem. Soc., **1993**. 115, 2677.

3) E.I. Solomon, B.L. Hemming, D.R. Root in Bioinorganic Chemistry of Copper, K.D. Karlin and Z. Tyeklár, Eds.; Chapman and Hall, New York, **1993**.

4) (a) N. Kitajima, K. Fujisawa, Y. Moro-oka, K. Toriumi, J. Am. Chem. Soc., **1989**, 111, 8975.
(b) N. Kitajima, K. Fujisawa, C. Fujimoto,Y. Moro-oka,Y. Hashimoto, T. Kitagawa, K. Toriumi, K. Tatsumi, A. Nakanura, J. Am. Chem. Soc., **1992**, 114,1277.

5) A. Volbeda, W.G.J. Hol, J. Mol. Biol., **1989**, 209, 249.

6) B. Hazes, K.A. Magnus, C. Bonaventura, J. Bonaventura, Z. Dauter, K.H. Kalk, W.G.J. Hol, Protein Science, **1993**, 2, 597.

7) K.A. Magnus, B. Hazes, H. Ton-That, C. Bonaventura, J. Bonaventura, W.G.J. Hol, Proteins: Structure, Function, and Genetics, **1994**, 19, 302.

8) K.A. Magnus, H. Ton-That, J.E. Carpenter, Chem. Rev., **1994**, 94, 727.

9) E.I. Solomon in Copper Proteins, T.G. Spiro, Ed.; Wiley Interscience, New York, **1981**.

10) P.A. Clark, D.E. Wilcox, Inorg. Chem., **1989**, 28, 1326.

11) (a) P.A. Clark, D.E. Wilcox, Inorg. Chem., **1990**, 29, 579.
(b) L. Alagna, S.S. Hasnain, B. Piggott, D.J. Williams, Biochem. J., **1984**, 220, 591.

12) E. Jabri, M.B. Carr, R.P. Hausinger, P.A. Karplus, Science, **1995**, 268, 998.

13) Manganese Redox Enzymes, V.L. Pecoraro, Ed.; VCH, New York, **1992**.

14) D.E. Wilcox, Chem. Rev., **1996**, 96, 2435.

15) R.S. Reczkowski, D.E. Ash, J. Am. Chem. Soc., **1992**, 114, 10992.

16) S.V. Khanglulov, P.J. Pessiki, V.V. Barynin, D.E. Ash, G.C. Dismukes, Biochem., **1995**, 34, 2015.

17) Z.Z. Kanyo, L.R. Scolnick, D.A. Ash, D.W. Christianson, Nature, **1996**, 383, 554.

18) A. Earnshaw, Introduction to Magnetochemistry; Academic Press, New York, **1968**.

19) C.J. O'Connor, Prog. Inorg. Chem., **1983**, 29, 203.

20) O. Kahn, Molecular Magnetism; VCH, New York, **1993**.

21) J.H. Van Vleck, The Theory of Electric and Magnetic Susceptibilities; Oxford University Press, London, **1932**.

22) K.S. Murray, Adv. Inorg. Chem., **1995**, 43, 261.

23) B. Bleaney, K.D. Bowers, Proc. R. Soc. (London), **1952**, A214, 451.

24) A.P. Ginsberg, M.E. Lines, Inorg. Chem., **1972**, 11, 2289.

25) A.P. Ginsberg, R.L. Martin, R.W. Brookes, R.C. Sherwood, Inorg. Chem., **1972**, 11, 2884.

26) D.V. Bautista, G. Bullock, F.W. Hartstock, L.K. Thompson, J. Heterocyclic. Chem., **1983**, 20, 345.

27) S.K. Mandal, L.K. Thompson, E.J. Gabe, J.P. Charland, Inorg. Chem., **1987**, 26, 2284.

28) L.K. Thompson, S.K. Mandal, J.P. Charland, E.J. Gabe, Can. J. Chem., **1988**, 66, 348.

29) (a) O. Kahn, Angew. Chem. Int. Ed. Engl., **1985**, 24, 834.
(b) M.F. Charlot, M. Verdaguer, Y. Journaux, P. de Loth, J.P. Daudey, Inorg.Chem., **1984**, 23, 3802.
(c) M. Julve, M. Verdaguer, A. Gleizes, M. Philoche-Levisalles, O. Kahn, Inorg. Chem., **1984**, 23, 3808.

30) V.H. Crawford, H.W. Richardson, J.R. Wasson, D.J. Hodgson, W.E. Hatfield, Inorg. Chem., **1976**, 15, 2107.

31) P.J. Hay, J.C. Thibeault, R. Hoffmann, J. Am. Chem. Soc., **1975**, 97, 4884.

32) O. Kahn, Inorg. Chim. Acta, **1982**, 62, 3.

33) L.K. Thompson, S.S. Tandon, F. Lloret, J. Cano, M. Julve, Inorg. Chem.,**1997**, 36, 3301.

34) M.A. Halcrow, J.-S. Sun, J.C. Huffman, G. Christou, Inorg. Chem., **1995**, 34, 4167.

35) (a) K.H. von Dahlen, J. Lorberth, J. Organomet. Chem., **1974**, 65, 267.
(b) M. Atam, U. Müller, J. Organomet. Chem., **1974**, 71, 435.

36) M.A.S. Goher, T.C.W. Mak, Inorg. Chim. Acta, **1984**, 85, 117.

37) F.A. Mautner, M.A.S. Goher, Polyhedron, **1992**, 11, 2537.

38) C.L. Sheppard, S.S. Tandon, L.K. Thompson, J.N. Bridson, D.O. Miller, M. Handa, F. Lloret, Inorg. Chim. Acta, **1996**, 250, 227.

39) R. Cortés, M. Drillon, X. Solans, L. Lezama, T. Rojo, Inorg. Chem., **1997**, 36, 677.

40) A. Escuer, R. Vincente, M.A.S Goher, F.A. Mautner, Inorg. Chem., **1997**, 36, 3440.

41) J. Ribas, M. Monfort, X. Solans, B.K. Ghosh, Angew. Chem. Int. Ed. Engl., **1994**, 33, 2087.

42) J. Ribas, M. Monfort, B.K. Ghosh, X. Solans, M. Font-Bardia, J. Chem. Soc, Chem. Commun., **1995**, 2375.

43) G. Viau, M.G. Lombardi, G. De Munno, M. Julve, F. Lloret, J. Faus, A. Caneschi, J.M. Clemente-Juan, J. Chem. Soc., Chem. Commun., **1997**, 1195.

44) J. Ribas, M. Monfort, I. Resino, X. Solans, P. Rabu, F. Maingot, M. Drillon, Angew. Chem. Int. Ed. Engl., **1996**, 35, 2520.

45) J.Ribas, M. Monfort, X. Solans, M. Drillon, Inorg. Chem., **1994**, 33, 742.

46) Y. Angus, R. Louis, J.P. Gisselbrecht, R. Weiss, J. Am. Chem. Soc., **1984**, 106, 93.

47) J. Comarmond, P. Plumeré, J.M. Lehn, Y. Angus, R. Louis, R. Weiss, O. Kahn, I. Morgenstern-Badarau, J. Am. Chem. Soc., **1982**, 104, 6330.

48) V. McKee, J.V. Dagdigian, R. Bau, C.A. Reed, J. Am. Chem. Soc., **1981**, 103, 7000.

49) P. Chaudhuri, K. Oder, K. Wieghardt, B. Nuber, J. Weiss, Inorg. Chem., **1986**, 25, 2818.

50) P. Chaudhuri, M. Guttmann, D. Vestur, K. Wieghardt, B. Nuber, J. Weiss, J. Chem. Soc., Chem. Commun., **1985**, 1618.

51) J. Ribas, M. Monfort, C. Diaz, C. Bastos, X. Solans, Inorg. Chem., **1993**, 32, 3557.

52) A. Escuer, R. Vincente, M.A.S. Goher, F.A. Mautner, Inorg. Chem., **1996**, 35, 6386.

53) A. Escuer, R. Vincente, J. Ribas, M. Salah El Falleh, X. Solans, M. Font-Bardia, Inorg. Chem., **1994**, 33, 1842.

54) M.G.B. Drew, M. McCann, S.M. Nelson, J. Chem. Soc., Chem. Commun., **1979**, 48.

55) K. Matsumoto, S. Ooi, K. Nakatsuka, W. Mori, S. Suzuki, A. Nakahara, V. Nakao, J. Chem. Soc., Dalton Trans., **1985**, 2095.

56) O. Kahn, S.Sikorav, J. Gouteron, S. Jeannin, Inorg. Chem., **1983**, 22, 2877.

57) S. Sikorav, I. Bkouche-Waksman, O. Kahn, Inorg. Chem., **1984**, 23, 490.

58) S.S. Tandon, L.K. Thompson, M.E. Manuel, J.N. Bridson, Inorg. Chem., **1994**, 33, 5555.

59) L.K. Thompson, S.S. Tandon, M.E. Manuel, Inorg. Chem., **1995**, 34, 2356.

60) M. Abersold, P. Bergerat, B. Gillon, O. Kahn, L. Pardi, F. Tukzek, L. Öhrström, A. Grand, NATO Advanced Research Workshop on Magnetism- A Supramolecular Function; Carcans-Maubuisson, France, Sept. 16-21, **1995**.

61) M.I. Arriortua, R. Cortés, L. Lezama, T. Rojo, X. Solans, M. Font-Bardia, Inorg. Chim. Acta, **1990**, 174, 263.

62) R. Cortés, J.I. Ruiz de Larramandi, L. Lezama, T. Rojo, K. Urtiaga, M.I. Arriortua, J. Chem. Soc., Dalton. Trans., **1992**, 2725.

63) A. Escuer, R. Vincente, J. Ribas, X. Solans, Inorg. Chem., **1995**, 34, 1793.

64) P. Chaudhuri, T. Weyhermüller, E. Bill, K. Wieghardt, Inorg. Chim. Acta, **1996**, 252, 195.

65) A. Escuer, R. Vicente, M. Salah El Fallah, X. Solans, M. Font-Bardia, Inorg. Chim. Acta, **1996**, 247, 85.

66) J. Ribas, M. Monfort, C. Diaz, C. Bastos, X. Solans, Inorg. Chem., **1994**, 33, 484.

67) R. Vincente, A. Escuer, J. Ribas, M. Salah el Fallah, X. Solans, M. Font-Bardia, Inorg. Chem., **1993**, 32, 1920.

68) P.D. Beer, M.G.B. Drew, P.B. Leeson, K. Lyssenko, M.I. Ogdens, J. Chem. Soc., Chem. Commun., **1995**, 929.

69) R. Cortés, L. Lezama, T. Rojo, K. Urtiaga, M. I. Arriortua, IEEE Trans. Mag., **1994**, 30, 4728.

70) R. Cortés, J. Luis Pizarro, L. Lezama, M. I. Arriortua, T. Rojo, Inorg. Chem., **1994**, 33, 2697.

71) K.R. Adam, A.J. Leong, L.F. Lindoy, B.J. McCool, A. Ekstrom, I. Liepa, P.A. Harding, K. Henrick, M. McPartlin, P.A. Tasker, J. Chem.Soc., Dalton Trans., **1987**, 2537.

72) G.A. van Albada, R.A.G. de Graaff, J.G. Haasnoot, J. Reedijk, Inorg. Chem., **1984**, 23, 1404.

73) S. Mohanta, K.K. Nanda, R. Werner, W. Haase, A.K. Mukherjee, S.K. Dutta, K. Nag, Inorg. Chem., **1997**, 36, 4656.

74) S. Brooker, R.J. Kelly, J. Chem. Soc., Dalton Trans., **1996**, 2117.

75) S. Raghunathan, C. Stevenson, J. Nelson, V. McKee, J. Chem. Soc., Chem. Commun., **1989**, 5.

76) S. Brooker, V. McKee, W.B. Sheppard, L.K. Oannell, J. Chem. Soc., Dalton Trans., **1987**, 2555.

77) D.M. Duggan, D.N. Henrickson, Inorg. Chem., **1974**, 13, 2929.

78) T. Rojo, R. Cortés, L. Lezama, M.I. Arriortua, K. Urtiaga, G. Villeneuve, J. Chem. Soc., Dalton Trans., **1991**, 1779.

79) M. Monfort, C. Bastos, C. Diaz, J. Ribas, Inorg. Chim. Acta, **1994**, 218, 185.

80) R. Vicente, A. Escuer, J. Ribas, X. Solans, J. Chem. Soc., Dalton. Trans., **1994**, 259.

81) M. Monfort, J. Ribas, X. Solans, Inorg. Chem., **1994**, 33, 4271.

82) E.J. Laskowski, D.N. Hendrickson, Inorg. Chem., **1978**, 17, 457.

83) J.N. McElearney, L.L. Balagot, J.A. Muir, R.D. Spence, Phys. Rev. B, **1979**, 19, 306.

84) J.B. Goodenough, Magnetism and the Chemical Bond; Interscience, New York, **1963**.

85) P.W. Anderson in Magetism, G.T. Rado, H. Suhl, Eds.; Academic Press, New York, **1963**.

86) T. Wen, L.K. Thompson, F.L. Lee, E.J. Gabe, Inorg. Chem., **1988**, 27, 4190.

87) C. Mealli, D.M. Proserpio, J. Chem. Ed., **1990**, 67, 399.

88) F. Lloret, Personal Communication

89) G. De Munno, G. Denti, P. Dapporto, Inorg. Chim. Acta, **1983**, 74, 199.

90) G. De Munno, G. Bruno, Acta Crystallogr., Sect. C, **1984**, 40, 2022.

91) S.K. Mandal, L.K. Thompson, E.J. Gabe, F.L. Lee, J.-P. Charland, Inorg. Chem., **1987**, 26, 2384.

92) L. Chen, L.K. Thompson, J.N. Bridson, Inorg. Chem., **1993**, 32, 2938.

93) L.K. Thompson, F.L. Lee, E.J. Gabe, Inorg. Chem., **1988**, 27, 39.

94) J. Manzur, A.M. Garcia, R. Letelier, E. Spodine, O. Penn, D. Grandjean, M.M. Olmstead, B.C. Noll, J. Chem. Soc., Dalton Trans., **1993**, 905.

95) P. Knuuttila, Inorg. Chim. Acta, **1982**, 58, 201.

96) H. Endres, D. Nöthe, E. Rossato, W.E. Hatfield, Inorg. Chem., **1984**, 23, 3467.

97) P.J. van Koningsbruggen, D. Gatteschi, R.A.G. de Graaff, J.G. Haasnoot, J. Reedijk, C. Zanchini, Inorg. Chem., **1995**, 34, 5175.

98) L.K. Thompson, A.W. Hanson, B.S. Ramaswamy, Inorg. Chem., **1984**, 23, 2459.

99) R. Beckett, R. Colton, B.F. Hoskins, R.L. Martin, D.G. Vince, Aust. J. Chem., **1969**, 22, 2527.

100) R. Beckett, B.F. Hoskins, J. Chem. Soc., Dalton Trans., **1972**, 291.

101) A.G. Bingham, H. Bögge, A. Müller, E.W. Ainscough, A.M. Brodie, J. Chem. Soc., Dalton Trans., **1987**, 493.

102) E.W. Ainscough, A.M. Brodie, J.D. Ranford, J.M. Waters, J. Chem. Soc., Dalton Trans., **1997**, 1251.

103) K. Nakamoto, Infrared Spectra of Inorganic and Coordination Compounds; Wiley-Interscience, New York, **1986**.

104) A.B.P. Lever, E. Mantovani, B.S. Ramaswamy, Can. J. Chem., **1971**, 49, 1957.

105) J.R. Ferraro, Low-Frequency Vibrations of Inorganic and Coordination Compounds; Plenum Press, New York, **1971**

106) L.K. Thompson, V.T. Chacko, J.A. Elvidge, A.B.P. Lever, R.V. Parish, Can. J. Chem., **1969**, 47, 4141.

107) G. Bullock, F.W. Hartstock, L.K. Thompson, Can. J. Chem., **1983**, 61, 57.

108) J.E. Pate, P.K. Ross, T.J. Thamann, C.A. Reed, K.D. Karlin, T.N. Sorrell, E.I. Solomon, J. Am. Chem. Soc., **1989**, 111, 5198.

109) F. Tuczek, E.I. Solomon, Inorg. Chem., **1993**, 32, 2850.

110) I. von Seggern, F. Tuczek, W. Bensch, Inorg. Chem., **1995**, 34, 5530.

111) A.B.P. Lever, Inorganic Electronic Spectroscopy; Elsevier, New York, **1984**.

112) S.S. Tandon, S.K. Mandal, L.K. Thompson, R.C. Hynes, Inorg. Chem., **1992**, 31, 2215.

113) J.V. Folgado, R.Ibáñez, E. Coronado, D. Beltrán, J.M. Savariault, Inorg. Chem., **1988**, 27, 19.

114) M. Mikuriya, H. Ôkawa, S. Kida, Bull. Chem. Soc. Jpn., **1981**, 54, 2979.

115) O. Kahn, I. Morgenstern, J.P. Audiere, J.M. Lehn, S.A. Sullivan, J. Am. Chem. Soc., **1980**, 102, 5936.

116) Y. Nishida, S. Kida, J. Chem. Soc., Dalton. Trans., **1986**, 2633.

117) V. McKee, M. Zvagulis, C.A. Reed, Inorg. Chem., **1985**, 24, 2914.

118) V. McKee, M. Zvagulis, J.V. Dagdigian, M.G. Patch, C.A. Reed, J.Am.Chem.Soc., **1984**, 106,4765.

119) A. Escuer, R. Vicente, B. Mernari, A.E. Gueddi, M. Pierrot, Inorg. Chem., **1997**, 36, 2511.

120) L.K. Thompson, S.K. Mandel, E.J. Gabe, J.-P. Charland, J. Chem. Soc., Chem. Commun., **1986**, 1537.

121) G.A. Reynolds, J.A. VanAllan, J.F. Tinker, J. Org. Chem., **1959**, 24, 1205.

122) S.K. Mandal, L.K. Thompson, M. J. Newlands, J.-P. Charland, E.J. Gabe, Inorg. Chim. Acta, **1990**, 178,169.

123) J.H. Boughton, R.N. Keller, J. Inorg. Nucl. Chem., **1966**, 28, 2851.

Appendix A

Eigenvalue Energies and $F_n(J,D,T)$ Functions for the Binuclear Ni(II) Expression for Magnetic Coupling

The energy eigenfunctions calculated from (2.18) using the Hamiltonian (2.17) and the Van Vleck equation (2.8) are:

$$E_1 = E_2 = -6J - 2D - \frac{g_x^2\beta^2H^2}{D}$$

$$E_3 = E_4 = -6J - D + g_x^2\beta^2H^2\left(\frac{1}{D} - \frac{3C_2^2}{6J-2\delta} - \frac{3C_1^2}{6J-2\delta}\right)$$

$$E_5 = -3J - D - \delta + \frac{3g_x^2\beta^2H^2C_2^2}{3J-\delta}$$

$$E_6 = E_7 = -2J - D + \frac{g_x^2\beta^2H^2}{2D}$$

$$E_8 = -2J - 2D - \frac{g_x^2\beta^2H^2}{D}$$

$$E_9 = -3J - D + \delta + \frac{3g_x^2\beta^2H^2C_1^2}{3J-\delta}$$

The coefficents C_1, C_2, and δ are defined as

$$C_1 = \frac{2\sqrt{2}\,D}{[(9J-D+3\delta)^2+8D^2]^{\frac{1}{2}}}$$

$$C_2 = \frac{(9J-D+3\delta)}{[(9J-D+3\delta)^2+8D^2]^{\frac{1}{2}}}$$

$$\delta = [(3J+D)^2 - 8JD]^{\frac{1}{2}}$$

The functions $F_n(J,D,T)$ used in (2.19), (2.20), (2.21a), (2.21b), and (2.23) are:

$$F_1(J,D,T) = \frac{e^{\frac{4J}{kT}} + 4e^{\frac{4J}{kT}}e^{\frac{D}{kT}} + 1}{2 + e^{\frac{D}{kT}} + 2e^{\frac{4J}{kT}} + e^{\frac{J}{kT}}e^{\frac{-\delta}{kT}} + e^{\frac{J}{kT}}e^{\frac{\delta}{kT}} + 2e^{\frac{4J}{kT}}e^{\frac{D}{kT}}}$$

$$F_2(J,D,T) = \frac{e^{\frac{D}{kT}} + 2e^{\frac{4J}{kT}}e^{\frac{D}{kT}} - 2e^{\frac{4J}{kT}} - 1}{2 + e^{\frac{D}{kT}} + 2e^{\frac{4J}{kT}} + e^{\frac{J}{kT}}e^{\frac{-\delta}{kT}} + e^{\frac{J}{kT}}e^{\frac{\delta}{kT}} + 2e^{\frac{4J}{kT}}e^{\frac{D}{kT}}}$$

$$F_3(J,D,T) = \frac{e^{\frac{4J}{kT}} - e^{\frac{J}{kT}}e^{\frac{\delta}{kT}}}{2 + e^{\frac{D}{kT}} + 2e^{\frac{4J}{kT}} + e^{\frac{J}{kT}}e^{\frac{-\delta}{kT}} + e^{\frac{J}{kT}}e^{\frac{\delta}{kT}} + 2e^{\frac{4J}{kT}}e^{\frac{D}{kT}}}$$

$$F_4(J,D,T) = \frac{e^{\frac{4J}{kT}} - e^{\frac{J}{kT}}e^{\frac{-\delta}{kT}}}{2 + e^{\frac{D}{kT}} + 2e^{\frac{4J}{kT}} + e^{\frac{J}{kT}}e^{\frac{-\delta}{kT}} + e^{\frac{J}{kT}}e^{\frac{\delta}{kT}} + 2e^{\frac{4J}{kT}}e^{\frac{D}{kT}}}$$

$$F'(J,D,T) = D^{-1}F_2(J,D,T) + \frac{3C_2^2}{3J-\delta}F_3(J,D,T) + \frac{3C_1^2}{3J+\delta}F_4(J,D,T)$$

Appendix B

Crystallographic Data

Crystal Data (@ 50K) for $[Cu_4(PAP3Me\text{-}H)_2(N_3)_6]$ (1)

Parameter	Value
Empirical Formula	$C_{20}H_{17}N_{15}Cu_2$
Formula Weight ($g \cdot mol^{-1}$)	594.57
Crystal Colour	dark green
Crystal Dimensions (mm)	0.32 x 0.22 x 0.20
Crystal System	monoclinic
Space Group	$P2_1/c$
a (Å)	8.9135(3)[a]
b (Å)	14.6366(4)
c (Å)	17.1885(4)
β (°)	92.3720(10)
d_{calcd} ($g \cdot cm^{-3}$)	1.763
Z	4
Diffractometer	Siemens SMART
Abs. coeff., μ (cm^{-1})	19.45
Radiation, λ (Å)	Mo Kα, 0.71073
T (K)	50
F_{000}	1200
$2\theta_{max}$ (°)	51.50
Data Collected	9490
No. of Unique Data [I>2σ(I)]	3518
No. of Variables	339
Goodness of Fit[b]	1.120
R_1 [I>2σ(I)][c]	0.0333
wR_2 [I>2σ(I)][d]	0.0732

[a] Throughout this work, the value in parentheses is the esd in the last digit.

[b] Goodness of Fit = $[\Sigma w(|F_o| - |F_c|)^2 / (\text{No. of reflections - no. of parameters})]^{1/2}$.

[c] $R_1 = \Sigma(|F_o| - |F_c|) / \Sigma|F_o|$

[d] $wR_2 = [(\Sigma w(|F_o|^2 - |F_c|^2)^2 / [\Sigma w(|F_o|^2)^2]^{1/2}$

Crystal Data (@ 90K) for $[Cu_4(PAP3Me\text{-}H)_2(N_3)_4]$ (1)

Parameter	Value
Empirical Formula	$C_{20}H_{17}N_{15}Cu_2$
Formula Weight ($g \cdot mol^{-1}$)	594.57
Crystal Colour	dark green
Crystal Dimensions (mm)	0.32 x 0.22 x 0.20
Crystal System	monoclinic
Space Group	$P2_1/c$
a (Å)	8.9149(1)[a]
b (Å)	14.6329(2)
c (Å)	17.1851(1)
β (°)	92.42(1)
d_{calcd} ($g \cdot cm^{-3}$)	1.763
Z	4
Diffractometer	Siemens SMART
Abs. coeff., μ (cm^{-1})	19.46
Radiation, λ (Å)	Mo Kα, 0.71073
T (K)	90
F_{000}	1200
$2\theta_{max}$ (°)	56.56
Data Collected	26887
No. of Unique Data [$I>2\sigma(I)$]	5546
No. of Variables	340
Goodness of Fit[b]	1.092
R_1 [$I>2\sigma(I)$][c]	0.0315
wR_2 [$I>2\sigma(I)$][d]	0.0660

[a] Throughout this work, the value in parentheses is the esd in the last digit.

[b] Goodness of Fit = $[\Sigma w(|F_o|-|F_c|)^2 / (\text{No. of reflections - no. of parameters})]^{1/2}$.

[c] $R_1 = \Sigma(|F_o|-|F_c|) / \Sigma|F_o|$

[d] $wR_2 = [(\Sigma w(|F_o|^2-|F_c|^2)^2 / [\Sigma w(|F_o|^2)^2]^{1/2}$

Crystal Data (@ 150K) for $[Cu_4(PAP3Me\text{-}H)_2(N_3)_6]$ (1)

Parameter	Value
Empirical Formula	$C_{20}H_{17}N_{15}Cu_2$
Formula Weight ($g \cdot mol^{-1}$)	594.57
Crystal Colour	dark green
Crystal Dimensions (mm)	0.14x 0.12 x 0.12
Crystal System	monoclinic
Space Group	$P2_1/c$
a (Å)	8.9332(3)[a]
b (Å)	14.6196(4)
c (Å)	17.1857(4)
β (°)	92.605(1)
d_{calcd} ($g \cdot cm^{-3}$)	1.761
Z	4
Diffractometer	Siemens SMART
Abs. coeff., μ (cm^{-1})	19.44
Radiation, λ (Å)	Mo Kα, 0.71073
T (K)	150
F_{000}	1200
$2\theta_{max}$ (°)	50.06
Data Collected	16209
No. of Unique Data [I>2σ(I)]	3966
No. of Variables	340
Goodness of Fit[b]	1.079
R_1 [I>2σ(I)][c]	0.0241
wR_2 [I>2σ(I)][d]	0.0570

[a] Throughout this work, value in parentheses is the esd in the last digit.

[b] Goodness of Fit = $[\Sigma w(|F_o| - |F_c|)^2 / (\text{No. of reflections - no. of parameters})]^{1/2}$.

[c] $R_1 = \Sigma(|F_o| - |F_c|) / \Sigma|F_o|$

[d] $wR_2 = [(\Sigma w(|F_o|^2 - |F_c|^2)^2 / [\Sigma w(|F_o|^2)^2]^{1/2}$

Crystal Data (@ 290K) for $[Cu_4(PAP3Me\text{-}H)_2(N_3)_6]$ (1)

Parameter	Value
Empirical Formula	$C_{20}H_{17}N_{15}Cu_2$
Formula Weight ($g \cdot mol^{-1}$)	594.57
Crystal Colour	dark green
Crystal Dimensions (mm)	0.32x 0.22 x 0.20
Crystal System	monoclinic
Space Group	$P2_1/c$
a (Å)	9.016(2)[a]
b (Å)	14.659(3)
c (Å)	17.309(4)
β (°)	93.23(1)
d_{calcd} ($g \cdot cm^{-3}$)	1.729
Z	4
Diffractometer	Siemens SMART
Abs. coeff., μ (cm^{-1})	19.08
Radiation, λ (Å)	Mo Kα, 0.71073
T (K)	290
F_{000}	1200
$2\theta_{max}$ (°)	56.58
Data Collected	27143
No. of Unique Data [I>2σ(I)]	5626
No. of Variables	340
Goodness of Fit[b]	1.142
R_1 [I>2σ(I)][c]	0.0422
wR_2 [I>2σ(I)][d]	0.0756

[a] Throughout this work, value in parentheses is the esd in the last digit.

[b] Goodness of Fit = $[\Sigma w(|F_o| - |F_c|)^2$ / (No. of reflections - no. of parameters)$]^{1/2}$.

[c] $R_1 = \Sigma(|F_o| - |F_c|) / \Sigma|F_o|$

[d] $wR_2 = [(\Sigma w(|F_o|^2 - |F_c|^2)^2 / [\Sigma w(|F_o|^2)^2]^{1/2}$

Crystal Data for $[Cu_4(PAP3Me)_2(N_3)_4(NO_3)_2(H_2O)_2](NO_3)_2(H_2O)_{0.76}$ (2)

Parameter	Value
Empirical Formula	$C_{20}H_{20.77}N_{14}O_{7.38}Cu_2$
Formula Weight ($g \cdot mol^{-1}$)	702.42
Crystal Colour	black
Crystal Dimensions (mm)	0.400x0.200 x 0.150
Crystal System	monoclinic
Space Group	C2/c
a (Å)	26.71(1)[a]
b (Å)	13.51(3)
c (Å)	16.84(1)
β (°)	117.35(3)
d_{calcd} ($g \cdot cm^{-3}$)	1.728
Z	8
Diffractometer	Rigaku AFC6S
Abs. coeff., μ (cm^{-1})	16.48
Radiation, λ (Å)	Mo Kα, 0.71073
T (K)	299
F_{000}	2846
$2\theta_{max}$ (°)	50.2
Data Collected	5133
No. of Unique Data [I>1.5σ(I)]	1863
No. of Variables	343
Goodness of Fit[b]	2.08
R [I>2σ(I)][c]	0.070
R_w [I>2σ(I)][d]	0.050

[a] Throughout this work, value in parentheses is the esd in the last digit.
[b] Goodness of Fit = $[\Sigma w(|F_o|-|F_c|)^2$ / (No. of reflections - no. of parameters)$]^{1/2}$.
[c] $\Sigma(|F_o|-|F_c|) / \Sigma|F_o|$
[d] $[(\Sigma w(|F_o|-|F_c|)^2 / [\Sigma w(|F_o|)^2]^{1/2}$

Crystal Data for $[Cu_2(PAP3Me)(N_3)_3(CH_3OH)](ClO_4)C_{0.5}N_{0.5}S_{0.5}$ (3)

Parameter	Value
Empirical Formula	$C_{21.5}H_{20}N_{15.5}O_5S_5ClCu_2$
Formula Weight ($g \cdot mol^{-1}$)	754.09
Crystal Colour	black
Crystal Dimensions (mm)	0.32 x 0.20 x 0.13
Crystal System	triclinic
Space Group	P-1
a (Å)	8.5328(1)
b (Å)	13.6204(1)
c (Å)	14.1372(1)
α (°)	108.57(1)
β (°)	98.57(1)
γ (°)	99.73(1)
d_{calcd} ($g \cdot cm^{-3}$)	1.671
Z	2
Diffractometer	Siemens SMART
Abs. coeff., μ (cm^{-1})	16.06
Radiation, λ (Å)	Mo Kα, 0.71073
T (K)	150
F_{000}	761
$2\theta_{max}$ (°)	50.0
Data Collected	13305
No. of Unique Data [$I>2\sigma(I)$]	5274
No. of Variables	403
Goodness of Fit[b]	1.126
R_1 [$I>2\sigma(I)$][c]	0.0641
wR_2 [$I>2\sigma(I)$][d]	0.1520

[a] Throughout this work, value in parentheses is the esd in the last digit.
[b] Goodness of Fit = $[\Sigma w(|F_o|-|F_c|)^2 / (\text{No. of reflections - no. of parameters})]^{1/2}$.
[c] $R_1 = \Sigma(|F_o|-|F_c|) / \Sigma|F_o|$
[d] $wR_2 = [(\Sigma w(|F_o|^2-|F_c|^2)^2 / [\Sigma w(|F_o|^2)^2]^{1/2}$

Crystal Data for $[Cu_2(PAP3Me)(SO_4)_2(H_2O)_4](H_2O)_{1.5}$ (6)

Parameter	Value
Empirical Formula	$C_{20}H_{29}N_6O_{13.50}S_2Cu_2$
Formula Weight ($g \cdot mol^{-1}$)	760.69
Crystal Colour	green
Crystal Dimensions (mm)	0.30x 0.20 x 0.40
Crystal System	monoclinic
Space Group	$P2_1/n$
a (Å)	13.863(8)[a]
b (Å)	35.067(4)
c (Å)	16.904(6)
β (°)	91.56(4)
d_{calcd} ($g \cdot cm^{-3}$)	1.845
Z	12
Diffractometer	Rigaku AFC6S
Abs. coeff., μ (cm^{-1})	17.86
Radiation, λ (Å)	Mo Kα, 0.71073
T (K)	299
F_{000}	4668
$2\theta_{max}$ (°)	50.2
Data Collected	15474
No. of Unique Data [$I>1.5\sigma(I)$]	8647
No. of Variables	1208
Goodness of Fit[b]	1.59
R [$I>2\sigma(I)$][c]	0.043
R_w [$I>2\sigma(I)$][d]	0.031

[a] Throughout this work, value in parentheses is the esd in the last digit.
[b] Goodness of Fit = $[\Sigma w(|F_o|-|F_c|)^2 / (\text{No. of reflections - no. of parameters})]^{1/2}$.
[c] $\Sigma(|F_o|-|F_c|) / \Sigma|F_o|$
[d] $[(\Sigma w(|F_o|-|F_c|)^2 / [\Sigma w(|F_o|)^2]^{1/2}$

Appendix C

Intermolecular Hydrogen Bonds in $[Cu_2(PAP3Me)(SO_4)_2(H_2O)_4](H_2O)_{1.5}$ (6)

All interactions for which the contact distance is less than or equal to the sum of the Van der Waals radii of the two atoms involved are reported.

Van der Waals Radii Used

H	1.2 Å
O	1.4 Å
S	1.85 Å

Atoms	Distance (Å)	Type of Interaction
S(1) H(73)	2.627	SO_4^{2-} Bridge Sulfur / Lattice H_2O Hydrogen
O(2) H(52)	2.052	SO_4^{2-} Bridge Oxygen / N-H Hydrogen
O(3) H(76)	1.675	SO_4^{2-} Bridge Oxygen / Coord. H_2O Hydrogen
O(4) H(73)	1.656	SO_4^{2-} Bridge Oxygen / Lattice H_2O Hydrogen
O(6) H(51)	2.066	SO_4^{2-} Bridge Oxygen / N-H Hydrogen
O(8) H(68)	2.094	SO_4^{2-} Bridge Oxygen / Coord. H_2O Hydrogen
O(15) H(61)	2.161	SO_4^{2-} Bridge Oxygen / N-H Hydrogen
O(16) H(60)	2.223	SO_4^{2-} Bridge Oxygen / Coord. H_2O Hydrogen
O(18) H(49)	2.317	SO_4^{2-} Bridge Oxygen / N-H Hydrogen
O(19) H(74)	2.066	SO_4^{2-} Bridge Sulfur / Lattice H_2O Hydrogen
O(20) H(79)	2.009	SO_4^{2-} Bridge Oxygen / Coord. H_2O Hydrogen
O(23) H(72)	2.365	Coord. H_2O Oxygen / Lattice H_2O Hydrogen

Atoms	Distance (Å)	Type of Interaction
O(28) H(29)	2.310	SO_4^{2-} Bridge Oxygen / C-H Methyl Hydrogen
O(28) H(53)	2.315	SO_4^{2-} Bridge Oxygen / N-H Hydrogen
O(29) H(53)	2.182	SO_4^{2-} Bridge Oxygen / N-H Hydrogen
O(29) H(20)	2.388	SO_4^{2-} Bridge Oxygen / C-H Ring Hydrogen
O(30) H(54)	2.140	SO_4^{2-} Bridge Oxygen / Coord. H_2O Hydrogen
O(31) H(54)	2.008	SO_4^{2-} Bridge Oxygen / Coord. H_2O Hydrogen
O(33) H(58)	2.063	SO_4^{2-} Bridge Oxygen / Coord. H_2O Hydrogen
O(34) H(56)	2.006	SO_4^{2-} Bridge Oxygen / Coord. H_2O Hydrogen
O(34) H(57)	2.211	SO_4^{2-} Bridge Oxygen / Coord. H_2O Hydrogen
O(35) H(50)	2.300	SO_4^{2-} Bridge Oxygen / N-H Hydrogen
O(40) H(66)	1.887	Lattice H_2O Oxygen / Coord. H_2O Hydrogen
O(41) H(5)	2.230	Lattice H_2O Oxygen / C-H Ring Hydrogen
O(41) H(42)	2.270	Lattice H_2O Oxygen / C-H Ring Hydrogen
O(42) H(80)	1.734	Lattice H_2O Oxygen / Coord. H_2O Hydrogen
O(43) H(63)	1.916	Lattice H_2O Oxygen / Coord. H_2O Hydrogen
O(44) H(70)	1.810	Lattice H_2O Oxygen / Coord. H_2O Hydrogen

Appendix D

Variable Temperature χ_M vs. T Magnetic Susceptibility Data

$[Cu_4(PAP3Me\text{-}H)_2(N_3)_6]$ (1)		$[Cu_4(PAP3Me)_2(N_3)_4(NO_3)_2(H_2O)_2](NO_3)_2$ (2)		$[Cu_2(PAP3Me)(N_3)_3(CH_3OH)](ClO_4)(H_2O)$ (3)	
T(K)	χ_M (emu/mol)	T(K)	χ_M (emu/mol)	T(K)	χ_M (emu/mol)
4.667	3.923E-003	5.039	1.124E-003	4.020	7.478E-004
8.769	4.114E-003	10.692	1.134E-003	5.846	5.237E-004
10.302	5.189E-003	13.755	1.207E-003	10.831	4.199E-004
15.022	5.636E-003	17.662	1.332E-003	15.863	3.449E-004
19.522	5.835E-003	21.969	1.491E-003	20.745	3.058E-004
24.310	5.819E-003	27.625	1.714E-003	25.602	2.819E-004
29.118	5.647E-003	32.174	1.888E-003	30.275	2.710E-004
33.932	5.362E-003	35.808	2.008E-003	34.999	2.657E-004
38.734	5.080E-003	40.048	2.128E-003	39.787	2.723E-004
43.566	4.801E-003	44.794	2.241E-003	44.482	2.955E-004
48.392	4.547E-003	49.563	2.320E-003	49.141	3.245E-004
53.200	4.332E-003	54.331	2.371E-003	53.862	3.545E-004
57.990	4.081E-003	59.314	2.403E-003	58.597	3.858E-004
62.816	3.851E-003	64.724	2.416E-003	63.336	4.221E-004
67.636	3.666E-003	70.071	2.414E-003	67.258	4.662E-004
72.450	3.493E-003	75.039	2.398E-003	72.717	5.016E-004
77.264	3.335E-003	80.387	2.373E-003	77.525	5.436E-004
82.072	3.188E-003	85.119	2.343E-003	82.292	5.846E-004
90.521	2.960E-003	93.322	2.285E-003	90.596	6.525E-004
100.750	2.722E-003	103.845	2.201E-003	100.725	7.272E-004
110.974	2.527E-003	114.933	2.112E-003	110.818	7.944E-004
121.192	2.355E-003	125.527	2.026E-003	120.934	8.423E-004
131.434	2.206E-003	135.736	1.944E-003	131.065	8.794E-004
141.669	2.074E-003	145.924	1.868E-003	141.202	9.044E-004
160.913	1.868E-003	166.119	1.731E-003	160.423	9.317E-004
181.385	1.690E-003	186.296	1.601E-003	180.998	9.419E-004
201.857	1.542E-003	207.118	1.489E-003	201.626	9.262E-004
222.310	1.419E-003	229.437	1.387E-003	222.143	9.102E-004
242.776	1.315E-003	250.099	1.298E-003	242.831	8.990E-004
263.259	1.223E-003	271.727	1.220E-003	263.220	8.657E-004
283.141	1.147E-003	286.222	1.171E-003	283.851	8.434E-004
295.134	1.104E-003	297.832	1.132E-003	296.003	8.311E-004

$[Cu_2(PAP3Me)(N_3)_2Cl_2](CH_3OH)_{1.5}$ (4)		$[Cu_4(PAP3Me)_2(N_3)_6Br_3]$ (5)		$[Cu_2(PAP3Me)(SO_4)_2(H_2O)_4](H_2O)$ (6)	
T(K)	χ_M (emu/mol)	T(K)	χ_M (emu/mol)	T(K)	χ_M (emu/mol)
5.318	2.098E-002	4.938	1.310E-002	3.480	3.579E-003
11.019	1.596E-002	10.464	1.218E-002	5.996	2.004E-003
14.207	1.435E-002	13.384	1.164E-002	10.610	1.169E-003
18.181	1.291E-002	17.284	1.074E-002	15.655	8.686E-004
22.445	1.170E-002	21.710	9.752E-003	20.381	8.281E-004
28.163	1.038E-002	26.358	8.797E-003	25.402	9.312E-004
31.954	9.633E-003	31.665	7.789E-003	30.456	1.144E-003
36.394	8.864E-003	35.904	7.082E-003	35.183	1.385E-003
40.451	8.248E-003	39.874	6.515E-003	39.944	1.647E-003
44.956	7.648E-003	44.634	5.947E-003	44.700	1.894E-003
49.970	7.083E-003	49.482	5.482E-003	49.423	2.112E-003
54.479	6.628E-003	54.282	5.096E-003	53.200	2.280E-003
59.493	6.177E-003	59.314	4.750E-003	58.038	2.375E-003
64.867	5.755E-003	64.724	4.434E-003	62.834	2.488E-003
70.155	5.393E-003	69.988	4.168E-003	67.636	2.570E-003
75.135	5.079E-003	74.942	3.940E-003	72.450	2.624E-003
80.276	4.803E-003	80.056	3.742E-003	77.270	2.655E-003
85.119	4.561E-003	84.995	3.568E-003	82.096	2.669E-003
93.620	4.195E-003	93.471	3.306E-003	90.521	2.665E-003
104.024	3.818E-003	103.842	3.035E-003	100.744	2.624E-003
114.937	3.490E-003	114.937	2.798E-003	110.962	2.557E-003
125.781	3.221E-003	125.781	2.601E-003	121.216	2.480E-003
135.737	2.995E-003	135.737	2.436E-003	131.440	2.398E-003
145.924	2.802E-003	145.924	2.294E-003	141.676	2.319E-003
165.700	2.494E-003	165.700	2.064E-003	160.919	2.173E-003
186.296	2.227E-003	186.809	1.862E-003	181.391	2.024E-003
207.118	2.015E-003	207.118	1.700E-003	201.845	1.893E-003
229.437	1.837E-003	229.437	1.563E-003	222.304	1.790E-003
250.908	1.688E-003	250.908	1.447E-003	242.782	1.667E-003
271.727	1.565E-003	271.727	1.350E-003	263.229	1.574E-003
286.222	1.488E-003	286.222	1.289E-003	283.117	1.494E-003
297.832	1.429E-003	298.870	1.243E-003	295.128	1.444E-003

$[Cu_2(PAP3Me)Cl_4]$ (7)		$[Cu_2(PAP3Me)(OH)(NO_3)_3](H_2O)$ (8)		$[Cu_2(PAP3Me)(OH)Br_3]$ (9)	
T(K)	χ_M (emu/mol)	T(K)	χ_M (emu/mol)	T(K)	χ_M (emu/mol)
3.517	8.316E-004	3.336	3.007E-003	3.577	3.769E-003
6.074	4.948E-004	5.827	1.743E-003	5.827	2.276E-003
10.592	3.171E-004	10.544	9.922E-004	10.544	1.344E-003
15.540	2.588E-004	15.522	7.090E-004	15.504	9.644E-004
20.351	3.014E-004	20.363	5.649E-004	20.357	7.826E-004
25.420	4.487E-004	25.396	4.730E-004	25.408	6.624E-004
30.450	6.789E-004	30.456	4.104E-004	30.450	5.863E-004
35.171	9.270E-004	35.165	3.682E-004	35.177	5.280E-004
39.902	1.186E-003	39.908	3.369E-004	39.890	4.873E-004
44.676	1.435E-003	44.688	3.130E-004	44.688	4.545E-004
49.399	1.651E-003	49.405	2.945E-004	49.393	4.285E-004
53.224	1.802E-003	53.266	2.822E-004	53.218	4.147E-004
58.002	1.918E-003	58.002	2.726E-004	58.002	3.984E-004
62.822	2.034E-003	62.816	2.648E-004	62.822	3.861E-004
67.630	2.119E-003	67.624	2.614E-004	67.630	3.780E-004
72.456	2.177E-003	72.456	2.622E-004	72.444	3.765E-004
77.252	2.215E-003	77.270	2.661E-004	77.252	3.777E-004
82.102	2.235E-003	82.084	2.734E-004	82.102	3.816E-004
90.527	2.242E-003	90.515	2.912E-004	90.521	3.947E-004
100.775	2.217E-003	100.750	3.216E-004	100.744	4.214E-004
110.986	2.166E-003	110.974	3.590E-004	110.968	4.544E-004
121.216	2.105E-003	123.352	3.998E-004	121.210	4.942E-004
131.446	2.040E-003	131.554	4.407E-004	131.428	5.300E-004
141.663	1.974E-003	141.663	4.782E-004	141.657	5.696E-004
160.919	1.852E-003	160.925	5.440E-004	160.932	6.323E-004
181.397	1.725E-003	181.391	6.039E-004	181.397	6.897E-004
201.857	1.613E-003	201.851	6.494E-004	201.845	7.332E-004
222.304	1.521E-003	222.298	6.809E-004	222.298	7.556E-004
242.782	1.418E-003	242.794	7.033E-004	242.782	7.826E-004
263.205	1.338E-003	263.235	7.166E-004	263.229	7.943E-004
283.087	1.269E-003	283.117	7.219E-004	283.105	7.916E-004
295.134	1.226E-003	295.128	7.224E-004	295.110	8.000E-004

$[Ni_2(PHP6Me\text{-}H)(N_3)_3(CH_3OH)]$ (10)		$[Ni_2(PAP6Me\text{-}H)(N_3)_3(CH_3OH)_2]$ (13)		$[Ni_2(PHP6Me)Cl(NCS)_2(H_2O)(CH_3CH_2OH)][Ni_2(PHP6Me)Cl(NCS)(H_2O)_2]Cl_3$ (14)	
T(K)	χ_M (emu/mol)	T(K)	χ_M (emu/mol)	T(K)	χ_M (emu/mol)
3.893	2.602E-002	5.100	7.771E-003	4.263	6.295E-003
5.060	2.243E-002	8.250	5.686E-003	8.343	1.111E-002
9.862	1.480E-002	13.663	3.943E-003	11.639	1.2842E-002
14.658	1.220E-002	17.368	3.308E-003	16.034	1.4022E-002
19.472	1.089E-002	22.255	2.722E-003	20.905	1.4579E-002
24.310	1.011E-002	27.306	2.324E-003	27.328	1.4674E-002
29.106	9.618E-003	32.429	2.058E-003	32.484	1.4511E-002
33.914	9.160E-003	37.233	1.906E-003	36.339	1.4235E-002
38.740	8.828E-003	42.051	1.825E-003	40.161	1.3882E-002
43.566	8.574E-003	46.828	1.802E-003	44.754	1.3404E-002
48.374	8.370E-003	50.510	1.808E-003	49.483	1.2909E-002
53.182	8.182E-003	54.728	1.832E-003	53.242	1.2397E-002
57.984	7.948E-003	59.613	1.876E-003	58.020	1.1846E-002
62.810	7.761E-003	64.867	1.937E-003	62.828	1.1298E-002
67.606	7.579E-003	70.155	2.000E-003	67.624	1.0799E-002
72.426	7.347E-003	75.135	2.061E-003	72.444	1.0340E-002
77.264	7.145E-003	80.166	2.118E-003	77.282	9.9216E-003
82.090	6.996E-003	84.995	2.170E-003	82.090	9.5395E-003
90.515	6.719E-003	93.471	2.2496E-003	90.521	8.9432E-003
100.732	6.410E-003	103.842	2.326E-003	100.763	8.298E-003
110.956	6.137E-003	114.937	2.388E-003	110.986	7.715E-003
121.204	5.870E-003	125.523	2.437E-003	121.216	7.220E-003
131.422	5.619E-003	135.737	2.471E-003	131.422	6.792E-003
141.633	5.381E-003	145.924	2.500E-003	141.657	6.421E-003
160.895	4.982E-003	165.700	2.534E-003	160.925	5.826E-003
181.415	4.634E-003	185.785	2.553E-003	181.391	5.283E-003
201.869	4.359E-003	207.118	2.549E-003	201.857	4.842E-003
222.316	4.058E-003	228.730	2.538E-003	222.316	4.467E-003
242.788	3.787E-003	250.099	2.515E-003	242.782	4.149E-003
263.241	3.555E-003	270.818	2.480E-003	263.229	3.884E-003
283.129	3.360E-003	290.185	2.436E-003	283.123	3.652E-003
295.128	3.256E-003	302.014	2.418E-003	295.128	3.526E-003

[Mn_2(PAP6Me-H)(N_3)$_3$ (H_2O)$_{2.5}$] (15)

T(K)	χ_M (emu/mol)
4.227	6.211E-002
8.277	5.191E-002
11.417	4.948E-002
15.823	4.803E-002
20.592	4.749E-002
26.401	4.705E-002
31.937	4.642E-002
35.929	4.572E-002
40.047	4.477E-002
44.766	4.354E-002
49.453	4.231E-002
53.224	4.115E-002
58.026	3.981E-002
62.822	3.829E-002
67.630	3.684E-002
72.468	3.550E-002
77.252	3.428E-002
82.090	3.317E-002
90.539	3.140E-002
100.750	2.946E-002
110.974	2.766E-002
121.216	2.610E-002
131.422	2.474E-002
141.657	2.352E-002
160.913	2.152E-002
181.391	1.966E-002
201.857	1.813E-002
222.286	1.679E-002
242.788	1.563E-002
263.229	1.465E-002
283.117	1.381E-002
295.134	1.330E-002

Appendix E

Input Files and Parameters Used in the EHMO Model Study

I. Variation of Cu-N_3-Cu Angle in Model Complex M1 †

```
# PHTHALAZINE WITH CU/NH3/N3 (CU-N3-CU = 90)
 37  3DIST    0  0
 EL WF CM OV OP RO NC
0.,0.,0.,DU
-1,1,NC 0.69,180.,0.
-1,2,NC 0.69,000.,0.
 1,3, C 1.32,120.,0.
 2,4, C 1.32,120.,0.
 3,5, H 1.10,240.,0.
 4,6, H 1.10,240.,0.
 3,7, C 1.45,120.,0.
 4,8, C 1.45,120.,0.
 7,9, C 1.40,240.,0.
 8,10, C 1.40,240.,0.
 9,11, H 1.10,240.,0.
10,12, H 1.10,240.,0.
 9,13, C 1.40,120.,0.
10,14, C 1.40,120.,0.
13,15, H 1.10,240.,0.
14,16, H 1.10,240.,0.
 1,17,CU 1.99,249.5,0.
 2,18,CU 1.99,249.5,0.
17,19,AM 1.97,180.,0.
17,23,AM 1.97,090.,0.
18,27,AM 1.97,180.,0.
18,31,AM 1.97,090.,0.
-1,35, N 3.25,270.,0.
35,36, N 1.20,180.,0.
36,37, N 1.20,180.,0.
```

† the input file presented here is for a Cu-N_3-Cu angle of 90°. The others were similar, with the only changes being in five membered ring angles.

II. Variation of $N_{diazine}$-$N_{diazine}$-Cu-N_{amine} Torsion Angle in Model Complex M2

```
# PHTHALAZINE WITH CU/NH3 (CU-N-N = 117)
 42  4DIST    1 10
40.,50.,60.,70.,80.,90.,100.,110.,120.,130.
 EL WF CM OV OP RO NC
0.,0.,0.,DU
-1,1,NC 0.69,180.,0.
-1,2,NC 0.69,000.,0.
 1,3, C 1.32,120.,0.
 2,4, C 1.32,120.,0.
 3,5, H 1.10,240.,0.
 4,6, H 1.10,240.,0.
 3,7, C 1.45,120.,0.
 4,8, C 1.45,120.,0.
 7,9, C 1.40,240.,0.
 8,10, C 1.40,240.,0.
 9,11, H 1.10,240.,0.
10,12, H 1.10,240.,0.
 9,13, C 1.40,120.,0.
10,14, C 1.40,120.,0.
13,15, H 1.10,240.,0.
14,16, H 1.10,240.,0.
 1,17,CU 1.99,243.,0.
 2,18,CU 1.99,243.,0.
17,19,AM 1.97,180.,0.
17,23,AM 1.97,090.,1000.
17,27,AM 1.97,270.,1000.
18,31,AM 1.97,180.,0.
18,35,AM 1.97,090.,1000.
18,39,AM 1.97,270.,1000.
```

III. Variation of Cu-$N_{diazine}$-$N_{diazine}$ Angle in Model Complex M2

```
# PHTHALAZINE WITH CU/NH3 (CU-N-N = 111)
 42  4DIST    2  8
249.,247.,245.,243.,241.,239.,237.,235.
249.,247.,245.,243.,241.,239.,237.,235.
 EL WF CM OV OP RO NC
0.,0.,0.,DU
-1,1,NC 0.69,180.,0.
-1,2,NC 0.69,000.,0.
 1,3, C 1.32,120.,0.
 2,4, C 1.32,120.,0.
 3,5, H 1.10,240.,0.
 4,6, H 1.10,240.,0.
 3,7, C 1.45,120.,0.
 4,8, C 1.45,120.,0.
 7,9, C 1.40,240.,0.
 8,10, C 1.40,240.,0.
 9,11, H 1.10,240.,0.
10,12, H 1.10,240.,0.
 9,13, C 1.40,120.,0.
10,14, C 1.40,120.,0.
13,15, H 1.10,240.,0.
14,16, H 1.10,240.,0.
 1,17,CU 1.99,1000.,0.
 2,18,CU 1.99,2000.,0.
17,19,AM 1.97,180.,0.
17,23,AM 1.97,090.,060.
17,27,AM 1.97,270.,060.
18,31,AM 1.97,180.,0.
18,35,AM 1.97,090.,060.
18,39,AM 1.97,270.,060.
```

IV. Trigonal Distortion of Azide Out of Cu_2N_2(diazine) Plane in Model Complex M1

```
# TRIGONAL DISTORTION OF N3, CU'S REMAIN IN PLANE (IDEAL GEO.)
 37  3DIST    1 19
0.1,5.,10.,15.,20.,25.,30.,35.,40.,45.,50.,55.,60.,65.,70.,75.,80.,85.,90.
  EL WF CM OV OP RO NC
0.,0.,0., N
 1,2, N 1.20,090.,1000.
 2,3, N 1.20,180.,0.
 1,4,CU 1.96,210.,0.
 1,5,CU 1.96,330.,0.
 4,6,NC 1.99,270.,0.
 5,7,NC 1.99,090.,0.
 4,8,AM 1.97,180.,0.
 4,12,AM 1.97,090.,0.
 5,16,AM 1.97,180.,0.
 5,20,AM 1.97,270.,0.
 6,24, C 1.32,120.,0.
 7,25, C 1.32,240.,0.
24,26, H 1.10,120.,0.
25,27, H 1.10,240.,0.
24,28, C 1.45,240.,0.
25,29, C 1.45,120.,0.
28,30, C 1.40,120.,0.
29,31, C 1.40,240.,0.
30,32, H 1.10,120.,0.
31,33, H 1.10,240.,0.
30,34, C 1.40,240.,0.
31,35, C 1.40,120.,0.
34,36, H 1.10,120.,0.
35,37, H 1.10,240.,0.
```

V. Fold of Bridging Azide out of Cu_2N_2(diazine) Plane in Model Complex M1

```
# IDEAL GEOMETRY, AM'S DEFINED W.R.T. N(1)
 37  3DIST    1 19
0.1,5.,10.,15.,20.,25.,30.,35.,40.,45.,50.,55.,60.,65.,70.,75.,80.,85.,90.
 EL WF CM OV OP RO NC
0.,0.,0.,DU
-1,1, N 0.98,090.,1000.
 1,2, N 1.20,180.,0.
 2,3, N 1.20,180.,0.
-1,4,CU 1.70,000.,0.
-1,5,CU 1.70,180.,0.
 4,6,NC 1.99,300.1,0.
 5,7,NC 1.99,300.,0.
 4,8,AM 1.97,120.,0.
 1,12,AM 3.86,-060.,0.
 5,16,AM 1.97,120.,0.
 1,20,AM 3.86,060.,0.
 6,24, C 1.32,120.,0.
 7,25, C 1.32,120.,0.
24,26, H 1.10,120.,0.
25,27, H 1.10,120.,0.
24,28, C 1.45,240.,0.
25,29, C 1.45,240.,0.
28,30, C 1.40,120.,0.
29,31, C 1.40,120.,0.
30,32, H 1.10,120.,0.
31,33, H 1.10,120.,0.
30,34, C 1.40,240.,0.
31,35, C 1.40,240.,0.
34,36, H 1.10,120.,0.
35,37, H 1.10,120.,0.
```

Parameters (exponents and atomic orbital energies) used in the MO calculations:

Atom	ζs	Hss(eV)	ζp	Hpp(eV)	ζd	ζd'	Hdd(eV)
H	1.300	-13.60	1.625	-11.40			
C	1.625	-21.40	1.625	-13.40			
N	1.950	-26.00	1.950	-13.40			
NC†	2.250	-26.00	2.250	-15.20			
Cu	2.800	-9.40	2.800	-5.06	9.150	3.000	-12.60
					0.5933‡	0.5744‡	

† NC parameters were used in place of standard N parameters for the diazine nitrogen atoms.

‡ contraction coefficients for d orbitals.